Liquid silicate equation of state: Using shock waves to understand the properties of the deep Earth

Thesis by

Claire Waller Thomas

In Partial Fulfillment of the Requirements for the

degree of

Doctor of Philosophy

CALIFORNIA INSTITUTE OF TECHNOLOGY

Pasadena, California

2013

(Defended April 11, 2013)

ACKNOWLEDGEMENTS

There are many to whom I owe thanks in the creation of this thesis. It takes a lot of people to blow up so many things—first thanks to Paul Asimow for being a pretty fantastic advisor, teacher, and mentor. He is likely the smartest person I know, but also manages to be the most patient and good-humored as well. That is a rare combination for which I am abundantly grateful. Thanks to the rest my committee: George Rossman, for academic and general life guidance; Jennifer Jackson, for an incredibly friendly and all-around pleasant demeanor, which makes me regret not throwing in a DAC chapter just for fun; and Ed Stolper, who despite having an incredibly full schedule makes time to serve on my committee and also provide both insightful and entertaining contributions to PRG each week. Thanks to the shock wave staff: Mike Long, Papo Gelle, Russ Oliver, and Oleg Fat'yanov for advice, patience, and insight as I learn from the masters of making things explode. My officemates Kristin Bergmann, Ajay Limaye, and Katie Stack are amazing people, but I can't really thank them for helping me with my thesis as we would rarely get work done when we were all in the office at the same time. Thanks to the delightful Dodd family and the Caltech swim team for making me have a life outside of lab. Thanks to my roommates/neighbors of the past 5 years, Fay Bi and Clara O'Farrell, for being such great friends despite being only thrown together by lovely chance of the Caltech housing lottery. Thanks to my parents as I am sure raising me was unpleasant as was having to deal the with the confusion of what it is I have been doing the past 5 years," I thought you were a geologist."

And finally thanks to my husband Daniel. He is the best person I know.

ABSTRACT

The equations of state (EOS) of several geologically important silicate liquids have been constrained via preheated shock wave techniques. Results on molten Fe_2SiO_4 (fayalite), Mg_2SiO_4 (forsterite), $CaFeSi_2O_6$ (hedenbergite), an equimolar mixture of $CaAl_2Si_2O_8$-$CaFeSi_2O_6$ (anorthite-hedenbergite), and an equimolar mixture of $CaAl_2Si_2O_8$-$CaFeSi_2O_6$-$CaMgSi_2O_6$ (anorthite-hedenbergite-diopside) are presented. This work represents the first ever direct EOS measurements of an iron-bearing liquid or of a forsterite liquid at pressures relevant to the deep Earth (> 135 GPa). Additionally, revised EOS for molten $CaMgSi_2O_6$ (diopside), $CaAl_2Si_2O_8$ (anorthite), and $MgSiO_3$ (enstatite), which were previously determined by shock wave methods, are also presented.

The liquid EOS are incorporated into a model, which employs linear mixing of volumes to determine the density of compositionally intermediate liquids in the CaO-MgO-Al_2O_3-SiO_2-FeO major element space. Liquid volumes are calculated for temperature and pressure conditions that are currently present at the core-mantle boundary or that may have occurred during differentiation of a fully molten mantle magma ocean.

The most significant implications of our results include: (1) a magma ocean of either chondrite or peridotite composition is less dense than its first crystallizing solid, which is not conducive to the formation of a basal mantle magma ocean, (2) the ambient mantle cannot produce a partial melt and an equilibrium residue sufficiently dense to form an ultralow velocity zone mush, and (3) due to the compositional dependence of Fe^{2+} coordination, there is a threshold of Fe concentration (molar $X_{Fe} \leq 0.06$) permitted

in a liquid for which its density can still be approximated by linear mixing of end-member volumes.

TABLE OF CONTENTS

LIST OF TABLES AND FIGURES

Chapter I

Introduction

Claire W. Thomas

An equation of state (EOS) (i.e., density as a function of pressure and temperature) for silicate melts at high pressure is of primary importance for understanding processes occurring within terrestrial interiors. There has previously existed only limited knowledge of melt density and compressibility determined at low pressures (< 40 GPa) on a restricted range of compositions. The goal of my graduate work documented by this thesis was to constrain the EOS for a number of important end-member liquids using shock wave studies and to incorporate them into an empirical, predictive model of melt density as a function of temperature, pressure and composition.

Chapter II describes the multi-technique collaboration of the University of Michigan, the University of New Mexico, and Caltech to constrain the EOS of molten Fe_2SiO_4 (fayalite). Shock wave experiments further extended the fayalite Hugoniot of *Chen et al*. [2002], which aided in resolving previously discrepant results for that study and the sink/float data set of *Agee* [1992]. The majority of the shock wave methods used for pre-heated experiments are described in this chapter. Subsequent chapters cover only changes made during each new set of experiments. The equations and derivation of the model used for creating isentropes of liquid mixtures is presented in detail in this chapter and is employed throughout the rest of the thesis.

The determination of the molten Mg_2SiO_4 (forsterite) EOS is presented in Chapter III, along with revised EOS parameters for $CaMgSi_2O_6$ (diopside), $CaAl_2Si_2O_8$ (anorthite) [*Asimow and Ahrens*, 2010], and $MgSiO_3$ (enstatite) melts [*Mosenfelder et al.*, 2009] . This new set of end member EOS, including fayalite, is used to determine the isentropic temperature profile of a fully molten magma ocean of two hypothetical bulk mantle compositions, chondrite [*Andrault et al.*, 2011] and peridotite[*Fiquet et al.*, 2010], by way of the isentrope mixture model presented in Chapter II. The temperature and pressure of first crystallization was determined from the

intersection of the isentrope and the experimental liquidus. This chapter also describes a melting model which employs linear mixing of liquid volumes to determine whether a partial melt and its equilibrium residue could produce an aggregate density that is comparable to that estimated by *Rost et al.*[2006] for a ultralow velocity zone and still maintain a low melt-residue density contrast (~1%) employed by the seismic modeling of *Williams and Garnero* [1996].

The EOS for $CaFeSi_2O_6$ (hedenbergite), a 50-50 mixture of $CaAl_2Si_2O_8$-$CaFeSi_2O_6$ (anorthite-hedenbergite), and an equimolar mixture of $CaAl_2Si_2O_8$-$CaFeSi_2O_6$-$CaMgSi_2O_6$ (anorthite-hedenbergite-diopside) are determined and described in Chapter IV. A series of tests on the validity of using linear mixing of volumes to predict the densities of multicomponent liquids at high temperature and pressure are presented. Results for these tests indicate that Fe-bearing silicate liquid densities can only be approximated as ideal under certain compositional restrictions.

REFERENCES

Agee, C. B. (1992), Isothermal compression of molten Fe_2SiO_4, *Geophys. Res. Lett.*, *19*(11), 1169–1172.

Andrault, D., N. Bolfan-Casanova, G. L. Nigro, M. A. Bouhifd, G. Garbarino, and M. Mezouar (2011), Solidus and liquidus profiles of chondritic mantle: Implication for melting of the Earth across its history, *Earth and planetary science letters*, *304*(1 – 2), 251 – 259.

Asimow, P. D., and T. J. Ahrens (2010), Shock compression of liquid silicates to 125 GPa: The anorthite-diopside join, *J. Geophys. Res.*, *115*(B10), B10209.

Chen, G. Q., T. J. Ahrens, and E. M. Stolper (2002), Shock-wave equation of state of molten and solid fayalite, *Physics of The Earth and Planetary Interiors*, *134*(1 – 2), 35 – 52.

Fiquet, G., A. L. Auzende, J. Siebert, A. Corgne, H. Bureau, H. Ozawa, and G. Garbarino (2010), Melting of Peridotite to 140 Gigapascals, *Science*, *329*(5998), 1516-1518.

Mosenfelder, J. L., P. D. Asimow, D. J. Frost, D. C. Rubie, and T. J. Ahrens (2009), The $MgSiO_3$ system at high pressure: Thermodynamic properties of perovskite, postperovskite, and melt from global inversion of shock and static compression data, *J. Geophys. Res.*, *114*.

Rost, S., E. J. Garnero, and Q. Williams (2006), Fine-scale ultralow-velocity zone structure from high-frequency seismic array data, *J. Geophys. Res.*, *111*(B9), B09310.

Williams, Q., and E. J. Garnero (1996), Seismic Evidence for Partial Melt at the Base of Earth's Mantle, *Science*, *273*(5281), 1528 – 1530.

Chapter II

Multi-technique equation of state for Fe_2SiO_4 melt and the density of Fe-bearing silicate melts from 0 – 161 GPa

Claire W. Thomas

Qiong Liu

Carl B. Agee

Paul D. Asimow

Rebecca A. Lange

Accepted to

Journal of Geophysical Research

August 27, 2012

ABSTRACT

New equation of state measurements on liquid Fe_2SiO_4 have been conducted in a collaborative, multi-technique study. The liquid density (ρ), the bulk modulus (K), and its pressure derivative (K') were measured from 1 atm to 161 GPa using 1-atm double-bob Archimedean, multi-anvil sink/float, and shock wave techniques. Shock compression results on initially molten Fe_2SiO_4 (1573 K) fitted with previous work and the ultrasonically- measured bulk sound speed (C_o) in shock velocity (U_S)-particle velocity (u_p) space yields the Hugoniot: U_S =1.58±0.03 u_p+ 2.438±0.005 km/s. Sink/float results are in agreement with shock wave and ultrasonic data, consistent with an isothermal K_T=19.4 GPa and K'=5.33 at 1500°C. Shock melting of initially solid Fe_2SiO_4 (300 K) confirms that the Grüneisen parameter (γ) of this liquid increases upon compression where $\gamma = \gamma_o(\rho_o/\rho)^q$ yields a q value of –1.45. Constraints on the liquid fayalite EOS permit the calculation of isentropes for silicate liquids of general composition in the multi-component system CaO-MgO-Al_2O_3-SiO_2-FeO at elevated temperatures and pressures. In our model a whole-mantle magma ocean would first crystallize in the mid-lower mantle or at the base of the mantle were it composed of either peridotite or simplified “chondrite” liquid, respectively. In regards to the partial melt hypothesis to explain the occurrence and characteristics of ultra-low velocity zones, neither of these candidate liquids would be dense enough to remain at the core mantle boundary on geologic timescales, but our model defines a compositional range of liquids that would be gravitationally stable.

INTRODUCTION

The formulation of an accurate equation of state (EOS) for silicate melts at high pressure and temperature is necessary to understand fully the important role of liquids in the differentiation and formation of terrestrial planets. The early history of the Earth may well have included one or more deep magma ocean events, perhaps extending to the core-mantle boundary (CMB) [*Labrosse et al.,* 2007]. During crystallization of magma oceans and also during partial melting events in predominantly solid mantle environments, the formation of chemically distinct reservoirs is controlled by gravitational differentiation and therefore intimately linked to the solid and liquid EOS. In particular, the possibility of crystal-liquid density cross-overs — that is, for a given liquid and a given mineral or assemblage of minerals, a horizon above which the liquid rises but below which it sinks [*Agee,* 1988; *Stolper et al.,* 1981] — implies dramatic bifurcation points in the possible paths of differentiation, leading to formation of either rising or sinking enriched reservoirs. These rising or sinking liquids will either potentially form crust or else potentially be sequestered at depth. Furthermore, changes in chemical equilibria with increasing pressure are defined by molar volume, the pressure derivative of the Gibbs free energy [*Asimow and Ahrens,* 2010]. Thus, accurate models of both the thermodynamic and fluid dynamic evolution of the Earth demand a fundamental knowledge of silicate liquid volumes at extreme pressure and temperature conditions.

In addition, detection of ultra-low velocity zones (ULVZ) [*Garnero and Helmberger*, 1995] at the base of the mantle may indicate the presence of silicate partial melts [*Lay et al.*, 2004; *Mosenfelder et al.*, 2009; *Williams et al.*, 1998] or more specifically iron-bearing melts [*Labrosse et al.,* 2007]. Seismic observations such as S- and P-wave speeds and inferred density have given clues as to the nature of the materials in ULVZs, but there are a number of candidate

iron-bearing solid phases that can produce the correct drops in wave speed and increased density without partial melting. Proposed phases include ferropericlase (Fe, Mg)O [*Wicks et al.*, 2010] and iron-enriched post-perovskite [*Mao et al.*, 2006]. Thus, improved constraints on iron-bearing silicate liquid densities at elevated pressure and temperature will aid in answering whether a liquid or liquid-solid mush could be dynamically stable at the CMB and similarly what the relative buoyancy of melt and its co-existing solids would be. There are presently no published experimental constraints on the density of iron-bearing silicate liquids beyond 47 GPa [*Chen et al.*, 2002; *Miller et al.*, 1991a].

Silicate liquids occupy a large, multi-dimensional continuum of compositions and therefore understanding their range of behavior requires either data on a very large number of compositions or data on a minimum set of end-member compositions and a reliable means of interpolating in composition space. At low pressure, ideal mixing of volumes has proven to be a reliable tool [*Lange and Carmichael*, 1987], but it remains poorly tested at high pressure [*Asimow and Ahrens*, 2010]. Here we present results on a pure iron-bearing end-member, fayalite (Fe_2SiO_4). In the future, this will allow assessment of intermediate compositions with lower iron contents without the need for extrapolation and provide an essential tie-point for the assessment of linear mixing along iron-magnesium mixing joins.

Previous shock experiments on fayalite (Fe_2SiO_4) liquid achieved pressures up to 47 GPa [*Chen et al.*, 2002], which corresponds to about mid-mantle range [*Dziewonski and Anderson*, 1981]. For this work, we extended this pressure range to 161 GPa, beyond CMB pressures, so we may apply our results to understanding the effects of iron on deep mantle systems. Additionally, this collaborative work sought to resolve inconsistencies in previous reports on Fe_2SiO_4 liquid compressibility and its change with pressure. Published isothermal static compression data from

sink/float experiments [*Agee*, 1992] and shock wave results [*Chen et al.*, 2002] are in close agreement for bulk modulus (K_o) values but differ greatly on the value of the pressure derivative (K'), 10.1 (isothermal) and 5.36 (isentropic), respectively, which give very divergent predictions for density at higher pressure. Isothermal and isentropic equations of state need not be the same, but a larger K' for the isotherm implies a negative coefficient of thermal expansion, which is contrary to expectations. The anomaly is even more apparent when the Hugoniot data at estimated shock temperatures are compared to the extrapolated isotherm (Figure 1). For instance, at 15 GPa, the estimated shock state is at temperature (T_S) 1783K and density ~4.75 g cm^{-3}, somewhat denser than the extrapolated isotherm at the same P and T, ~4.5 g cm^{-3}. At 50 GPa however, the estimated Hugoniot state is at temperature 2943 K and density ~6.0 g cm^{-3}, much denser than the extrapolated 1773 K isotherm at 50 GPa, 4.75 g cm^{-3}, whereas one expects density to decrease with increasing temperature. This discrepancy was also noted by Ghiorso (2004), whose equation of state fitting exercise produced an internally consistent prediction of all fusion curve data and Hugoniot volume data, but underestimated the density of neutral buoyancy experiments from *Agee* [1992] by 1%.

We have conducted new measurements of the equation of state of molten fayalite (Fe_2SiO_4) using the following techniques: (i) double-bob Archimedean method for melt density and thermal expansion at ambient pressure (University of Michigan), (ii) multi-anvil sink/float technique to measure melt density to 4.5 GPa (University of New Mexico), and (iii) shock wave measurements of *P-V-E* equation of state to 161 GPa (Caltech). The aim of this multi-technique study has been to measure the density of molten Fe_2SiO_4, to resolve the discrepancy in published EOS for this material, and to use the measured equation of state to address processes of early earth differentiation and stability of a liquid at the CMB.

METHODS

1- atm double-bob Archimedean methods

The shared starting material for the double-bob density measurements and the shockwave experiments was synthesized at the University of California, Berkeley, by Mark Rivers and contains 64.48 mol% Fe as FeO, 34.97 mol% SiO_2, and 0.56 mol% Al_2O_3 (wet chemical analysis is reported in *Rivers and Carmichael* [1987]), slightly off fayalitic composition (66.66 mol% FeO, 33.33 mol% SiO_2). This is the same material used for ambient ultrasonic sound speeds reported in *Ai* and *Lange* [2004].

The starting material was a brick-red powder with iron predominantly in the form of ferric iron (Fe^{3+}). To produce a starting composition with iron as Fe^{2+}, approximately 75 g was loaded step-wise in four batches (~18-20 g each) into a straight-wall molybdenum crucible (7.8 cm deep and 3.6 cm inner diameter) placed in a Deltech furnace at 1300°C in a reducing stream of 1%CO-99%Ar. Each batch of melt was held at 1300°C for 12 hours until all 75 grams were loaded into the crucible and reduced. The Mo crucible was then placed on a platform in the Deltech furnace such that the top 3 cm of the liquid corresponded with the isothermal hotspot in the furnace. A thermal profile from the top of the crucible down into the sample had been previously documented for a Mo crucible filled with alumina powder for each temperature of measurement. Temperature was measured at the top of the crucible with an S-type thermocouple, calibrated against the melting temperature of gold.

Liquid density measurements were made on the Fe_2SiO_4 liquid using the double-bob Archimedean method, described in detail in *Lange and Carmichael* [1987]. The method was adapted for a reducing atmosphere (1%CO-99%Ar) in this study by using molybdenum instead of platinum for the two bobs and the crucible. An electronic balance with a precision of ±0.0001

g was mounted on an aluminum platform above the furnace to measure the weights of the Mo bobs before and after immersion into the Fe_2SiO_4 liquid. By using two Mo bobs of different mass (~20 and ~7 g), but identical stem diameters (1 mm), the effect of surface tension on the stem was eliminated. The density of the liquid is calculated from the following equation:

$$\rho(T) = \frac{B_L(T) - B_S(T)}{V_L(T) - V_S(T)} \quad (1)$$

where $B_L(T)$ and $B_S(T)$ are the buoyancy of the large and small bob, respectively, and $V_L(T)$ and $V_S(T)$ are the immersed volume of the large and small bob, respectively. The buoyancy is defined as the mass of the bob in the gas stream (corrected to vacuum) minus the mass of the bob during the immersion in the Fe_2SiO_4 melt. Four density measurements were made at each temperature with two different large bobs and two different small bobs. The accuracy of using Mo bobs instead of Pt bobs was tested by measuring the density of NaCl liquid at 1286 K and the result (1.445 g/cm^3) closely matches that recommended by NIST [*Janz*, 1980] at this temperature (1.441 g/cm^3).

Sink/float methods

Fayalite used for sink-float experiments was the same sample used in the original *Agee* [1992] study. This is a different starting material than used in the double-bob density and shockwave measurements of this study. The fayalite was synthesized in a Deltech gas-mixing furnace for 24 hours at controlled fO_2 (IW-1). All sink-float experiments were carried out in a Walker-style multi-anvil device at the University of New Mexico, as opposed to a piston-cylinder device at the Bayerisches Geoinstitut used in *Agee* [1992]. Two types of gem-quality marker spheres were used: a spessartine garnet from the Malagasy Republic with composition $Alm_{10.6}Sps_{89.4}$ (also used in *Agee* [1992]) and a San Bernardino almandine-rich garnet

$Alm_{80.0}Grs_{8.9}Sps_{6.4}Pyr_{4.7}$. Experiments were run in high purity molybdenum capsules, with run times of approximately 30 seconds at 1500°C. For further details of the experimental method, see *Circone and Agee* [1996].

Shock wave methods

Sample synthesis and preparation of preheated (1573 K) shots

The shared starting material used for the shock wave and double-bob experiments was reduced in a similar manner as described above in the double-bob methods section to produce a starting composition with the correct oxidation state (Fe^{2+}). The powder was melted in a deep (3.5 cm deep, 1.7 cm inner diameter) molybdenum crucible hung on molybdenum wires in a Deltech furnace at 1300°C in a reducing gas stream of 1%CO-99%Ar. The powder was melted in short 30-45 minute runs; quenched and re-filled several times to reach the crucible's capacity; and then left to equilibrate for 18 hours at temperature. The quenching process used was unfortunately slow to avoid CO gas release or rapid oxidation on hot exposure to air. An extra-long ceramic hanging rod was used to push the crucible out of the hot spot to the bottom of the furnace tube to cool within the reducing atmosphere. Once the crucible was no longer glowing red (approximately 10 minutes), nitrogen was streamed for 10 minutes followed by a finishing quench in water. A combination of volume reduction on crystallization and surface tension at the crucible walls typically left a 5mm diameter triangular pit in the center, which reached nearly half way to the bottom of the crucible.

Mössbauer spectra measured by Bjorn Mysen at the Carnegie Institution of Washington confirmed that Fe in the run products was reduced and dominantly in the form of fayalite and wüstite (FeO) with minor amounts of an iron-bearing accessory mineral, most likely magnetite. This aggregate was too fragile to be lapped into disks to fit into shock wave experiment sample

holders, so it was re-ground and hot-pressed in a piston-cylinder device at 10 kbar and 725°C using a graphite sleeve and CaF_2 base plug. The maximum fO_2 in our graphite sample assembly is controlled by the CCO buffer[*Holloway et al.*, 1992; *Médard et al.*, 2008] with a calculated log fO_2 of -16 at our *P-T* conditions [*Jakobsson and Oskarsson*, 1994; *Ulmer and Luth*, 1991].Experimental results from *Médard et al.* indicate that the fO_2 within graphite capsules is likely more reducing than the CCO buffer (average value: CCO-0.07; IW+1.5), therefore the amount of Fe^{3+} introduced during this process is assumed to be negligible. The sample underwent synchronized slow decompression (1 MPa/minute) and cooling (1 K/minute) to reduce cracking during recovery, but usually the cylinder of fayalite naturally separated into rough 2–3 mm-thick disks. The hot-pressing increased the bulk density and sintered the aggregate into a machinable form; the sample disks were cored to 8 mm outer diameter. The composition was checked for carbon contamination from the graphite hot-pressing sleeve on a scanning electron microscope using energy-dispersive x-ray spectroscopy, but none was found. There were minor amounts of molybdenum contamination in the form of Fe-Mo metal oxides, but total bulk Mo content was constrained to less than 2 wt% with electron microprobe analyses. The disks were then lapped down to under-fill the volume of the molybdenum sample holder (see below) by 7-13%, such that — accounting for thermal expansion of the Mo holder [*Miller et al.*, 1988] and the Fe_2SiO_4 liquid density at ambient pressure and 1300°C — a void space 1–1.5 mm-deep would remain at the top of the heated capsule. This small void space volume prevents blow out, excessive warping, or failure of the welded cap and yet remains far enough above the imaged area of the shock wave to preserve one-dimensional wave propagation.

The molybdenum sample holders are comprised of a driver plate, sample well, and cap. The outer and inner portions of the rear-surface of the driver plate and both sides of the cap were

polished to a mirror-finish with 1-micron alumina grit. For the two completed preheated shots, both caps had a thickness of 1mm, and all sample wells were 8mm in diameter and approximately 2.5mm deep. Shot 409 had a driver plate 1mm thick, and shot 396 had a 2 mm-thick driver plate. After polishing, a line profile of the driver plate topography inside the sample well was measured with a depth gauge micrometer using a 0.7 mm flat-end tip in 0.2 mm increments along the centerline, which is aligned to the streak camera slit position.

An outside contractor (Electron Beam Engineering Inc., Anaheim, CA) electron-beam welded the caps to the sample holder wells enclosing the sample to prevent leaking during experimental heating. After bake-out at 100±3 °C, an initial circular pass of a defocused, low-power beam under 10^{-4} torr vacuum helps residual gases to escape; trapped volatiles could lead to bowing of the sample cap during experimental heating. Sample holders are leak-checked at room temperature in a helium bomb and additionally in a heat test chamber at 1573 K by visual inspection for escaping fayalite liquid. We note that fayalite is an especially troublesome liquid to weld into capsules due to its low melting point, high surface tension, and poor glass-forming; ten capsules were lost to bad welds in obtaining the two successful capsules that were used for our experiments.

The final driver and top hat shape were measured with a depth gauge micrometer on a digital mill table in 0.1 mm increments along the bright vertical line in Figure 2a. The sample capsules were carbon coated on both sides to ~80-200 nm thickness using a Cressington model 208C coater except for a thin rectangular masked area where the streak camera slit images the shock arrival. The layer of carbon provides an oxygen sink to reduce oxidation the molybdenum during heating, which can degrade the reflection into the streak camera [*Asimow and Ahrens*, 2010].

Preparation of room temperature (300 K) shots

One solid room-temperature (300 K) shot was performed, extending the pressure range of previous room-temperature shocks on fayalite [*Chen et al.*, 2002] from 212 GPa to 229 GPa. This was done to verify that the highest-pressure 300 K shots (107, 161, 126, 412; See Table 2) melted during impact, which is necessary for calculation of the liquid Grüneisen parameter (γ). Details of this calculation are in the Results section under *Grüneisen parameter*.

The sample used was a single crystal of fayalite synthesized by H. Takei [*Takei*, 1978]. The boule was cut perpendicular to the growth axis into an elliptical disk with a minimum diameter of 7.8 mm and a maximum diameter of 8.8 mm. The disk was doubly polished to 2 mm thickness (within ±0.002 mm of uniform thickness). The crystal contained some glassy inclusions, but their estimated volume from electron backscatter images was less than 4%. The sample was directly mounted on a 0.5 mm tantalum driver plate and was not encapsulated. A series of fused quartz mirrors were glued to the down-range side of the driver plate and sample [cf. *Mosenfelder et al.*, 2007] for recording of the shock arrival.

Experimental setup

The experimental methods used in our study for molten materials were originally developed by *Rigden et al.* [1984] and refined by *Rigden et al.* [1988; 1989], *Miller et al.* [1988; 1991a], *Chen et al.* [1998; 2002] and *Asimow et al*. (2008). The experimental configuration is summarized here; for additional description, see *Asimow and Ahrens* [2010].

The experiments for this study were performed in a 90/25- mm two-stage light-gas gun; previous shots from *Chen et al.* (2002) were performed using a 40- mm propellant gun. Shots 396 and 409 were preheated with a H_2O-cooled copper induction coil powered by a 10 kW Lepel radio frequency generator [*Chen and Ahrens*, 1998] to 1300°C (1573 K), 95°C above the melting

point of pure Fe_2SiO_4. For preheated experiments, the sample holders are mounted through a hole drilled in a Zircar™ alumina board and are held in place by a "guy-wire" set up in which W-Re alloy wire is threaded through two Mo posts screwed into the sample side of the target.

Tantalum flyer plates were pressed into Lexan projectiles and launched at velocities (u_{fp}) of 4.997-7.085 km/s, measured by a double-flash x-ray system and a two-magnet induction detector [*Asimow et al.*, 2008]. For all three shots reported here, the two measurements agreed to within the stated uncertainty, and the average of the two measurements was used for the u_{fp}. For room-temperature experiments (shot 412), the streak camera is electrically triggered by signals from shorting pins. For preheated shots, the camera and xenon spark lamp (which illuminates the target) are triggered using a "non-contact" system from the flyer-magnet signals and an up-down counter [*Asimow and Ahrens*, 2010]. The light is filmed by a Hadland Imacon 790 streak camera equipped with a 25 μm slit focused horizontally across the center of the sample holder (Figure 2a). As the shock wave reaches the free surface of the driver and later the sample cover, it changes the reflectance of the polished surface, creating a visible cutoff on the film. The shock wave velocity (U_s) through the sample is calculated from the time difference of these two cutoffs, corrected for the known shape of the driver face and cap and thermal expansion of the assembly, and subtracting the shock transit time through the Mo cap. The final shock state is calculated iteratively using the technique developed in *Ridgen et al*. [1988], which takes into account the thickness and EOS of the hot molybdenum cap. The camera writing rate was calibrated using a test streak modulated by a radio-frequency tuner at 147.9993 MHz, which provides a time signal every 6.757 ns. The streak photo was scanned at 2400 dpi in 8-bit gray scale and matched to the calibration streak scanned at the same resolution to assign each column of pixels a time value. Driver and sample cutoffs were picked by selecting the inflection point of

an arctangent function fit by cross-correlation to the gray scale values of each row of pixels parallel to the time axis (Figure 2c, shows only 3 pixel rows). If the correlation coefficient for the arctangent fit for a given pixel line was less than 0.95, then that pick was discarded. Discarding of pixels usually occurred in dark portions of the photo that were either poorly exposed or dark in the pre-experiment static photo due to imperfections in the polish. A few hundred points on either side usually constrain the driver cutoff (except in shot 396, see below); these picks are co-registered with the previously measured driver topography profiles and corrected for deviations from flat. Although tilt and bowing of the impactor and hence the shock front are often approximated as parabolic [*Mitchell and Nellis*, 1981a], we found that fourth order polynomial fits were suitable for extrapolating the shape of the shock front within the sample (Figure 2b). Only the center 3mm portion of the sample arrival was used for the calculation of shock transit time to reduce edge effects. The iterative solutions [*Rigden et al.*, 1988] to particle velocity (u_p), pressure (P_H), and density (ρ_H) of the shock state were determined from impedance matching, the Rankine-Hugoniot equations, and the following input parameters: sample geometry; standard Hugoniot data (ρ_o, C_o, s) for the metal flyer, driver and cover plates [*Asimow et al.*, 2008; *Mitchell and Nellis*, 1981b]; and the initial density (ρ_o) and best-initial guess values for 1 bar bulk sound speed (C_o) and Hugoniot slope s for fayalite liquid at 1300 °C. It should be noted that regardless of the initial guess for the C_o and s the same resulting shock state converges after three iterations). Uncertainties in all derived parameters (U_S, u_p, P_H, ρ_H) were obtained from the uncertainties in the measured and standard parameters by analytical error propagation [cf. *Jackson and Ahrens*, 1979].

RESULTS

Density and ultrasonic results at ambient pressure

The double-bob density measurements between 1551 and 1831 K are reported in Table 1 and plotted against temperature in Figure 3. A linear equation: $\rho(T) = 3699\pm1 - 0.30\pm0.01*(T-1573\ K)$ was fit to the data. Sound speed (C) data on the same sample between 1516 and 1879 K are reported in *Ai and Lange* [2004] using a frequency-sweep acoustic interferometer. Those data can also be described as a linear function of temperature: $C(T) = 2438\pm5 - 0.33\pm0.03*(T-1573\ K)$ m/s.

Sink/ float results

The results from the sink/float experiments are shown in Figure 4. We observed floating of the almandine garnets at 3.5 and 4.5 GPa and floating of spessartine garnets at 4.0 GPa. We were unsuccessful in observing sinks or floats at 3.0 GPa because of marker sphere dissolution or breakdown during the run. Therefore, our new data do not bracket the fayalite liquid density. However the observed floats do give a minimum density of the liquid within the experimental pressure range 3.5-4.5 GPa, and thus the new data do not agree with the sink/float measurements of *Agee* [1992] requiring that the compression curve for fayalite liquid be at higher density values in the range 3.5-4.5 GPa. On the other hand, the measurements of *Agee* [1992] at lower pressure using ruby spheres are still consistent with the new multi-anvil measurements. Reasons for possible inconsistencies in the *Agee* [1992] are discussed below.

Shockwave results

Comparison to previous data

The shock wave data are reported in Table 2, including shot number, flyer/driver material, temperature prior to firing, u_{fp}, u_p, U_S, P_H, and peak density (ρ_H). Figure 5 shows the Hugoniot of this data in U_S-u_p space. A Hugoniot is a family of shock states achieved in a

material from the same starting conditions (in this case, liquid fayalite at 1573 K and 1 bar). Empirically the Hugoniot of a well-behaved material forms a line in U_S-u_p space, given to third order in strain by $U_S = C_o + s\,u_p$ [*Jeanloz,* 1989] where the intercept $C_o = (K_{oS} / \rho_o)^{1/2}$ is the bulk sound speed of fayalite liquid at room pressure and the slope $s = (K'_S + 1)/4$ is related to K'_S, the isentropic pressure derivative of the isentropic bulk modulus (K_{oS}) [*Ruoff,* 1967].

Previous work from *Chen et al.* [2002] consists of 7 experiments completed on the Caltech 40-mm propellant gun. All *Chen et al.* data are taken from the original publication and were not re-analyzed. These data have widely varying reported uncertainties; *Chen et al.*'s linear regression was weighted by errors on U_s only: $U_s = 2.63\pm0.02 + 1.59\pm0.01\,u_p$ km/s.

To these data, we added two preheated shocks, extending the Hugoniot to 161 GPa. Shot 409 from this study had clear cutoffs and well-defined shock arrivals. Conversely, shot 396 had a poorly exposed driver arrival, but showed a simple, un-tilted planar shock arrival at the top hat. The driver arrival for this shot was approximated as linear and un-tilted, which introduced error in the travel time measurement but is a suitable assumption due to the flatness of the top hat. An un-weighted linear fit to all nine preheated fayalite liquid data points from *Chen et al.* [2002] and this study yields $U_s = 2.67\pm0.08 + 1.50\pm0.03\,u_p$ km/s (r^2= 0.996), whereas a York regression (a regression which accounts for errors in both U_s and u_p) gives $U_s = 2.80\pm0.18 + 1.488\pm0.071\,u_p$ km/s (MSWD = 8.9).

The unconstrained intercept of the York fit to the full data set is consistent within the 99% confidence interval with the bulk sound speed determined to much higher precision by ultrasonic techniques, C_o= 2.438±0.005 km/s [*Ai and Lange,* 2004]. This suggests we cannot confidently reject the null hypothesis that this material, like other silicate liquids measured in the same way, displays relaxed (liquid-like), as opposed to un-relaxed (glass-like), behavior upon

shock compression [*Rigden et al.*, 1988]. Therefore, to reduce the error on the linear fit, we fixed the intercept at the ultrasonic value measured in this work. The un-weighted, constrained linear fit in U_S-u_p space yields U_S = 2.438±0.005 + 1.58±0.03 u_p km/s (r^2=0.998**)**. A weighted, constrained fit yields poor results because the uncertainties of U_S reported for some of *Chen et al.*'s data are anomalously small. The selected slope *s* corresponds to a K'_S value of 5.33±0.10, and overall this is in reasonable agreement with the previous work by *Chen et al.* [2002], which estimated K'_S of 5.39±0.04. Figure 5 includes both the unconstrained and constrained linear fits to the entire data set, as well as the previous fit by *Chen et al.* [2002]. It is worth noting that the slopes of the new and old linear fits are very similar despite having slightly different though nominally fayalitic compositions. Thus within the errors of the experiments, our results seem to be insensitive to minor compositional differences.

Our newest shockwave and sink/float results also resolve previously discrepant measurements for K'_S. Isothermal static compression data from sink/float [*Agee*, 1992] and shock wave [*Chen et al.*, 2002] experiments gave *K*' values of 10.1 and 5.36, respectively. The newest sink/float measurements are shown in Figure 4 alongside two 3rd-order Birch-Murnaghan isotherms (dashed and dotted lines).The isotherms are fit with ρ_o from this study, the bulk modulus from ultrasonic experiments (K_T=19.4) [*Ai and Lange*, 2004], and *K*' from the slope of the newest constrained linear Hugoniot (*K*'=5.33)(dashed in Fig. 4) or *K*' from the 3rd-order Birch-Murnaghan/Mie-Grüneisen (3BM/MG) (*K*'=7.28) from this study (dotted in Fig. 4). The details of the 3BM/MG fit are given below in the *Thermal equation of state fitting* section. The solid line is calculated using the previous data from *Agee* [1992]. The three experiments showing flotation are consistent with the dashed and dotted lines and discount the previous measurements (>3 GPa) on identical material used in the 1992 study. It is conceivable that piston "bottoming-

out" or other unknown friction effects at high compressions and high temperatures produced lower pressures than expected from calibration runs. In any case, the new multi-anvil sink/float data are in good agreement with the ultrasonic and shockwave results.

Solid Hugoniot shocked to liquid / χ^2 test of weighted values

Shot 412 was carried out on single crystal fayalite and is believed to have undergone a phase transition to liquid during the shock. A phase transition to liquid along the Hugoniot can often be detected by an offset in pressure-volume [*Akins et al.*, 2004] or U_S-u_p space. To establish where in U_S-u_p space the phase transition occurs, we used a χ^2 test of weighted values on linear fits to all room-temperature shock data (Table 1). The goal was to minimize the χ^2 value of fitting two separate linear Hugoniots to solid and shock-melted data. Excluding shot 116, which has an anomalously low U_s, the best fit (χ^2= 0.0014867) occurred when shots 107, 161, 126, and 412 were calculated as liquids. The pressure limit of 190 GPa for shock melting implied by placing the boundary between shots 99 and 107 is also consistent with the melting thresholds along the Hugoniots of many iron-free silicate minerals shocked from room temperature: quartz at 120 GPa [*J. A. Akins*, 2002; *Lyzenga*, 1983], diopside at ≤144 GPa [*Svendsen and Ahrens*, 1990], and diopside-anorthite ($Di_{64}An_{36}$) at 133 GPa [*Asimow and Ahrens*, 2010] all of which have higher ambient melting temperature than that of fayalite (previous descriptions of shock melting of forsterite at 142 GPa [*Mosenfelder et al.*, 2007] enstatite at 174 GPa [*Mosenfelder et al.*, 2009] may not be accurate and are discussed in Chapter III). We have therefore used the four highest-pressure data points, presumed to have melted on shock, to calculate a value for the liquid Grüneisen parameter.

Grüneisen parameter

The thermodynamic Grüneisen parameter (γ) is a macroscopic parameter that relates

thermal pressure to the thermal energy per unit volume, where thermal pressure is defined as the increase in pressure due to heating at a constant volume. Because a solid shocked to a liquid and an initially molten sample obtain different pressures and internal energy states at equal density (ρ_H) upon compression, γ can be directly determined by comparison of the two Hugoniots (e.g., [*Luo et al*., 2002; *Mosenfelder et al*., 2007, *Asimow & Ahrens*, 2010]). We calculated the Grüneisen parameter from the following expressions; the parameter definitions and the values used are given in Table 3. By definition,

$$\gamma = \frac{1}{\rho}\left(\frac{\partial P}{\partial E}\right)_{\rho}. \tag{2}$$

The Mie-Grüneisen approximation defines γ as a function of ρ only, which simplifies the above expression to a finite difference:

$$\gamma = \frac{1}{\rho}\frac{\Delta P_{th}}{\Delta E} = \frac{1}{\rho}\frac{(P_{H-liquid} - P_{H-solid})}{\Delta E}, \tag{3}$$

where ρ is the density of interest and ΔP_{th} and ΔE are the offsets in pressure and internal energy between the two Hugoniot states at that density. The subscripts *H-liquid* and *H-solid* correspond to states on the Hugoniots that are both liquid in the shock state but that were initially a liquid at 1573 K and a solid at 300 K, respectively. The energy offset is calculated from

$$\Delta E = \Delta E_{H-solid} - \Delta E_{H-liquid} + \Delta E_{tr}, \tag{4}$$

where ΔE_{tr}, the transition energy, is the internal energy difference at ambient pressure conditions and is estimated by the enthalpy difference (ΔH_{tr}) because the transition takes place at nearly zero pressure [*Asimow and Ahrens*, 2010]. ΔH_{tr} is composed of two parts, the integral

of the isobaric heat capacity (C_P) and the enthalpy of fusion, and was calculated with MELTS [*Ghiorso and Sack*, 1995]. The internal energy change across each shock front (ΔE_H) was calculated using the 3rd Rankine-Hugoniot relation,

$$\Delta E_H = \frac{P_H}{2}\left(\frac{1}{\rho_o} - \frac{1}{\rho_H}\right) \quad . \tag{5}$$

There are several empirical forms for describing the density dependence of $\gamma(\rho)$ consistent with the Mie-Grüneisen assumption [*Stixrude and Lithgow-Bertelloni*, 2005]. We will look only at the power law form, which is both the simplest and most prevalent in the literature:

$$\gamma(\rho) = \gamma_o(\rho_o / \rho)^q . \tag{6}$$

The Grüneisen parameter at initial conditions is derived from the expressions

$$\gamma = \frac{\alpha K_T}{\rho C_V} \tag{7}$$

and

$$\frac{C_P}{C_V} = 1 + \alpha\gamma T \, , \tag{8}$$

where α is the isobaric coefficient of thermal expansion, C_V is isochoric heat capacity, and C_P is isobaric heat capacity.

Fitting the offset between the Hugoniots of fayalite liquid shocked from liquid and solid initial states to equation (5) yields a q value of –1.45 based on data in the vicinity of ρ_o/ρ =0.49. In solid materials γ generally decreases upon compression (Figure 6), but a negative q value demonstrates that γ for this liquid increases upon compression. Moreover, this q value is similar

to values obtained on other silicate liquid compositions using Hugoniot offsets, such as forsterite (q = –1.47) (corrected from the *Mosenfelder et al.* value, see Table 5; Chapter III includes a new EOS from preheated forsterite), enstatite (q = –1.71) [*Mosenfelder et al.*, 2009] (revised in Chapter III), and anorthite-diopside eutectic (q = –1.63) [*Asimow and Ahrens*, 2010]. We take this result as strong evidence that iron-bearing silicate liquids follow the same general behavior as iron-free silicate liquids, which are all described by $-2.0 \leq q \leq -1.45$ for the compression range $1 \geq \rho_o/\rho \geq 0.49$. Figure 6 shows the similarities in volume dependence of γ for liquids of composition $MgSiO_3$ (En), Mg_2SiO_4 (Fo), and Fe_2SiO_4 (Fa) as well as the opposite dependence displayed by mantle solids.

Negative q values for liquids have been interpreted qualitatively as a result of increasing cation coordination by analogy to structural phase changes in related solids [*Stixrude and Karki*, 2005] and, more recently, quantitatively in terms of liquid configurational entropy in the context of a hard-sphere model of atomic packing in liquids [*Jing and Karato*, 2011a]. The consistent behavior of fayalite with other liquids so far studied does not obviously resolve the question of the microscopic origin of the behavior, but it shows that the behavior does not depend very much on the major cations in the liquid.

Thermal equation of state fitting

A Hugoniot is a one-parameter curve through a *P*-*V*-*E* thermodynamic space of two independent variables, in this case $V(P, E)$. However, we are generally interested in defining the behavior of liquids in regions that lie off the Hugoniot curve. In particular, at high compressions, the Hugoniot reaches temperatures and energies much higher than mantle conditions of geophysical interest, even for the early earth. In order to investigate material properties that lie off the Hugoniot, we attempt to define the entire *P*-*V*-*E* surface for a given composition by fitting

a thermal equation of state. There are several formalisms for thermal EOS; we have chosen to investigate three of them (all of which are plotted in Figure 7): (1) the shock wave equation of state (SWEOS, derived from both the constrained and unconstrained linear fit above), (2) 3rd and 4th order Birch-Murnaghan Mie-Grüneisen equation of state (3BM/MG and 4BM/MG), and (3) de Koker-Stixrude fundamental relation (dKSFR) [*de Koker and Stixrude*, 2009].

The SWEOS is defined by a linear Hugoniot in $U_S - u_p$ space, transformed into pressure (P)- density (ρ) space using the first and second Rankine-Hugoniot equations [e.g., *Ahrens*, 1987]:

$$\rho_H = \frac{\rho_o U_S}{U_S - u_p} \tag{9}$$

$$P_H = \rho_o U_S u_p . \tag{10}$$

States that lie off the Hugoniot are found using the Mie-Grüneisen thermal pressure approximation with temperature-independent $\gamma(\rho)$, as calculated above (6).

The 3rd- and 4th-order Birch-Murnaghan/Mie-Grüneisen equations of state are defined by 3rd or 4th order Birch-Murnaghan isentropes centered at 1 bar and 1573K plus a Mie-Grüneisen thermal pressure approximation. Thus, total pressure P at any volume and internal energy is given by

$$P = P_S + P_{th} . \tag{11}$$

P_s is the Birch-Murnaghan isentropic pressure given to 4th order in strain by

$$P_S = 3K_{oS} f(1+2f)^{\frac{5}{2}}(1+\frac{3}{2}(K'_S - 4)f + \frac{3}{2}(K''_S K_{oS} + K'_S (K'_S - 7) + \frac{143}{9}) f^2) \tag{12}$$

where f is the Eulerian finite strain parameter

$$f = \frac{1}{2}\left(\left(\frac{\rho}{\rho_o}\right)^{\frac{2}{3}} - 1\right). \quad (13)$$

[*Birch*, 1947]. The thermal pressure term (P_{th}) is given by

$$P_{th} = \gamma\rho(E - E_S) \quad (14)$$

where E is the energy of interest. The internal energy along the isentrope (E_S) is found by integration of $dE_S = -P_S dV$:

$$E_S = \frac{9}{2}\frac{K_{oS}}{\rho_o}\left(f^2 + (K'_S - 4)f^3 + \frac{3}{4}(K''_S K_{oS} + K'_S(K'_S - 7) + \frac{143}{9})f^4\right) \quad (15)$$

For 3rd-order BM isentropic pressure and energy, K" in the previous expressions is fixed to the value that makes the 4th-order term vanish:

$$K''_S = -(K'_S(K'_S - 7) + \frac{143}{9})/K_{oS} \quad (16)$$

In order to infer a temperature, we need to define an isochoric heat capacity (C_V). Currently no shock temperature measurements exist to constrain an expression for $C_V(\rho)$ for an iron-bearing silicate liquid, so C_V was fixed at the constant value determined from constant C_P at ambient pressure and 1573 K [*Lange and Navrotsky*, 1992]. The temperature of interest is then calculated with the equation

$$T = T_o \int_{\rho_o}^{\rho} \frac{\gamma(\rho)}{\rho} d\rho + \int_{E_S}^{E} \frac{1}{C_V} dE, \quad (17)$$

which is composed of two parts: (1) integration along the reference isentrope to the density of interest with T_o = 1573 K as the foot temperature and (2) addition of the energy offset proportional to C_V.

A method for fitting shock wave data to the 3BM/MG and 4BM/MG forms is found in *Asimow and Ahrens* [2010]. To account for uncertainties in both pressure and volume, the function

$$\chi^2 = \sum_{i=1}^{n} \left[\left(\frac{P_*^i(\rho_*^i) - P_H^i}{\sigma_\rho^i} \right)^2 + \left(\frac{\rho_*^i - \rho_H^i}{\sigma_\rho^i} \right)^2 \right] \tag{18}$$

is minimized, where pressure is evaluated along the model Hugoniot at the trial density

$$P_*^i = \frac{P_S - \gamma\rho_*^i(E_S - E_{tr}^i)}{1 - \frac{\gamma}{2}\left(\frac{\rho_*^i}{\rho_o^i} - 1\right)}. \tag{19}$$

The subscript * denotes a trial pressure or density, and σ denotes the respective uncertainties for each pressure-density experimental pair, (P^i_H, ρ^i_H). Uncertainties in the fitted parameters are estimated by bootstrap iteration [*Efron*, 1982]. The input parameters that remain fixed are $K_{oS,}$ C_V, ρ_o, and γ_o; the best-fit parameters (K'$_S$ and q, plus K'' for 4BM) are given in Table 4. The 3BM/MG fit result is K_S' = 7.28±0.35, q = –0.95±0.51, and a reduced χ^2 = 1.526. The 4BM/MG fit result is K_S' = 6.64±0.58, K_S" = –0.47±0.27 GPa^{-1}, q = –0.54±1.49 and reduced χ^2 = 0.941. The 4BM/MG chi-squared value indicates probable over-fitting, and the fairly large error bars on all output parameters seem to indicate a very unstable fitting routine. On the other hand, the 3BM/MG seems relatively stable. The unconstrained-SWEOS appears to have similar form to the 3BM/MG and matches the highest pressure data better than the constrained SWEOS. The

stiffness in the constrained SWEOS is likely due to being tied to the intercept and the most precise of *Chen et al.*'s data points—the precision of which is likely overestimated. The *q* value for the SWEOS is just within the stated errors of the 3BM/MG value, and the 3BM/MG reduced chi-squared value is reasonable. Additionally with little justification to implement the 4th-order fit, we recommend the 3rd-order fit for fayalite liquid.

The initially solid data are included in the fits to the 3BM/MG and 4BM/MG thermal EOS for the liquid (figure 7). The 4th-order fit recovers these data very well, but only the 3rd-order fit appears justified by the fitting statistics.

The Eulerian finite strain Birch-Murnaghan EOS has been used widely in the literature for describing the volumetric behavior of liquids [*Agee*, 1998; *Y Ai and Lange*, 2008; *Asimow and Ahrens*, 2010; *Bottinga*, 1985; *Lange*, 2007; *Rigden et al.*, 1989; *Suzuki et al.*, 1995; *Tenner et al.*, 2007]; it has thus far proven to be adequate for fitting although it lacks any rigorous basis in theory as an EOS for liquids. The BM formalism has been criticized for its theoretical weakness in giving unphysical interatomic potentials for high K' materials (gases and liquids) [*Hofmeister*, 1993] and for singularities that occur at high temperature and low pressure [*Ghiorso*, 2004]. Consequently, although the BM EOS can fit our data and allows interpolation between experimental points, it should be used only with caution for extrapolation beyond experimental constraints.

It is a difficult task to capture the nature of liquids, which have short-range order but lack long-range order, in a single EOS. Two recent EOS formalisms have been developed specifically for silicate liquids that are both thermodynamically and theoretically self-consistent in their approach to describing the volume behavior at elevated temperatures and pressure: (1) the deKoker and Stixrude fundamental relation (dKSFR) [*de Koker and Stixrude*, 2009] and (2) the

hard sphere equation of state (HSEOS) [*Jing and Karato*, 2011a].

The dKSFR is an extension of the finite strain description given in *Birch* [1952; 1978] but additionally takes into account the thermal free energy contribution and temperature dependence of liquid properties. The thermodynamic variables are self-consistent in that they are derived from a single equation for the Helmholtz energy, and the contributions to the Helmholtz energy are separable [*McQuarrie*, 1984] into an ideal gas term, an excess term, and an electronic term. Recent work by *Muñoz Ramo and Stixrude* [in review] using first principles molecular dynamics (FPMD, GGA+U) of Fe_2SiO_4 liquid obtained a fit with a fourth-order expansion in finite strain and first-order expansion in the reduced temperature using the dKSFR. Their Hugoniot, shown in Figure 7, is in good agreement with our shockwave data. However, contrary to the monotonic increase in γ with increasing pressure inferred from shock wave studies, their results show γ increasing up to a compression of $\rho_o/\rho \approx 0.49$ followed by a decrease in γ coinciding with a change from the high-spin state of Fe.

The HSEOS assigns a hard sphere for each cation species, which move freely in the liquid. The geometrical arrangement of these spheres gives the contribution of entropy to the compression of the liquid [*Jing and Karato*, 2011a]. This formalism does well in explaining the complex behaviors of melts, such as the dependence of γ with pressure. However currently, the calibration of the Fe sphere diameter is based on two experiments within a close range of temperature. Therefore, the Fe sphere diameter dependence on temperature remains somewhat poorly constrained for extreme temperature conditions along the Hugoniot. Calibration would be improved with shock temperature measurements or any other independent measurements of Fe-bearing silicate liquids within a wider temperature range.

Corrections and re-analysis of silicate liquids

Also in this study, the anorthite and diopside liquid data of *Asimow and Ahrens* [2010] were re-analyzed, only sampling the center 3 mm of the arrival top hat. This was motivated by a hydro-code model of shock propagation through our capsule geometry carried out at Lawrence Livermore National Laboratory by J. Nguyen, which indicated that the outer part of the top hat arrival is influenced by edge effects. The corrected BM/MG fits are given in Table 5, and the reanalyzed data points are given in Table 1 of Chapter III. The 4^{th}-order fit for anorthite liquid excludes 3 shots: 382, the highest pressure shot from *Asimow and Ahrens* [2010], due to an abnormally shaped shock arrival; and shots 663 and 672, the highest pressure shots from Rigden [1988] due to possible un-relaxed behavior upon compression. For further discussion of glass-like behavior in anorthite under some shock conditions, see *Asimow and Ahrens* [2010], section 4.4. The re-analysis of diopside liquid excludes 378, the lowest pressure shot from *Asimow and Ahrens* [2010] due to irregular and over-exposed top hat arrival.

Also presented in Table 5 is the corrected forsterite liquid γ_o (which previously contained a sign error), and its subsequent re-fitted 4BM parameters. The entire EOS of forsterite is revised in Chapter III.

IMPLICATIONS

Mixing of oxide volumes at high pressure and temperature; application to a magma ocean liquidus

Our extension of the EOS of fayalite liquid completes the basis set needed for estimation, subject to the assumption of linear mixing, of liquid densities in the full CMASF (CaO-MgO-Al_2O_3-SiO_2-FeO) major element space for mafic to ultramafic liquids at elevated temperatures and pressures. Shockwave experiments completed thus far that span this component space are

forsterite (Fo, Mg_2SiO_4) [*Mosenfelder et al.*, 2007], enstatite (En, $MgSiO_3$) [*Mosenfelder et al.*, 2009], anorthite (An, $CaAl_2Si_2O_8$), diopside (Di, $CaMgSi_2O_6$) [Asimow and Ahrens, 2010], and now also fayalite (Fa, Fe_2SiO_4). All of the EOS parameters for each of these compositions, corrected (see above) or recommended by the original authors, are given in Table 5.The revised EOS are discussed in detail in the subsequent chapter (Tables 3 and 4)

In this study we examine only one simple model of many possible scenarios for the crystallization of an early terrestrial magma ocean. Our initial condition is a well-mixed, convecting liquid composed of one of two plausible bulk silicate Earth compositions — "chondrite" or peridotite — that reaches the base of the mantle. To learn at what depth and critical potential temperature such a whole-mantle magma ocean would begin to crystallize, we used mixtures of silicate liquids in the CMASF system and calculated the intersections or tangency points between isentropes of these two liquid compositions and their respective liquidus curves. The basis of our model is derived from an alternative definition of the Grüneisen parameter,

$$\gamma = (\partial \ln T)/(\partial \ln \rho)_S , \qquad (20)$$

which expresses the adiabatic temperature gradient with increasing density [*Miller et al.*, 1991b]. Figure 8 shows the two mantle compositions that we examined. The first (Fig. 8a) is a synthetic "chondrite" mix [*Andrault et al.*, 2011] with relative proportions of the five major oxides akin to the primitive mantle but lacking any minor components (TiO_2, Na_2O, K_2O… etc.); its major element ratios are similar to pyrolite composition [*Ringwood*, 1975]. The second composition (Fig. 8b) approximates the major oxide composition of KLB-1 peridotite [*Fiquet et al.*, 2010], a fertile spinel lherzolite. We also considered the KLB-1 composition given by *Davis et al.* [2009], but found that the isentropes were nearly indistinguishable from those calculated from the

published composition in *Fiquet et al*. [2010]. Table 6 gives the major oxide proportions for each composition as well as the normalized percent of each end-member liquid used in the model. We also were concerned with what the density contrast of our model liquid would be with its first forming solid—whether it would sink or float. As a conservative measure of where solid flotation is possible, we assumed the liquidus solid to be pure Pv ($MgSiO_3$, magnesium perovskite) using the EOS from *Mosenfelder et al*. [2009]. Mg-rich Pv was the liquidus solid in both *Andrault et al.* [2011] and *Fiquet et al.*[2010] at the pressures of interest.

We determined each CMASF model isentrope for a given potential temperature (T_P) in a stepwise fashion, solving for temperature (T) at each fixed increment of pressure (P) from 0 to 140 GPa. In this calculation, each CMASF isentrope is a combination of the pure end-member isentropes of An, Di, Fo, En, and Fa; and each of the end-member isentropes is defined by its own potential temperature T^i_P (superscript i denotes an end-member mineral), where T^i_P is a separately defined value from the T_P of the CMASF model isentrope. The separate T_P and T^i_P values permit the mixture of the end-member isentropes to define a point on the final CMASF model isentrope in which the total entropy (S_{tot}) remains a constant, such that

$$S_{tot} = \sum_i f^i S^i + S_{mix} = \text{constant}, \tag{21}$$

where f is the mole fraction (Table 6) and S^i is the molar entropy for each end-member in the model liquid. By assuming the entropy of mixing (S_{mix}) is constant for a given liquid composition, the potential temperature of each end-member liquid isentrope (T^i_P) was solved by setting the derivative of the total entropy equal to zero:

$$d\sum_i f^i S^i = \sum_i f^i C_P^i \ln\left(\frac{T_P^i}{T_P}\right) = 0. \tag{22}$$

The potential temperature for each end-member liquid isentrope is further defined as

$$T_P^i = T \exp\left(\frac{\gamma_o^i}{q^i} \left(\frac{V_P^i}{V_o^i} \right)^{q^i} - \left(\frac{V^i}{V_o^i} \right)^{q^i} \right). \quad (23)$$

This expression is derived from (20) by integrating

$$\partial T = \gamma_o \left(\frac{\rho_o}{\rho} \right)^q \frac{T}{\rho} \partial \rho . \quad (24)$$

and is dependent on the following three variables: (1) the temperature at each iteration along the model isentrope (T), (2) the volume of each end member at T and P (V^i), and (3) the volume of each end member at T^i_{P} and 0 GPa (V^i_{P}). These three variables are solved iteratively to satisfy equation (22) and to minimize the expression

$$\sum_i (P_S^i - P) + (P_P^i)^2 , \quad (25)$$

where P^i_{P} is the BM isentropic pressure at T^i_{P} and equals 0 GPa at the target volume V^i_{P} and P^i_{S} is the BM isentropic pressure for each end member at T. Minimization of this expression ensures that the isentropic pressure for each end member converges to the defined pressure in question and that P^i_{P} is in fact equal to 0 GPa. For Fa, we used the BM3 parameters given in Table 4; for all other end members, we used the BM parameters in Table 5. In total, 11 parameters (T and two volumes, V^i and V^i_{P}, for each of the 5 end members) were solved iteratively for each step increment in pressure along a model isentrope.

The densities of the mixtures were calculated using linear mixing of volumes. This assumption has been previously tested for mixing of anorthite and diopside liquids [*Asimow and Ahrens*, 2010] and was found to be well-behaved at high temperatures and pressures but began to break down when applied at low temperatures requiring very large extrapolation downwards from the Hugoniot temperature. Furthermore, anorthite liquid may be a special case due to its highly polymerized structure at low pressure [*Mysen and Richet*, 2005], although we examine

this further in Chapter III. Hence, despite examination of three compositions along the anorthite-diopside join, it remains unclear whether or not linear mixing of volume at high pressure is valid for most mafic to ultramafic silicate liquids. Nevertheless, given five measured compositions in a five-oxide system, the assumption of linear mixing is necessary to make progress at this time and remains consistent with data presently available. We examine this assumption in detail in Chapter IV.

The resulting model for the *Andrault et al.* [2011] "chondrite" mix shows that crystallization would begin at the base of present-day mantle (~135 GPa) with a critical adiabat of T_P = 2600K (Fig 8a). *Andrault et al.* found Pv to be the liquidus phase at all pressures above 60 GPa; therefore we calculated the density for a first forming crystal and found it to be denser than the surrounding liquid (ρ_{Pv}, 5.38 g cm^{-3} > ρ_{liquid}, 5.28 g cm^{-3}). Thus a basal magma ocean similar to that described in *Labrosse et al.* [2007] in which a large portion of the lowermost mantle is zone-refined to concentrate incompatible elements would be unlikely as crystallization of the mantle would occur from the bottom up. A chondritic basal magma ocean is likely only able to exist within the thermal boundary layer (highest estimated outer core of 4150K) [*Hernlund et al.*, 2005] or at the elevated basal temperatures that occurred during early Earth accretion [*Canup*, 2004].

The critical adiabat for the peridotite composition of *Fiquet et al.* (2010), on the other hand, occurs at a higher T_P of 2800 K and, notably, is tangent to the liquidus at 85 GPa (Fig 8b). Consequently crystallization would begin in the middle of the lower mantle. A Pv liquidus phase would, like the model above, sink upon formation (ρ_{Pv}, 4.94 g cm^{-3} > ρ_{liquid}, 4.63 g cm^{-3}). This model is more akin to the picture described in *Labrosse et al.* [2007] as the basal magma ocean would include a portion of the lower mantle which could be used to distill incompatible elements

into a potential present-day ULVZ, yet the sinking liquidus phase if not conducive to the dynamic formation of a basal ocean.

It is worth mentioning that the surface temperatures in both of these models could be too hot for simple, realistic magma ocean models; *Andrault et al.* [2011] suggest that such high foot temperatures would lead to large portions of the mantle vaporizing and rapid cooling if thermal blanketing is inefficient.

Within this exercise, the location of first crystallization is likely dominantly controlled by two factors: (1) the topology of the liquidus curve and (2) the amount of Fo end-member in the model liquid. It is unclear whether different shapes of liquidus curves stem from differing experimental techniques in the two synchrotron-based laser-heated diamond anvil studies considered or instead if they reflect thermodynamic differences within that range of composition space. However, Fig. 8 makes clear that without a notable decrease in slope in the liquidus curve compared to the isentrope at high pressure, crystallization would always be predicted at the base of the mantle (Fig. 8b).

Secondly, it has been observed that the forsterite component has a large control on the spacing and steepness of the isentropes. This behavior can be seen to be true in peridotite, which has a greater fraction of Fo component (Table 6) and has a much steeper isentrope series than the En-rich chondrite liquid (Fig. 8). The effect that Fo has on the isentrope mixing can be predicted from its 1-bar thermodynamic parameters (Table 5) with larger γ_o , α, and K_S. These larger parameters are inversely proportional to the amount of SiO_2 in Fo, since the dV/dT value of SiO_2 at ambient pressure (from which these parameters are derived) is zero [*Lange and Carmichael*, 1990]. The bulk modulus of SiO_2 is notably low compared to other oxides likely because of topological degrees of freedom in tetrahedral framework liquids. Thus the component with the

least SiO_2 gives the largest γ_o, α, and K_S and so the steepest isentrope, which contributes directly to the steepness of the isentrope of the mixture.

In Chapter III, we used the revised EOS of Fo, An, and En to re-model these liquid isentropes (Figure 7). The results are fairly similar, but it is important to note that the γ_o , α, and K_S of forsterite liquids are not as large as modeled by the 1-bar data, and thus forsterite does not play such a dominant role on the steepness of the isentrope. A full discussion is given in Chapter III, section *Isentropes for a full mantle magma ocean*.

We can conclude from this exercise in modeling the Earth's accretion, acknowledging the simplifying assumptions and presumed bulk compositions, that the first crystallizing solid will likely occur within the lower mantle or at the base of the mantle. This is made more likely if early earth core temperatures are assumed to be elevated above current estimates [*Canup*, 2004]. Although largely controlled by the chosen bulk composition, within our exercise the liquidus phase would be Pv and would sink upon formation. Whether pure Mg-Pv is a correct approximation to the liquidus phase, as opposed to a more Fe-rich (Mg,Fe)-Pv, is unclear based on the spread of high *T-P* Fe partitioning values in the current literature (D_{Fe} = 0.6 to > 0.1) [*Andrault et al.*, 2012; *Nomura et al.*, 2011]. Regardless, since pure Pv is the least dense end-member of the (Mg, Fe)SiO_3 solid-solution, greater partitioning of Fe into the solid would only further increase the density and magnitude of the already observed negative buoyancy.

Buoyancy in the current temperature regime; application to the solidus and ULVZ

For long-term gravitational stability, a presumed molten silicate liquid of the ULVZ must be denser than or at least neutrally buoyant compared to the ambient lower-most mantle bulk composition that exists today. Shown in Figure 9 are the densities of fayalite, enstatite and forsterite liquids along a plausible modern mantle adiabat including a thermal boundary

correction, with a potential temperature of 1673 K and a gradient of 10 K/GPa. A pure molten fayalite composition with density of 7 g cm^{-3} would pond at the core mantle boundary if present, as it is much denser than any likely solid assemblage at lowermost mantle conditions. However the model of a pure fayalite liquid ULVZ is inconsistent both with the density of 6.12 g cm^{-3} in the ULVZ inferred from seismic reflection coefficients [*Rost et al.*, 2006] (Figure 9) and with the non-zero shear velocity of this layer. Instead, a less-dense multicomponent partial melt needs to be considered as a plausible state for the ULVZ. Assuming linear mixing of the oxide volumes calculated from the BM EOS given in Tables 4 and 5, Figure 10a displays lines of constant density within a Fa-Fo-En-Fs space (where ferrosilite (Fs) = En+ .5Fo -.5Fa). Figure 10b is the same plot, but uses the revised EOS in Chapter III Tables 3 and 4. The y-axis is Mg# (Mg# = MgO/FeO+MgO), and the x-axis is (MgO+FeO)/SiO_2. The solid curves delineate compositions that are neutrally buoyant with respect to a pure Pv solid at ~135GPa (roughly the pressure at the CMB) at the given temperature conditions (3900 K–4500 K). The dashed lines indicate a constant density of 6.12 g/cm^3, which represents the estimated upper limit of a 10% density jump of an ULVZ [*Rost et al.*, 2006] with respect to PREM [*Dziewonski and Anderson*, 1981]. Any liquid mixture that lies above the solid lines where Pv sinks (white in Fig. 10) is inferred to be gravitationally unstable with respect to upwards percolation into the solid mantle, and any mixture below the dashed lines is denser than has been inferred for ULVZs.

In this exercise, potential liquid compositions for a high-melt fraction ULVZ must span a narrow range in composition space (striped blue in Figure 10), eliminating pure enstatite, and fayalite end-members as candidate compositions. Previously (Fig. 10a), pure forsterite was not denser than coexisting Pv crystal, but in the revised EOS (Fig. 10b), this is no longer shown to be true. For reference, the simplified chondrite and peridotite liquids modeled in the section above

are also plotted on Figure 10. These results indicate that these liquid compositions are unlikely to be gravitationally stable at the CMB today (although peridotite liquid is denser than previously modeled Fig 10b); if residual liquids were to be derived from magma oceans of either composition, they would need to be enriched in Fe, depleted in Si, or both during some process of re-crystallization and distillation from the original bulk mantle. The gray arrows from each composition indicate the direction of compositional evolution if Pv ($MgSiO_3$, En) were to crystallize and be removed. It also gives a rough estimate of what the final liquid composition would need to be for Pv to be buoyant.

When evaluating whether a liquid would be gravitationally stable, Figure 10 assumes that a pure Pv end member is an acceptable estimation for bulk lower mantle density. Adding Fe to the pertinent solid phase in this scenario (modeled as Pv) would qualitatively narrow the region of gravitationally stable liquids to only low Mg# (<0.5) compositions in Fig. 10 (blue-lined area). Also the densities shown here are for fixed compositions that are unlikely to be in chemical equilibrium. For a complete examination of stability, we would need a better grasp on the actual bulk composition of the solid and an understanding of Fe/Mg partitioning at lower mantle conditions. Moreover, it is likely that the bulk lower mantle contains some amount of iron-bearing Pv and calcium-silicate Pv, which would be denser than pure Mg-Pv and also effectively narrow the range of acceptable, stable compositions for a ULVZ liquid shown in Figure 10. Similarly, incorporation of Al_2O_3 and CaO into the model partial melt using the EOS of anorthite and diopside would narrow this same region of Fig. 10 by decreasing the density of the liquid. Therefore, our simplified model in Fig. 10 indicates the minimum amount of Fe enrichment that the liquid must have to be a high-fraction, gravitationally stable silicate melt at the CMB, but the amount of enrichment is likely to be much greater.

CONCLUSIONS

The density for Fe_2SiO_4 liquid as well as values for K and K' have been constrained. Additionally, the Grüneisen parameter for Fe-bearing silicate liquids is shown to change with compression in a manner similar to non-Fe bearing liquids and the opposite to that of solids. Although the Grüneisen parameter has been measured for formulation of a thermal equation state, as with any thermal EOS formalism, there are trade-offs especially when examining states far from the Hugoniot including extrapolations in pressure beyond experimental pressures (161 GPa). Temperature estimates could be greatly improved by either shock temperature measurements or any other off-Hugoniot temperature measurements to constrain $C_{v.}$ Constraints on the end-member liquid fayalite EOS permit interpolation between CMASF silicate liquids densities, assuming linear mixing of volumes. The calculation of isentropes at elevated temperatures and pressures for model whole-mantle magma oceans composed of peridotite and simplified "chondrite" liquid indicate crystallization initiating at the mid-lower mantle (85 GPa) and the base of the mantle, respectively. Finally, a compositional range of gravitationally stable liquids was determined to examine the likelihood of a gravitationally stable ULVZ composed of a large degree of partial melt. There exists a region of melt composition that is denser than Pv at the CMB, but neither chondrite nor peridotite is sufficiently enriched in Fe to be stable. Fractional crystallization of Pv would need to take place before either liquid would be dense enough to remain at the CMB. To elucidate fully the proper stable liquid composition, formulation of multicomponent phase equilibria or partition coefficients at high pressure and temperature are necessary for accurate description of the CMB.

ACKNOWLEDGEMENTS

The authors would like to thank the following: the shock wave lab technical staff—Michael Long, Eprapodito Gelle, and Russel Oliver; additionally, Bjorn Mysen for conducting Mössbauer measurements, and Jeff Nguyen for running simulations of our shock wave experiments. This work was supported by the National Science Foundation through award EAR-0855774.

REFERENCES

Agee, C. B. (1988), Mass balance and phase density constraints on early differentiation of chondritic mantle, *Earth and planetary science letters*, *90*(2), 144.

Agee, C. B. (1992), Isothermal compression of molten Fe_2SiO_4, *Geophys. Res. Lett.*, *19*(11), 1169–1172.

Agee, C. B. (1998), Crystal-liquid density inversions in terrestrial and lunar magmas, *Physics of The Earth and Planetary Interiors*, *107*(1-3), 63-74.

Ahrens, T. J. (1987), 6. Shock Wave Techniques for Geophysics and Planetary Physics, in *Methods in Experimental Physics*, edited by G. S. Charles and L. H. Thomas, pp. 185-235, Academic Press.

Ai, Y and R. A. Lange (2004), An ultrasonic frequency sweep interferometer for liquids at high temperature: 2. Mechanical assembly, signal processing, and application, *J. Geophys. Res.*, *109*(B12204).

Ai, Y., and R. A. Lange (2008), New acoustic velocity measurements on CaO-MgO-Al_2O_3 SiO_2 liquids: Reevaluation of the volume and compressibility of $CaMgSi_2O_6$-$CaAl_2Si_2O_8$ liquids to 25 GPa, *J. Geophys. Res.*, *113*(B4), B04203.

Akins, J. A. (2002), Dynamic compression of SiO_2: A new interpretation, *Geophysical research letters*, *29*(10), 31.

Akins, J. A., S.-N. Luo, P. D. Asimow, and T. J. Ahrens (2004), Shock-induced melting of $MgSiO_3$ perovskite and implications for melts in Earth's lowermost mantle, *Geophys. Res. Lett.*, *31*(14), L14612.

Andrault, D., N. Bolfan-Casanova, G. L. Nigro, M. A. Bouhifd, G. Garbarino, and M. Mezouar (2011), Solidus and liquidus profiles of chondritic mantle: Implication for melting of the Earth across its history, *Earth and planetary science letters*, *304*(1-2), 251-259.

Andrault, D., S. Petitgirard, G. Lo Nigro, J.-L. Devidal, G. Veronesi, G. Garbarino, and M. Mezouar (2012), Solid-liquid iron partitioning in Earth's deep mantle, *Nature*, *487*(7407), 354-357.

Asimow, P. D., and T. J. Ahrens (2010), Shock compression of liquid silicates to 125 GPa: The anorthite-diopside join, *J. Geophys. Res.*, *115*(B10), B10209.

Asimow, P. D., D. Sun, and T. J. Ahrens (2008), Shock compression of preheated molybdenum to 300 GPa, *Physics of The Earth and Planetary Interiors*, *174*(1-4), 302.

Birch, F. (1947), Finite Elastic Strain of Cubic Crystals, *Physical review*, *71*(11), 809.

Birch, F. (1952), Elasticity and constitution of the Earth's interior, *J. Geophys. Res.*, *57*(2), 227 286.

Birch, F. (1978), Finite strain isotherm and velocities for single-crystal and polycrystalline NaCl at high pressures and 300K, *J. Geophys. Res.*, *83*(B3), 1257-1268.

Bottinga, Y. (1985), On the isothermal compressibility of silicate liquids at high pressure, *Earth and planetary science letters*, *74*(4), 350-360.

Canup, R. M. (2004), Simulations of a late lunar-forming impact, *Icarus*, *168*(2), 433-456.

Chen, G. Q., and T. J. Ahrens (Eds.) (1998), *Radio frequency heating coils for shock wave experiments*, 63-71 pp., Materials Research Society Symposia Proceedings, Warrendale, PA.

Chen, G. Q., T. J. Ahrens, and E. M. Stolper (2002), Shock-wave equation of state of molten and solid fayalite, *Physics of The Earth and Planetary Interiors*, *134*(1-2), 35-52.

Circone, S., and C. B. Agee (1996), Compressibility of molten high-Ti mare glass: Evidence for

crystal-liquid density inversions in the lunar mantle, *Geochimica et Cosmochimica Acta*, *60*(14), 2709-2720.
Davis, F. A., J. A. Tangeman, T. J. Tenner, and M. M. Hirschmann (2009), The composition of KLB-1 peridotite, *American Mineralogist*, *94*(1), 176-180.
de Koker, N., and L. Stixrude (2009), Self-consistent thermodynamic description of silicate liquids, with application to shock melting of MgO periclase and $MgSiO_3$ perovskite, *Geophysical Journal International*, *178*(1), 162 Erratum Ibid., doi: 110.1111/j.1365-1246X.2010.04739.x.
Dziewonski, A. M., and D. L. Anderson (1981), Preliminary reference Earth model, *Physics of The Earth and Planetary Interiors*, *25*(4), 297-356.
Efron, B. (Ed.) (1982), *The Jackknife, the Bootstrap, and Other Resampling Plans*, 92 pp., Philadelphia, PA.
Fiquet, G., A. L. Auzende, J. Siebert, A. Corgne, H. Bureau, H. Ozawa, and G. Garbarino (2010), Melting of Peridotite to 140 Gigapascals, *Science*, *329*(5998), 1516-1518.
Garnero, E. J., and D. V. Helmberger (1995), A very slow basal layer underlying large-scale low-velocity anomalies in the lower mantle beneath the Pacific: evidence from core phases, *Physics of The Earth and Planetary Interiors*, *91*(1-3), 161-176.
Ghiorso, M. S. (2004), An equation of state for silicate melts. III. Analysis of stoichiometric liquids at elevated pressure: shock compression data, molecular dynamics simulations and mineral fusion curves, *Am J Sci*, *304*(8-9), 752-810.
Ghiorso, M. S., and R. O. Sack (1995), Chemical mass transfer in magmatic processes IV. A revised and internally consistent thermodynamic model for the interpolation and extrapolation of liquid-solid equilibria in magmatic systems at elevated temperatures and pressures, *Contributions to Mineralogy and Petrology*, *119*(2), 197-212.
Hernlund, J. W., C. Thomas, and P. J. Tackley (2005), A doubling of the post-perovskite phase boundary and structure of the Earth's lowermost mantle, *Nature*, *434*(7035), 882-886.
Hofmeister, A. M. (1993), Interatomic potentials calculated from equations of state: Limitation of finite strain to moderate K', *Geophys. Res. Lett.*, *20*(7), 635-638.
Holloway, J. R., V. Pan, and G. Gudmundsson (1992), High-pressure fluid-absent melting experiments in the presence of graphite; oxygen fugacity, ferric/ferrous ratio and dissolved CO 2, *European Journal of Mineralogy*, *4*(1), 105-114.
Jackson, I., and T. J. Ahrens (1979), Shock wave compression of single-crystal forsterite, *Journal Name: J. Geophys. Res.; (United States); Journal Volume: 84:B6*, Medium: X; Size: Pages: 3039-3048.
Jakobsson, S., and N. Oskarsson (1994), The system C-O in equilibrium with graphite at high pressure and temperature: An experimental study, *Geochimica et Cosmochimica Acta*, *58*(1), 9-17.
Janz, G. (1980), Molten Salts Data as Reference Standards for Density, Surface Tension, Viscosity, and Electrical Conductance: KNO3 and NaCl, *Journal of Physical and Chemical Reference Data*, *9*(4), 791.
Jeanloz, R. (1989), Shock Wave Equation of State and Finite Strain Theory, *J. Geophys. Res.*, *94*.
Jing, Z., and S.-i. Karato (2011a), A new approach to the equation of state of silicate melts: An application of the theory of hard sphere mixtures, *Geochim. Cosmochim. Acta*.
Labrosse, S., J. W. Hernlund, and N. Coltice (2007), A crystallizing dense magma ocean at the base of the Earth/'s mantle, *Nature*, *450*(7171), 866-869.

Lange, R. A. (2007), The density and compressibility of $KAlSi_3O_8$ liquid to 6.5 GPa, *American Mineralogist*, *92*(1), 114-123.

Lange, R. A., and I. S. E. Carmichael (1987), Densities of Na_2O-K_2O-MgO-MgO-FeO-Fe_2O_3 Al_2O_3-TiO_2-SiO_2 liquids: New measurements and derived partial molar properties, *Geochimica et Cosmochimica Acta*, *51*(11), 2931-2946.

Lange, R. A., and I. S. E. Carmichael (1990), Thermodynamic properties of silicate liquids with emphasis on density, thermal expansion and compressibility, *Reviews in Mineralogy and Geochemistry*, *24*(1), 25-64.

Lange, R. A., and A. Navrotsky (1992), Heat capacities of Fe2O3-bearing silicate liquids, *Contributions to Mineralogy and Petrology*, *110*(2-3), 311.

Lay, T., E. J. Garnero, and Q. Williams (2004), Partial melting in a thermo-chemical boundary layer at the base of the mantle, *Physics of The Earth and Planetary Interiors*, *146*(3-4), 441-467.

Lyzenga, G. A. (1983), Shock temperatures of SiO2 and their geophysical implications, *Journal of geophysical research*, *88*(B3), 2431.

Mao, W. L., H.-k. Mao, W. Sturhahn, J. Zhao, V. B. Prakapenka, Y. Meng, J. Shu, Y. Fei, and R. J. Hemley (2006), Iron-Rich Post-Perovskite and the Origin of Ultralow-Velocity Zones, *Science*, *312*(5773), 564-565.

McQuarrie, D. A. (1984), *Statistical Mechanics*, University Science Books, Sausalito, CA.

Médard, E., C. A. McCammon, J. A. Barr, and T. L. Grove (2008), Oxygen fugacity, temperature reproducibility, and H2O contents of nominally anhydrous piston-cylinder experiments using graphite capsules, *American Mineralogist*, *93*(11-12), 1838-1844.

Miller, G. H., T. J. Ahrens, and E. M. Stolper (1988), The equation of state of molybdenum at 1400 C, *Journal of Applied Physics*, *63*(9), 4469-4475.

Miller, G. H., E. M. Stolper, and T. J. Ahrens (1991a), The Equation of State of a Molten Komatiite 1 Shock Wave Compression to 36 GPa, *J. Geophys. Res.*, *96*.

Miller, G. H., E. M. Stolper, and T. J. Ahrens (1991b), The Equation of State of a Molten Komatiite 2. Application to Komatiite Petrogenesis and the Hadean Mantle, *J. Geophys. Res.*, *96*.

Mitchell, A. C., and W. J. Nellis (1981a), Diagnostic system of the Lawrence Livermore National Laboratory two-stage light-gas gun, *Review of scientific instruments*, *52*(3), 347.

Mitchell, A. C., and W. J. Nellis (1981b), Shock compression of aluminum, copper, and tantalum, *Journal of Applied Physics*, *52*(5), 3363-3374.

Mosenfelder, J. L., P. D. Asimow, and T. J. Ahrens (2007), Thermodynamic properties of Mg_2SiO_4 liquid at ultra-high pressures from shock measurements to 200 GPa on forsterite and wadsleyite, *J. Geophys. Res.*, *112*.

Mosenfelder, J. L., P. D. Asimow, D. J. Frost, D. C. Rubie, and T. J. Ahrens (2009), The $MgSiO_3$ system at high pressure: Thermodynamic properties of perovskite, postperovskite, and melt from global inversion of shock and static compression data, *J. Geophys. Res.*, *114*.

Muñoz Ramo, D., and L. Stixrude (in review), Spin crossover in Fe_2SiO_4 liquid at high pressure, *Physical Review Letters*.

Mysen, B. O., and P. Richet (2005), *Silicate Glasses and Melts: Properties and Structure*, 544., Elsevier, Amsterdam.

Nomura, R., H. Ozawa, S. Tateno, K. Hirose, J. Hernlund, S. Muto, H. Ishii, and N. Hiraoka

(2011), Spin crossover and iron-rich silicate melt in the Earth's deep mantle, *Nature*, *473*(7346), 199-202.
Rigden, S. M., T. J. Ahrens, and E. M. Stolper (1984), Densities of liquid silicates at high pressures, *Science*, *226*(4678), 1071-1074.
Rigden, S. M., T. J. Ahrens, and E. M. Stolper (1988), Shock compression of molten silicate: results for a model basaltic composition, *J. Geophys. Res.*, *93*(B1), 367-382.
Rigden, S. M., T. J. Ahrens, and E. M. Stolper (1989), High-Pressure Equation of State of Molten Anorthite and Diopside, *Journal of Geophysical Research*, *94*(B7), 9508-9522.
Ringwood, A. E. (1975), Composition and Petrology of the Earth's Mantle, edited, p. 618, McGraw-Hill, New York.
Rost, S., E. J. Garnero, and Q. Williams (2006), Fine-scale ultralow-velocity zone structure from high-frequency seismic array data, *J. Geophys. Res.*, *111*(B9), B09310.
Ruoff, A. (1967), Linear Shock-Velocity-Particle-Velocity Relationship, *Journal of Applied Physics*, *38*(13), 4976.
Stixrude, L., and B. Karki (2005), Structure and Freezing of $MgSiO_3$ Liquid in Earth's Lower Mantle, *Science*, *310*(5746), 297-299.
Stixrude, L., and C. Lithgow-Bertelloni (2005), Thermodynamics of mantle minerals – I. Physical properties, *Geophysical Journal International*, *162*(2), 610-632.
Stolper, E., D. Walker, B. H. Hager, and J. F. Hays (1981), Melt Segregation From Partially Molten Source Regions: The Importance of Melt Density and Source Region Size, *J. Geophys. Res.*, *86*.
Suzuki, A., E. Ohtani, and T. Kato (1995), Floatation of diamond in mantle melt at high pressure, *Science*, *269*(5221), 216-218.
Svendsen, B., and T. J. Ahrens (1990), Shock-Induced Temperatures of $CaMgSi_2O_6$, *J. Geophys. Res.*, *95*(B5), 6943-6953.
Takei, H. (1978), Growth of fayalite (Fe_2SiO_4) single crystals by the floating-zone method, *Journal of Crystal Growth*, *43*(4), 463-468.
Tenner, T. J., R. A. Lange, and R. T. Downs (2007), The albite fusion curve re-examined: New experiments and the high-pressure density and compressibility of high albite and $NaAlSi_3O_8$ liquid, *American Mineralogist*, *92*(10), 1573-1585.
Ulmer, P., and R. Luth (1991), The graphite-COH fluid equilibrium in P, T, & fO2 space, *Contributions to Mineralogy and Petrology*, *106*(3), 265-272.
Wicks, J. K., J. M. Jackson, and W. Sturhahn (2010), Very low sound velocities in iron-rich (Mg, Fe) O: Implications for the core-mantle boundary region, *Geophysical research letters*, *37*(15), 15304.
Williams, Q., J. Revenaugh, and E. J. Garnero (1998), A Correlation Between Ultra-Low Basal Velocities in the Mantle and Hot Spots, *Science*, *281*(5376), 546-549.

TABLES

Table 1. Double-bob density measurements

T (K)	ρ g cm^{-3}	±
1551	3.710	0.002
1632	3.679	0.002
1723	3.652	0.002
1818	3.630	0.001

Table 2. Shock compression data

	Shot #	Flyer/ Driver	T (°C)	u_{fp} km s^{-1}	±	u_p km s^{-1}	±	U_s km s^{-1}	±	ρ_H g cm^{-3}	±	P_H GPa	±
Chen et al. (2002)	999[a]	Al2024/ Al2024	25	1.96	0.001	0.754	0.26	7.05	0.26	4.90	0.03	23.3	0.4
	1000[a]	W/Al2024	25	2.03	0.01	1.51	0.18	6.95	0.18	5.61	0.05	46.2	0.9
	110	Cu/Cu	25	4.63	0.01	2.87	0.08	8.2	0.08	6.76	0.05	103.3	0.8
	120	Cu/Cu	25	5.30	0.002	3.29	0.08	8.71	0.08	7.00	0.06	124.7	0.8
	116	Ta/Ta	25	5.171	0.006	3.58	0.11	9.02	0.11	7.26	0.06	141.4	1.7
	113	Ta/Ta	25	5.38	0.005	3.69	0.17	9.44	0.17	7.21	0.1	153.0	2.1
	099	Ta/Ta	25	5.77	0.01	3.95	0.05	9.79	0.05	7.34	0.03	169.4	0.7
	107	Ta/Ta	25	6.25	0.001	4.27	0.1	10.15	0.1	7.59	0.07	190.5	1.5
	161	Ta/Ta	25	6.494	0.001	4.44	0.11	10.33	0.11	7.65	0.06	200.3	2.1
	126	Ta/Ta	25	6.51	0.005	4.57	0.1	10.57	0.1	7.73	0.08	211.9	1.6
This work	412	Ta/Ta	25	7.085	0.012	4.864	0.019	10.90	0.04	7.81	0.07	229.2	2.1
Chen et al. (2002)	995	Al2024/ Mo	1300	1.05	0.004	0.43	0.02	3.23	0.02	4.33	0.12	5.25	0.03
	996	Al2024/ Mo	1300	1.95	0.01	0.81	0.01	3.91	0.31	4.73	0.05	11.9	0.7
	981	Ta/Mo	1300	1.52	0.02	1.24	0.02	4.72	0.01	5.09	0.03	21.9	0.3
	993	Ta/Mo	1300	1.890	0.002	1.53	0.08	4.94	0.01	5.43	0.14	28.3	1.5
	990	Ta/Mo	1300	2.00	0.02	1.63	0.04	4.92	0.54	5.61	0.34	30.1	2.5
	994	Ta/Mo	1300	2.52	0.01	1.99	0.01	5.82	0.01	5.70	0.02	43.4	0.2
	998	W/Mo	1300	2.50	0.01	2.17	0.02	5.85	0.14	5.96	0.1	47.6	0.9
This work	396	Ta/Mo	1299	4.997	0.003	3.82	0.003	8.45	0.03	6.76	0.02	119.5	0.3
	409	Ta/Mo	1300	6.050	0.002	4.58	0.01	9.50	0.05	7.15	0.04	161.0	0.6

[a] 40mm shots on Caltech polycrystalline fayalite

Table 3. Parameters used

	Units	Fe_2SiO_4 liquid (1573 K)	Molybdenum[d] (1573 K)	Tantalum[e] (300 K)
$\Delta E_{tr} \approx \Delta H_{tr}$	kJ kg^{-1}	-1584.2194[a]	-	-
α	K^{-1}	8.1949e-05[b]	-	-
C_p	J kg^{-1} K^{-1}	1182.35[c]	-	-
C_v	J kg^{-1} K^{-1}	1123.13[c]	-	-
ρ_o	g cm^{-3}	-	9.96	16.65
C_o	km s^{-1}	-	4.927	3.293
s		-	1.288	1.307

[a]*Ghiorso and Sack* [1995] [b]derived from this work, (see text and Table 1 for dV/dT) [c]*Lange and Navrotsky* [1992] [d]*Asimow et al.* [2008] [e]*Mitchell and Nellis* [1981]

Table 4. Equation of state fits for molten Fe_2SiO_4

	Units	SWEOS	SWEOS*	3BM/MG	4BM/MG	Source
T_o	K	1573	1573	1573	1573	
ρ_o	g cm^{-3}	3.699	3.699	3.699	3.699	this work
C_o	m s^{-1}	2438±5	2670±8			AL04
s		1.58 ± 0.03	1.50±0.03			fitted
γ_o		0.412	0.412	0.412	0.412	derived
q		-1.45	-1.04	-0.95	-0.55	fitted
K_{oS}	GPa	21.99	26.38	21.99	21.99	derived
K_S'		5.33	4.99	7.28	6.64	fitted
K_S''	GPa^{-1}				-0.47	fitted
χ^2				1.526	0.941	

SWEOS= shock wave equation of state. SWEOS*= shockwave EOS derived from the unconstrained linear fit (see text). 3BM/MG = 3rd order Birch-Murnaghan isentrope. 4BM/MG = 4th order Birch-Murnaghan isentrope. Sources: *Fitted* indicates an adjustable parameter, AL04 is *Ai and Lange* [2004]

Table 5. BM/MG fits for silicate liquid

	Units	Fo 4BM[a]	En 4BM[b]	An 4BM[c]	Di 3BM[c]	Source
T_o	K	1673	1673	1673	1673	
ρ_o	g cm^{-3}	2.825	2.618	2.584	2.643	LC90; L97
γ_o		0.816	0.365	0.18	0.49	LC90
q		-1.47	-1.71	-1.71[d]	-1.28	fitted
K_S	GPa	42.19	24.66	20.39	24.57	derived
K_S'		4.73	9.18	2.31	6.98	derived
K_S'	GPa^{-1}	-0.11	-1.87	0.60		fitted
C_P	J K^{-1} kg^{-1}	1926.18	1761.15	1528.72	1612.56	LN92
C_V	J K^{-1} kg^{-1}	1684.30	1690.54	1512.56	1506.21	derived

[a] corrected γ_o and refit to 4BM [b] from *Mosenfelder et al.* [2009] [c] resampled shock arrivals and refit to BM and excluding some shots, see text. [d] fixed q value LC90 is *Lange and Carmichael* [1990]; L97 is *Lange* [1997]; LN92 is *Lange and Navrotsky* [1992].

Table 6. Major oxide proportions for model mantle

	"chondrite" Andrault et al. (2011)	*KLB-1* Fiquet et al. (2010)	*KLB-1* Davis et al. (2010)
	mol %	mol %	mol %
CaO	2.6	1.5	2.8
MgO	45.9	53.7	50.8
Al_2O	1.8	1.2	1.8
SiO_2	43.5	38.3	38.7
FeO	6.2	5.3	5.9
	mol %	mol %	mol %
Di	1.95	0.70	2.93
An	4.40	3.32	4.98
Fa	7.57	7.16	8.25
Fo	24.2	56.1	55.0
En	61.9	32.7	28.8

FIGURE CAPTIONS

Figure 1. A comparison of previous static sink/float and shock wave compression methods on fayalite liquid. The purple dashed line is an extrapolation of the 1773K isotherm from *Agee* [1992] with K_T'=10.1. The blue solid line is the fayalite liquid Hugoniot from *Chen et al.* [2002] with K_S'=5.36. Estimated shock temperatures are from *Chen et al.* [2002].

Figure 2. (a) Static image of the back of the molybdenum sample holder inverted 90 degrees clockwise such that the top is to the left. The centermost circle is the sample chamber or "top hat"; the guy wire posts are the smaller circles to the left and right. The vertical yellow lines correspond to the portion of the drivers (two outside lines) and the top hat (center line) that are sampled for shock wave arrival cutoffs. The bright vertical line is a superposed static image of the 25 micron slit in position. (b) On the streak image, the y-coordinate corresponds to position along the slit image in (a) where the x-coordinate is time increasing to the right. Yellow lines denote observed shock arrivals. Blue dashed lines are the 4^{th}-order polynomial extrapolation of the shape of shock front from the drivers. The calibration streak shown at bottom converts an x-coordinate on the photo to a time during the experiment, giving the time between the shock wave passing from driver into sample (red line) and reaching the free surface of the top hat (rightmost yellow line). (c) An enlarged view of the top hat arrival with examples of pixel gray scale value vs. distance along the time axis profiles on the right. The arrival point is picked as the inflection point of the arc tangent function fit (black lines). The amplitude of the arctangent functions is arbitrary.

Figure 3. The double-bob density measurements between 1551 and 1831 K, plotted against temperature, are fit by the line $\rho(T) = 3699\pm1 - 0.30\pm0.01*(T\text{-}1573\ \text{K})$.

Figure 4. Density versus pressure diagram showing the new multi-anvil sink/float results for fayalite liquid at 1500°C. "Up" triangles represent observed floats, in which the fayalite liquid was denser than the mineral marker buoy. No sinks were accomplished in the new study. The green curve is the calculated compression for the spessartine garnet marker; the blue curve is the calculated compression for the almandine-rich garnet marker. Fayalite liquid density at 1-bar is from this study (purple diamond) determined by the Archimedean technique. The dashed and dotted curves are the compression curves calculated for fayalite liquid at 1500°C using the K from ultrasonic data [*Ai and Lange*, 2004] and the K' derived from the shock wave EOS and the 3rd-order Birch-Murnaghan EOS in this study, respectively (see Table 4). The thin purple solid curve is the compression curve for liquid fayalite from *Agee* [1992]. Float observations should plot below the correct liquid compression curve.

Figure 5. Preheated (1573K) fayalite Hugoniot in shock velocity (U_s)-particle velocity (u_p) space. Blue circles at the highest velocities were performed in this study. The red filled squares are taken from *Chen et al.* [2002] and were fit with the dotted blue line given in that study. The red solid line is the unconstrained un-weighted linear fit for all data points, and the light green solid line is the constrained un-weighted linear fit for all data points where the intercept is fixed at the bulk sound speed of liquid fayalite measured at 1573K. The hollow symbols are the initially solid experiments (300K) that were shocked to liquid from *Chen et al.* [2002] (hollow red

squares) and this work (hollow blue circle). The dashed green line represents a cold Hugoniot offset from the fitted hot liquid Hugoniot using the derived model for the liquid Grüneisen parameter.

Figure 6. The behavior of Grüneisen parameter for liquid and solid silicates with compression. The reference densities for the liquids (solid lines) are at 1673K for $MgSiO_3$ [*Mosenfelder et al*., 2009] and Mg_2SiO_4 [*Mosenfelder et al.* 2009, corrected in this chapter] and at 1573 K for Fe_2SiO_4 (this study). The gamma functions for the solid materials are shown by dashed lines: magnesium perovskite (Pv) [*Mosenfelder et al.* 2009]-"BM3S model"; majorite (Mj) and enstatite (En) [*Stixrude and Lithgow-Bertelloni*, 2005].

Figure 7. Hugoniot data plotted in pressure-density space with thermal EOS fits for fayalite liquid and shock-melted single crystal all fixed at the Archimedean density at zero pressure. Data symbols are the same as Figure 5. Abbreviations: SWEOS- shock wave equation of state; BM/MG – Birch-Murnaghan/Mie-Grüneisen EOS; dKSFR- de Koker –Stixrude fundamental relation

Figure 8. Models for the early mantle upon cooling showing the comparison of the liquidus curves (black solid line) with the isentropic temperature profile (dotted line) of the same composition. (a) "Chondritic" composition and liquidus from *Andrault et al*. [2011]. (b) Peridotite KLB-1 composition and liquidus from *Fiquet et al.* [2010]. The critical isentrope with

its mantle potential temperature is shown in red. The EOS parameters used for En, Fo, An, and Di are given in Table 5 and Fa 3BM/MG parameters in Table 4. This figure is redone with the revised EOS in Chapter III Figure 8.

Figure 9. Calculated densities as function of pressure along a 10K/GPa mantle geotherm. The density at base of mantle (135 GPa) for each composition is thermally corrected from 3073K to 4400K (shaded cones). Also shown is the density profile from PREM [*Dziewonski and Anderson*, 1981] and the inferred density for a ULVZ from seismic reflection coefficients [*Rost et al.* 2006]. This figure is redone with the revised EOS in Chapter III Figure 9.

Figure 10. The density of liquid mixtures within En-Fs-Fo-Fa space at 135 GPa. The solids lines represent liquid mixtures that are neutrally buoyant with respect to solid magnesium perovskite (Pv) at different core-mantle-boundary temperatures from 3700-4500K. Any liquid compositions above these lines are less dense than Pv (white area) and any below are denser (blue striped area). Constant density lines for liquid compositions at 6.12 g/cc (dashed lines) represent the upper density limit for ULVZ's inferred from *Rost et al.* [2006]. The blue C represents the "chondrite" composition from used in *Andrault et al.* [2011], and the yellow P is the peridotite composition from *Fiquet et al.* [2010]. Both compositions are given in Table 6. The gray arrows indicate the direction of liquid composition change with fractional crystallization of Pv (disregarding partitioning of Fe). a) The EOS parameters used for En and Fo are given in Table 5 and Fa 3BM parameters in Table 4. b) The EOS parameters used for En and Fa are given in Table 4 and Fo 3BM parameters in Table 3 of Chapter III.

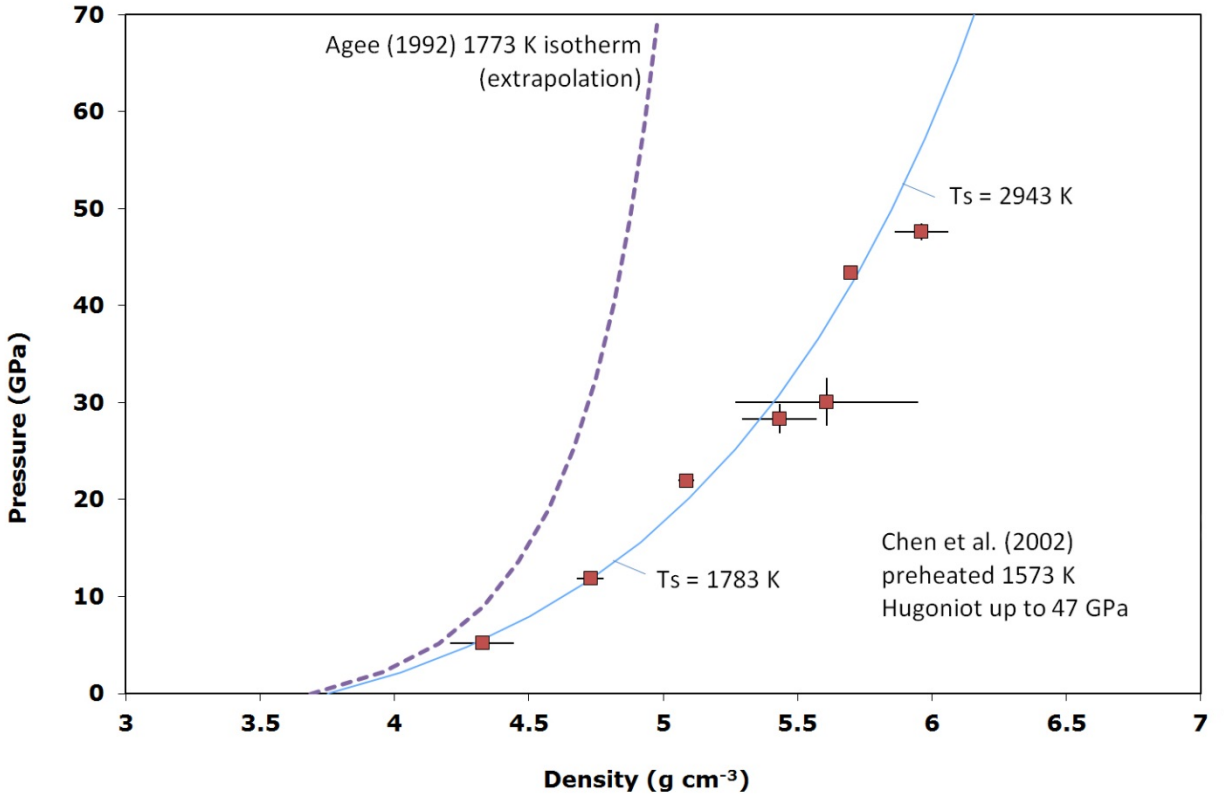
Agee (1992) 1773 K isotherm
(extrapolation)
Ts = 2943 K
Ts = 1783 K
Chen et al. (2002)
preheated 1573 K
Hugoniot up to 47 GPa
Pressure (GPa)
Density (g cm-3)
0
10
20
30
40
50
60
70
3
3.5
4
4.5
5
5.5
6
6.5
7

Figure 1

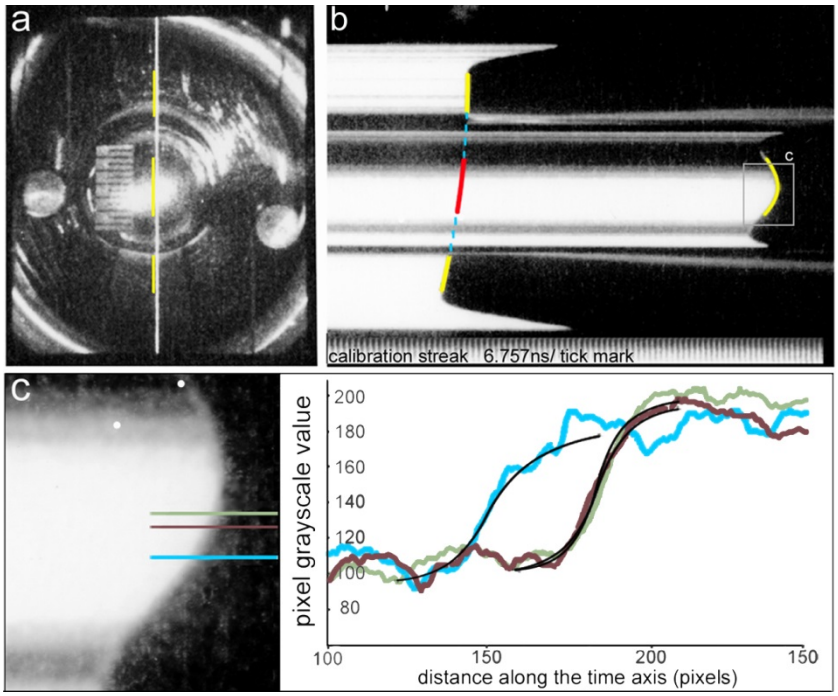
a
b
c
calibration streak 6.757ns/ tick mark
c
pixel grayscale value
200
180
160
140
120
100
80
100
150
200
150
distance along the time axis (pixels)

Figure 2

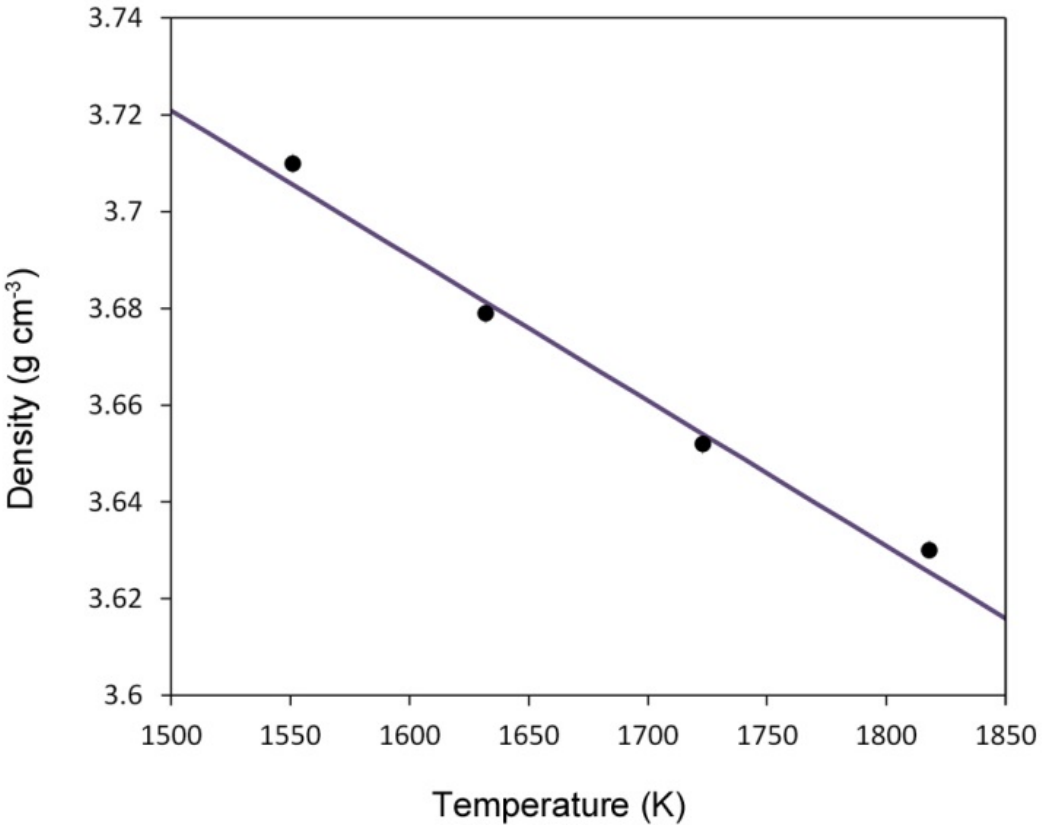
3.74
3.72
3.7
3.68
3.66
3.64
3.62
3.6
Density (g cm-3)
1500
1550
1600
1650
1700
1750
1800
1850
Temperature (K)

Figure 3

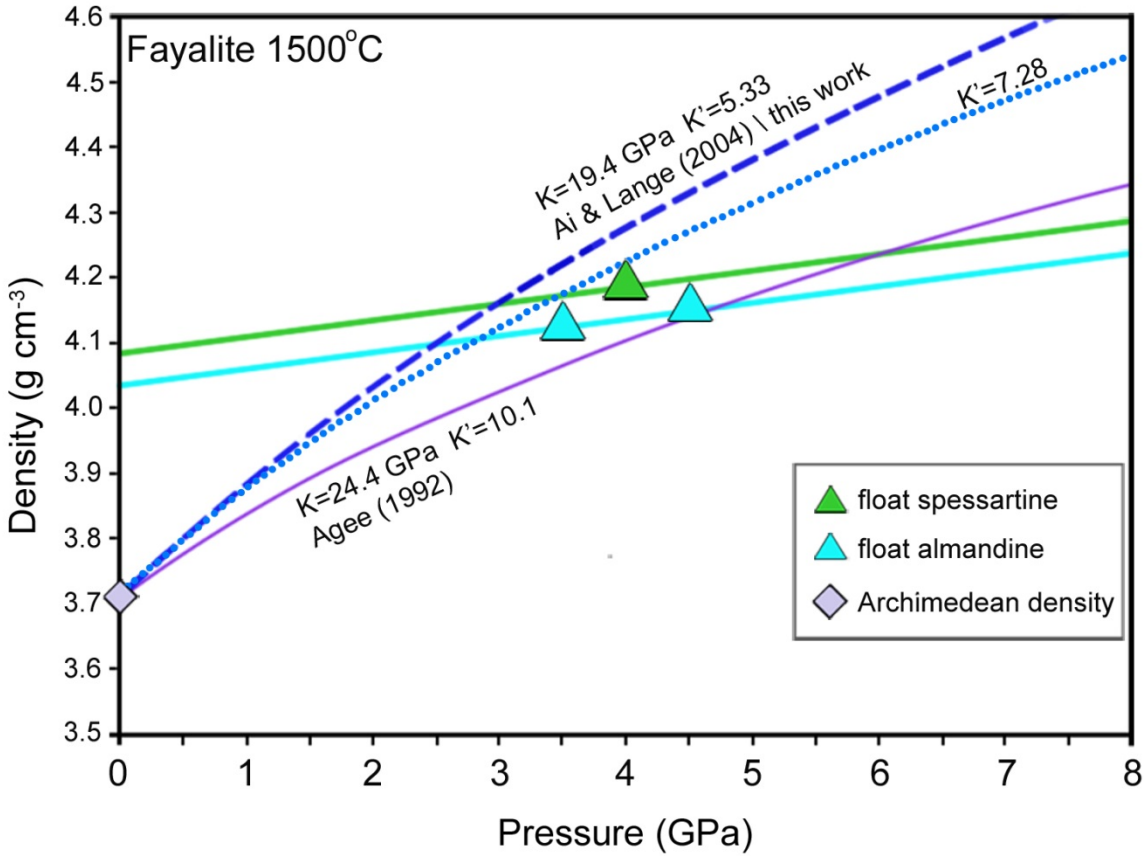
Fayalite 1500°C
K=19.4 GPa K'=5.33
Ai & Lange (2004) \ this work
K'=7.28
K=24.4 GPa K'=10.1
Agee (1992)
float spessartine
float almandine
Archimedean density
Density (g cm-3)
Pressure (GPa)
4.6
4.5
4.4
4.3
4.2
4.1
4.0
3.9
3.8
3.7
3.6
3.5
0
1
2
3
4
5
6
7
8

Figure 4

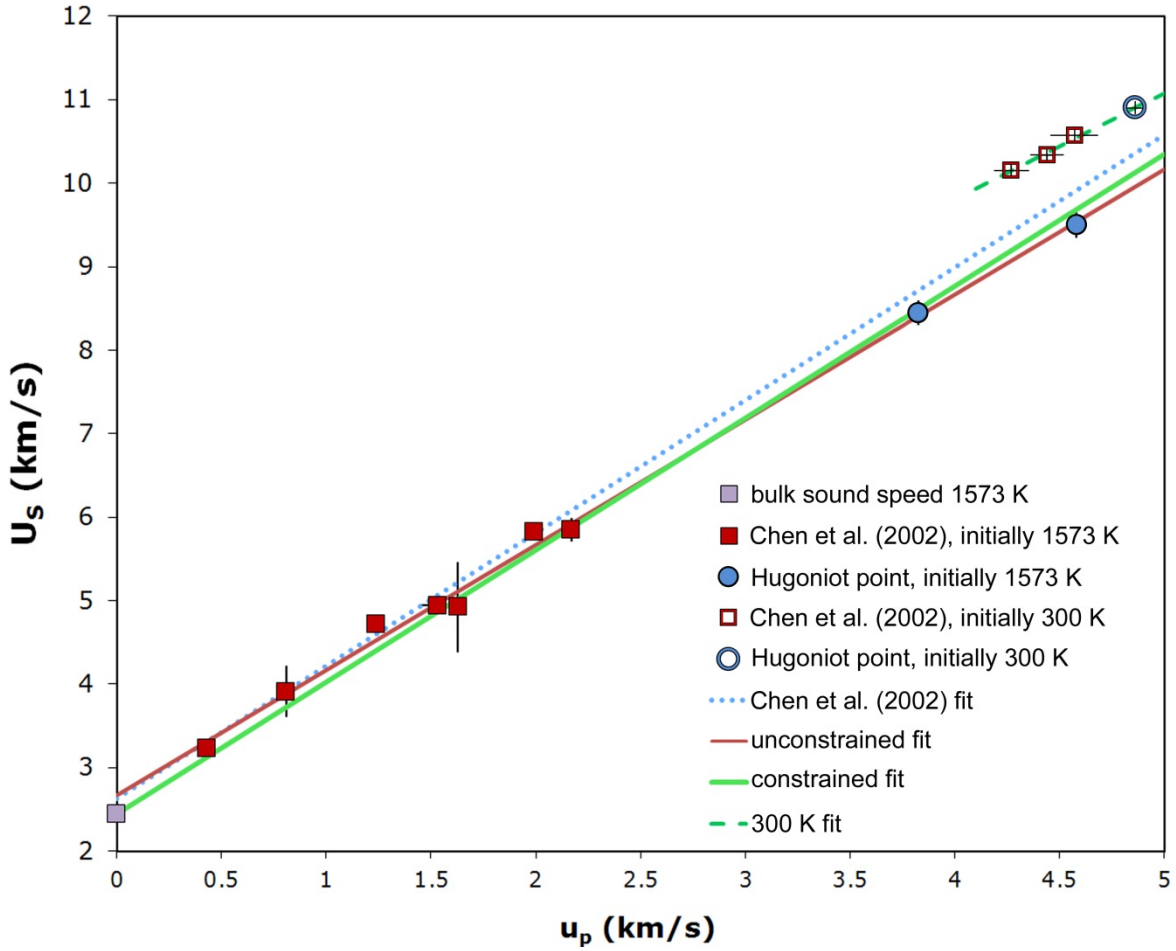
12
11
10
9
8
7
6
5
4
3
2
0
0.5
1
1.5
2
2.5
3
3.5
4
4.5
5
U_S (km/s)
u_p (km/s)
bulk sound speed 1573 K
Chen et al. (2002), initially 1573 K
Hugoniot point, initially 1573 K
Chen et al. (2002), initially 300 K
Hugoniot point, initially 300 K
Chen et al. (2002) fit
unconstrained fit
constrained fit
300 K fit

Figure 5

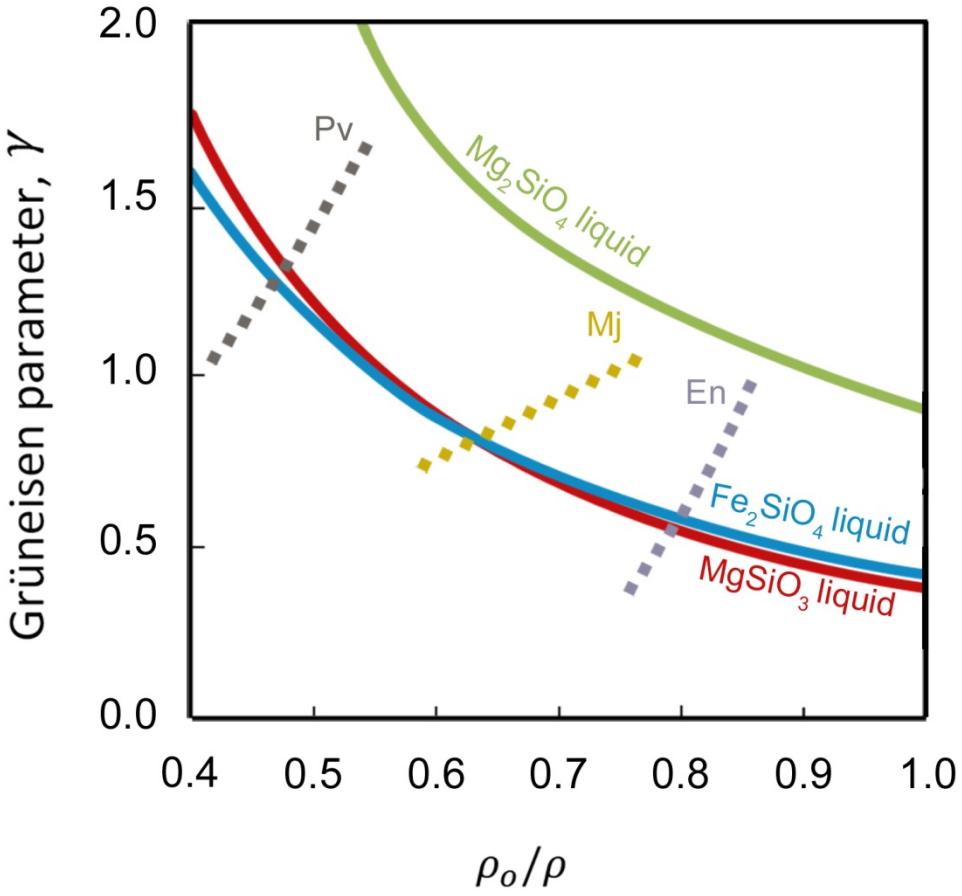
2.0
1.5
1.0
0.5
0.0
Grüneisen parameter, γ
0.4
0.5
0.6
0.7
0.8
0.9
1.0
ρo/ρ
Pv
Mg2SiO4 liquid
Mj
En
Fe2SiO4 liquid
MgSiO3 liquid

Figure 6

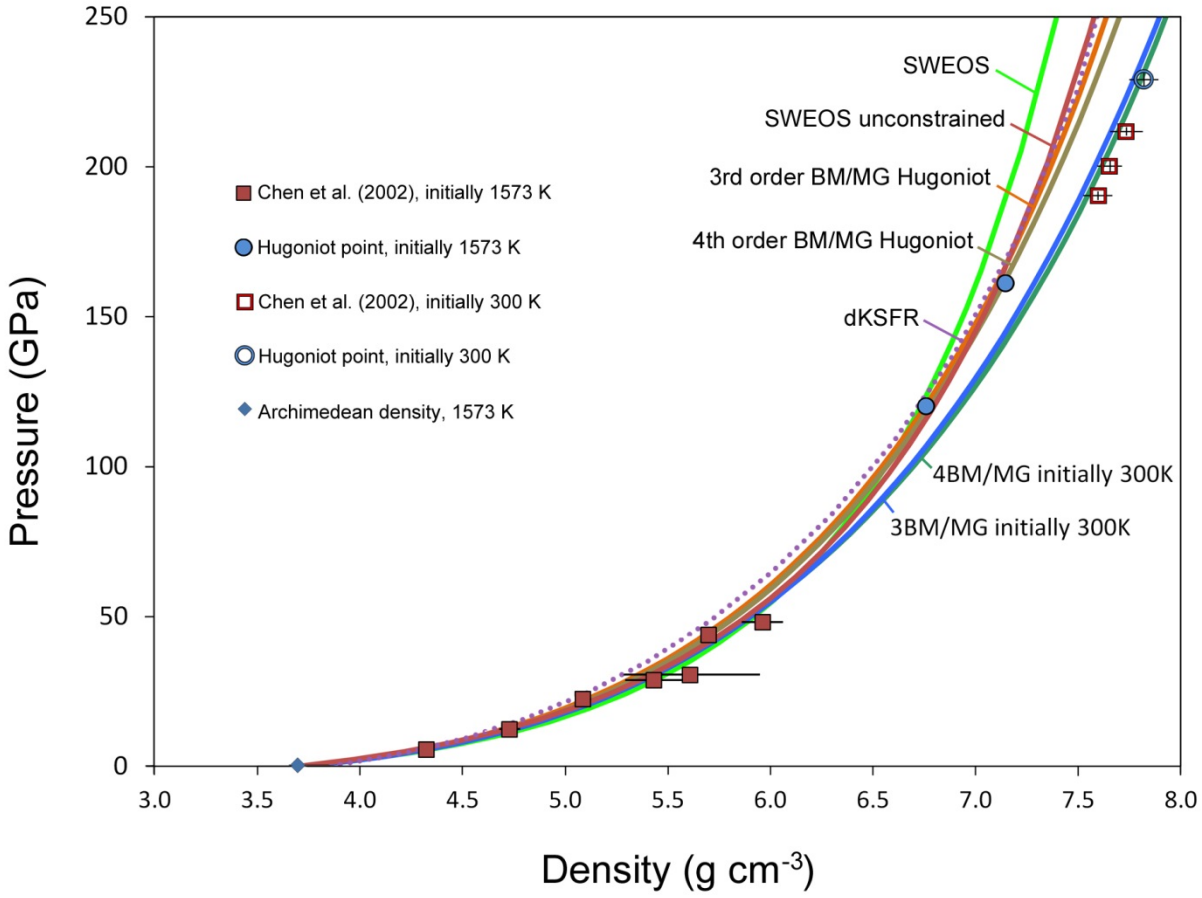
Pressure (GPa)
Density (g cm-3)
250
200
150
100
50
0
3.0
3.5
4.0
4.5
5.0
5.5
6.0
6.5
7.0
7.5
8.0
Chen et al. (2002), initially 1573 K
Hugoniot point, initially 1573 K
Chen et al. (2002), initially 300 K
Hugoniot point, initially 300 K
Archimedean density, 1573 K
SWEOS
SWEOS unconstrained
3rd order BM/MG Hugoniot
4th order BM/MG Hugoniot
dKSFR
4BM/MG initially 300K
3BM/MG initially 300K

Figure 7

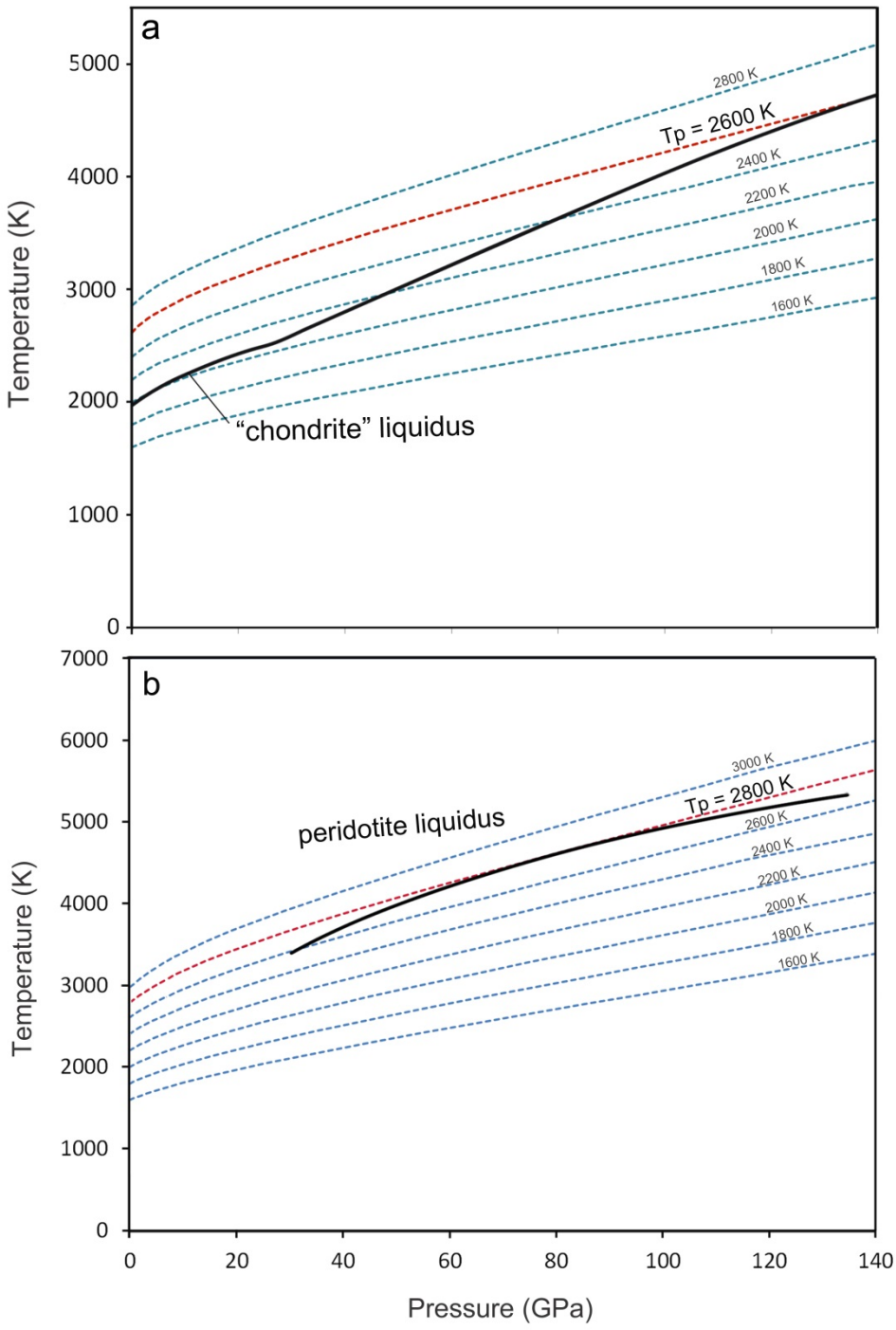
a
5000
4000
3000
2000
1000
0
Temperature (K)
2800 K
Tp = 2600 K
2400 K
2200 K
2000 K
1800 K
1600 K
"chondrite" liquidus
b
7000
6000
5000
4000
3000
2000
1000
0
Temperature (K)
3000 K
Tp = 2800 K
peridotite liquidus
2600 K
2400 K
2200 K
2000 K
1800 K
1600 K
0
20
40
60
80
100
120
140
Pressure (GPa)

Figure 8

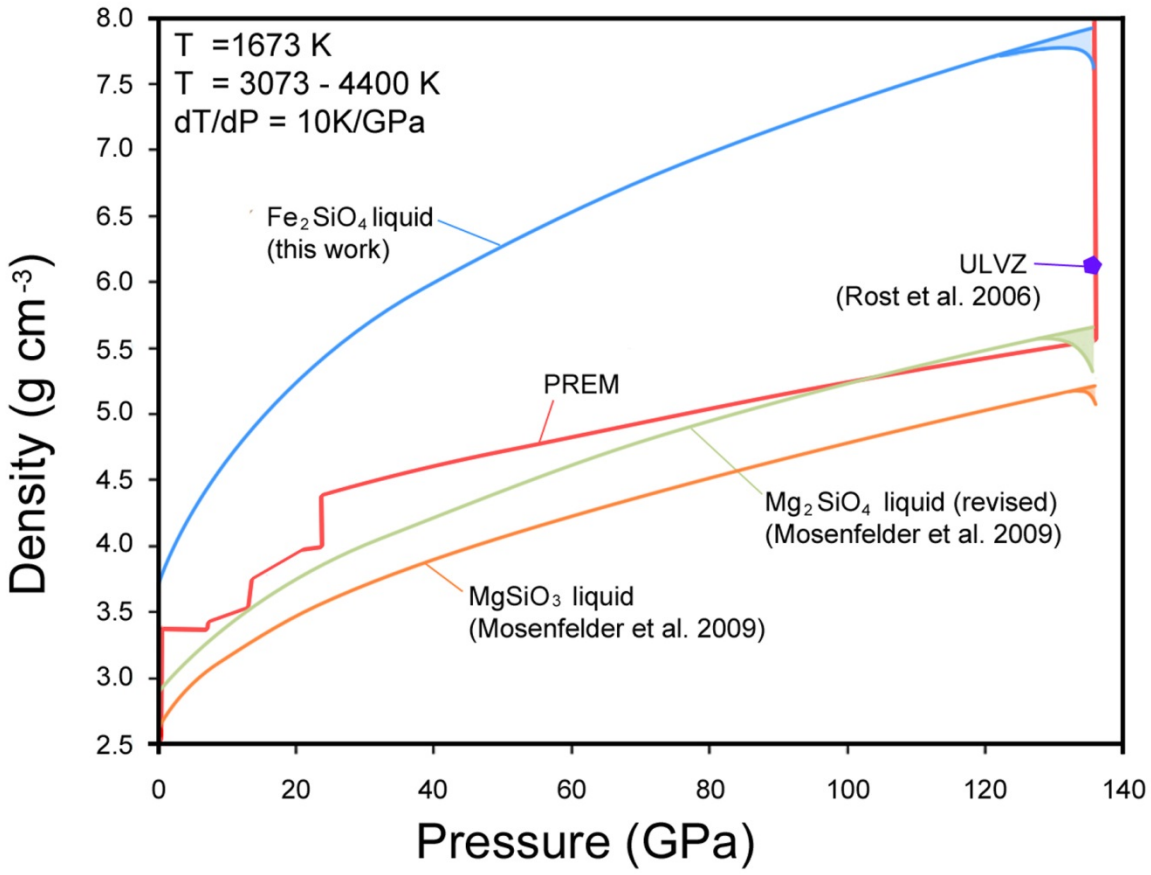
T =1673 K
T = 3073 - 4400 K
dT/dP = 10K/GPa
Fe2SiO4 liquid
(this work)
ULVZ
(Rost et al. 2006)
PREM
Mg2SiO4 liquid (revised)
(Mosenfelder et al. 2009)
MgSiO3 liquid
(Mosenfelder et al. 2009)
Density (g cm-3)
Pressure (GPa)
8.0
7.5
7.0
6.5
6.0
5.5
5.0
4.5
4.0
3.5
3.0
2.5
0
20
40
60
80
100
120
140

Figure 9

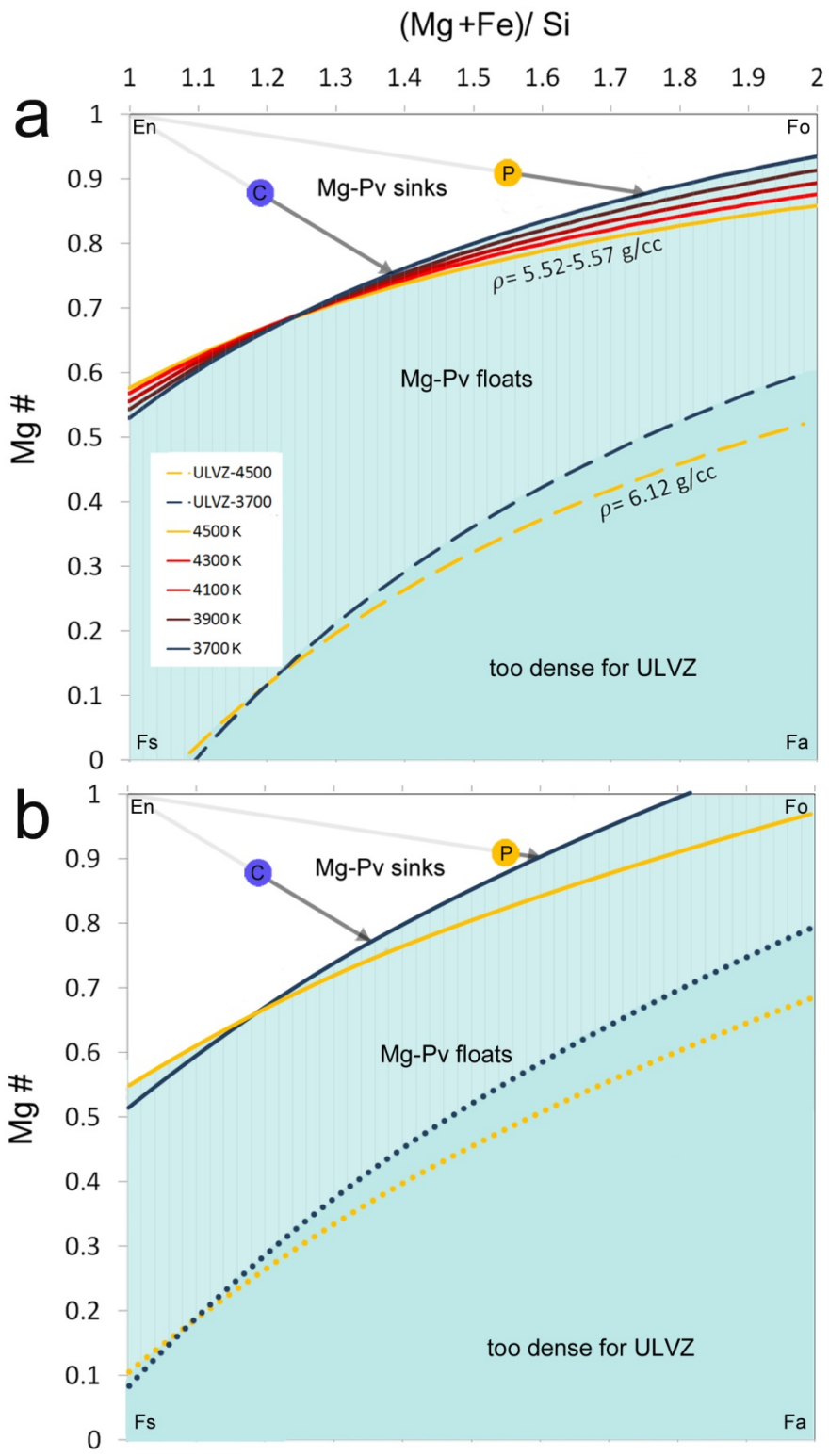
(Mg+Fe)/ Si
1
1.1
1.2
1.3
1.4
1.5
1.6
1.7
1.8
1.9
2
a
b
Mg #
0
0.1
0.2
0.3
0.4
0.5
0.6
0.7
0.8
0.9
1
En
Fo
Fs
Fa
C
P
Mg-Pv sinks
Mg-Pv floats
too dense for ULVZ
ρ= 5.52-5.57 g/cc
ρ= 6.12 g/cc
ULVZ-4500
ULVZ-3700
4500 K
4300 K
4100 K
3900 K
3700 K

Figure 10

Chapter III

Direct shock compression experiments on pre-molten Mg_2SiO_4 and progress towards a consistent high-pressure equation of state for CaO-MgO-Al_2O_3-SiO_2-FeO liquids

Claire W. Thomas

Paul D. Asimow

For submission to

Journal of Geophysical Research

April 4, 2013

ABSTRACT

We performed shock compression experiments on preheated forsterite liquid (Mg_2SiO_4) at an initial temperature of 2273 K and have revised the equation of state (EOS) that was previously determined by shock melting of initially solid Mg_2SiO_4 (300 K). The linear Hugoniot, U_S = 2.674±0.188 + 1.64±0.06 u_p km/s, constrains the bulk sound speed within a temperature and composition space as yet unexplored by 1-bar ultrasonic experiments. We have also revised the EOS for enstatite liquid ($MgSiO_3$) to exclude experiments that may have been only partially melted upon shock compression and also the EOS for anorthite liquid, which now excludes potentially unrelaxed experiments at low pressure. The revised fits and the previously determined EOS of fayalite and diopside were used to produce isentropes in the multicomponent CaO-MgO-Al_2O_3-SiO_2-FeO system at elevated temperatures and pressures. Our results are similar to those previously presented for peridotite and simplified "chondrite" liquids such that regardless of where crystallization first occurs, the liquidus solid sinks upon formation. This process is not conducive to the formation of a basal magma ocean. We also examined the chemical and physical plausibility of the partial melt hypothesis to explain the occurrence and characteristics of ultralow velocity zones. We determined that the ambient mantle cannot produce an equilibrium partial melt and residue that is sufficiently dense to be a ULVZ mush. The partial melt would need to be segregated from its equilibrium residue and combined with a denser solid component to achieve a sufficiently large aggregate density.

INTRODUCTION

The volumetric behavior of silicate melts at high pressures and temperatures is not well constrained despite its importance for accurately modeling the formation and early evolution of the Earth. Our ability to predict the chemical and physical consequences of the Earth's differentiation, for example, after the putative moon-forming impact, depends on a formulation of a liquid equation of state (EOS) accurate enough to determine the buoyancy of liquids relative to coexisting solids. Furthermore, the liquid EOS is also needed for rigorous interpretation of present-day deep Earth seismic observations: detection of ultra-low velocity zones (ULVZ) [*Garnero and Helmberger*, 1995] at the base of the mantle have been interpreted to possibly indicate the presence of liquid—potentially a partial melt [*Lay et al.*, 2004; *Williams et al.*, 1998] or a dense liquid that has remained un-sampled at the core-mantle boundary since differentiation of the planet [*Labrosse et al.*, 2007]. This latter idea is based in part on the simplified modeling of the mantle as an isochemical $MgSiO_3$ system [*Mosenfelder et al.*, 2009], which would begin crystallization in the mid-mantle for a full mantle magma ocean. This concept provides the potential for creating two separately evolving chemical reservoirs in the upper and lower mantle that would allow distillation of a presumed dense melt. Yet applying this same idea to slightly more complex multicomponent mantle compositions in the CaO-MgO-Al_2O_3-SiO_2-FeO (CMASF) system demonstrates that mid-mantle crystallization is not very likely or at least unlikely to lead to dynamically separate reservoirs [*Thomas et al.*, 2012]. Similarly, our current knowledge of the density differences between complex multicomponent silicate liquids and the present-day ambient mantle are not adequate to make precise predictions of the gravitational stability of a liquid-mush ULVZ.

Most of our understanding on the volume and elastic behavior of silicate liquids has been limited to pressures and temperatures within the upper mantle. Data are derived by density and sound speed measurements at 1 bar [*Ai and Lange*, 2008; *Ghiorso and Kress*, 2004; *Lange and Carmichael*, 1990] or by sink-float experiments at higher pressures up to a few GPa [*Agee*, 1992; 1993; *Ohtani et al.*, 1995; *Suzuki et al.*, 1998]. Diamond anvil cell (DAC) experiments are conducted at temperature and pressure regimes comparable to the lower mantle, but even distinguishing whether melting has occurred remains a non-trivial exercise (techniques for detecting melt vary among laboratories and results can often differ [*Andrault et al.*, 2011; *Fiquet et al.*, 2010]) and measuring the density of silicate melts *in situ* in the DAC remains an elusive goal. Shock experiments that start at ambient conditions and produce melt upon dynamic compression have achieved pressures equivalent to those in the deep mantle but can often be difficult to interpret due to solid-solid phase transitions along the Hugoniot or challenges in deciphering how far the melt reaction has been over-stepped [*Akins*, 2003; *Akins et al.*, 2004; *Luo et al.*, 2002; *Mosenfelder et al.*, 2007; *Mosenfelder et al.*, 2009].

Recently, preheated shock techniques have achieved pressures equivalent to those in the lower mantle for fully molten anorthite (An; $CaAl_2Si_2O_8$), diopside (Di; $CaMgSi_2O_6$), An_{36}-Di_{64} eutectic [*Asimow and Ahrens*, 2010], and fayalite (Fa; Fe_2SiO_4) [*Thomas et al.*, 2012] compositions. To this shock dataset of liquids we have added a series of novel experiments, which preheat Mg_2SiO_4 (forsterite, Fo) beyond its melting point at ambient conditions to 2273 K prior to dynamic compression. These experiments compliment the shock experiments performed on initially solid forsterite and wadsleyite (300K) [*Mosenfelder et al.*, 2007], and permit re-evaluation of the previous EOS without the ambiguities of distinguishing solid-melt transformations along the Hugoniot.

These experiments are also are the first to measure thermodynamic properties of Mg_2SiO_4 melt directly. The high melting temperature of forsterite (2163±20 K; [*Bowen and Andersen*, 1914]) has made *in situ* experimental measurements of melt properties difficult for this composition. They are instead typically calculated using linear mixing of partial molar properties extrapolated from lower temperatures and higher SiO_2 compositions [*Lange*, 1997; *Lange and Carmichael*, 1990; *Lange and Navrotsky*, 1992; *Stebbins et al.*, 1984]. Our newest measurements constrain the sound speed of silicate liquid within temperature and composition space yet unexplored by ambient-pressure ultrasonic experiments [*Ai and Lange*, 2008; *Ghiorso and Kress*, 2004].

METHODS

Sample Preparation of Preheated (2273 K) Shots

The Mg_2SiO_4 used for shock wave experiments was un-doped, single crystal forsterite (Morion Co. Gems) cored and lapped into disks. The sample disks under-filled the volume of the molybdenum sample holders by 7-13% at room temperature [cf. *Thomas et al.*, 2012]. The room temperature under-filling—accounting for thermal expansion of Mo and the thermal expansion and volume of fusion of forsterite—results in a 1 – 1.5 mm-deep meniscus at the top of the heated capsule at 2273 K. This bubble is above the area imaged by the streak camera and therefore still allows observation of simple one-dimensional wave propagation. A void space is preferred to over-filling of the capsule, which can result in warping or failure of the welded cap.

The surfaces within and outside the sample well including both sides of the cap were polished to a mirror finish with 1-micron alumina grit. Smoothing all the surfaces prevents bubbles from clinging to the walls of the sample holder during heating and potentially interfering with the imaged shock wave. The caps were electron-beam welded (Electron Beam Engineering

Inc., Anaheim, CA) to the sample holder wells enclosing the sample. The details of this process are described in *Thomas et al.* [2012]; we note that forsterite, unlike fayalite, welded easily with only occasional and minor oxidation of the cap.

Before and after welding, a profile of the topography aligned to the streak camera slit was taken with a depth gauge micrometer using a 0.7 mm flat-end tip. The inner portion of the sample well was measured in 0.2 mm increments, and the final driver and welded cap (or "top hat") were measured in 0.1 mm increments. Typically the topography varied no more than ±0.008mm from flat for the inside of the sample well and ±0.015mm for the outside driver and top hat. Sample capsules were carbon coated on both sides to reduce oxidation of the reflecting molybdenum surface during heating [cf. *Asimow and Ahrens,* 2010; *Asimow et al.*, 2008] except for shots completed on the 40-mm propellant gun. Oxidation of the target was less of a problem in the 40-mm gun possibly due to better vacuum for the smaller target chamber and catch tank volume compared to that of the 90mm/25mm two-stage light-gas gun (LGG).

Experimental Setup

The pioneering work for shock studies on molten materials is *Rigden et al.* [1984]. The description of our methods below builds on this and the work of *Rigden et al.* [1988; 1989], *Miller et al.* [1988; 1991a], *Chen and Ahrens* [1998], and *Chen et al.* [2002]. For more recent changes in experimental techniques and data analysis, the reader is directed to *Asimow et al.* [2008], *Asimow and Ahrens* [2010], and *Thomas et al.* [2012].

For this study, six total experiments were performed — four in the Caltech 90/25-mm two-stage LGG and two using the Caltech 40-mm propellant gun. All shots were preheated to 2000°C (2273 K) using a H_2O-cooled copper induction coil powered by a 10 kW Lepel radio frequency heater [*Chen and Ahrens,* 1998]. The targets were held in place by a "guy-wire" set up and

mounted through a hole drilled in a high-temperature Zircar™ zirconia board as opposed to the alumina board used for lower-temperature experiments [cf. *Asimow and Ahrens,* 2010].The boards were also cut with a slit from the center hole through to the bottom including two separate inch-deep slits at the top (a *Y* shape) in order to relieve mechanical stresses that arose due to thermal expansion of the board while at high temperatures. Lexan projectiles with molybdenum flyer plates (see Table 1) were used in this study; flyer plate velocities (u_{fp}) ranged from 1.04 - 5.963 km s^{-1}. For the LGG shots, u_{fp} was measured redundantly by a double-flash x-ray system and a two-magnet induction detector as described in *Asimow et al.* [2008]. The u_{fp} for the 40-mm gun shot was also measured by two methods: double-exposure x-ray image and laser cutoffs. The 40-mm x-ray system utilizes a double-flash x-ray, which doubly exposes the flyer image on a single piece of film. Velocity is determined by the separation of the two flyer images — taking into account the magnification on film and the previously calibrated parallax distance — divided by the time between the two x-ray discharges [*Rigden et al.*, 1988]. The 40-mm gun was also outfitted with a new laser timing system using 3 lasers aimed across the projectile path onto small active-area photodiode detectors. The distance between the lasers was measured to within ±0.05 cm, and the time between cutoffs is recorded on a 1 GHz oscilloscope. The velocities measured by the two techniques for each gun agreed to within the stated uncertainty for all the shots, and the average of the two values was used for the u_{fp} given in Table 1.

During each experiment, the rear face of the target was illuminated by a Specialised Imaging xenon spark lamp and filmed by a Hadland Imacon 790 streak camera through a narrow (25 μm) slit focused horizontally across the center of the driver and sample cap. The image of the shockwave transit was recorded using a new Specialised Imaging 2DR digital readout system. The system collects the streak image using a 4008 x 2688 pixel CCD, which was specifically

designed to affix to the streak camera tube. The image is captured digitally, in contrast to the previous method, which relied on digital scanning of analog images captured on Polaroid film [cf. *Asimow and Ahrens*, 2010; *Thomas et al.*, 2012]. The precise measurement of the shock transit time through the sample and molybdenum cap was measured from the extinguished (or sharp intensity change in) reflected light as the shock wave reached the free surface of the driver plate followed by the sample cap. The procedure for picking cutoffs and the calibration of the streak rate is described in *Thomas et al.* [2012]. The selected cutoffs were co-registered with the previously measured driver topography profiles and corrected for deviations from flat.

The shape of the shock front as it enters the sample is determined by interpolating the visible driver cutoffs using a 4^{th}-order polynomial. The 95% confidence interval for the fit was used as the upper and lower bounds for the location of the shock front and was the greatest source of error in the final calculated shock state — i.e., the error bars for shock pressure (P_H), shock density (ρ_H), particle velocity (u_p), and shock wave velocity (U_s). The time that the shock wave spends in the Mo cap is estimated using the iterative method of *Rigden et al.* [1988] and subtracted from the offset in time between the two cutoffs to calculate the shock wave velocity U_s in the sample. Then u_p, P_H, and ρ_H follow from impedance matching, the Rankine-Hugoniot equations, and the following input parameters: standard Hugoniot data (ρ_o, C_o, s) for the cold metal flyer and hot Mo driver plates [*Asimow et al.*, 2008; *Chase*, 1998] (see Table 2), the initial sample density (ρ_o) [*Lange*, 1997], and an initial guess for C_o and the s parameter of Mg_2SiO_4 liquid to seed the iteration (the converged result is independent of this guess).

RESULTS

Linear Hugoniot

The shock wave data for Mg_2SiO_4 liquid are reported in Table 1, including shot number, flyer/driver material, temperature prior to firing, u_{fp}, u_p, U_S, ρ_H, and P_H.

A Hugoniot is a family of peak shock states achieved in a material by progressively stronger shocks from the same starting conditions [*Ahrens*, 1987] (in this case, liquid Mg_2SiO_4 at 2273 K and 1 bar). Empirically, the Hugoniot of a well-behaved material forms a line in U_S-u_p space, given to third order in strain by $U_S = C_o + s\,u_p$ [*Jeanloz*, 1989]. The slope (s) is related to K'_S, the pressure derivative of the isentropic bulk modulus (K_{oS}) by $s = (K'_S + 1)/4$; the intercept, C_o, is the bulk sound speed of the material at room pressure ($C_o^2 = K_{oS} / \rho_o$) [*Ruoff*, 1967].

Typically, the intercept of the un-weighted linear Hugoniot in U_S-u_p space falls within error of the 1-bar value of the sound speed measured by ultrasonic techniques indicating relaxed (as opposed to "glass-like") behavior upon compression. Currently there are no 1-bar sound speed measurements on CaO-MgO-Al_2O_3-SiO_2 (CMAS) liquids with temperatures in excess of 1727K and mole fractions of MgO greater than 0.46 (Figure 1). Sound speed values can be calculated from the models of *Ghiorso and Kress* [2004] or *Ai and Lange* [2008] assuming linear addition of oxide component C_o and dC_o/dT but must be extrapolated well beyond the composition and temperature space used in either calibration (which is not recommended by the authors). The sound speed for Mg_2SiO_4 liquid at 2773K from *Ghiorso and Kress* [2004] is 3.195 km/s and from *Ai and Lange* [2008] is 3.126 km/s.

Figure 2 shows linear fits to shock data in U_S-u_p space fixed at these 1-bar model values as well as the unconstrained fit. The unconstrained, un-weighted linear fit to all preheated Mg_2SiO_4 liquid data points yields $U_S = 2.674\pm0.188 + 1.64\pm0.06\,u_p$ km/s ($r^2 = 0.995$). The unconstrained C_o falls below the derived model values potentially indicating that the dC_o/dT value is negative for Mg_2SiO_4 liquid, contrary to the positive [*Ghiorso and Kress*, 2004] and zero [*Ai and Lange*, 2008] values given in the previous studies. This is not evidence for unrelaxed behavior in the shock compression experiments; this would be expected to yield a higher bulk

modulus than expected from relaxed ultrasonic data. Instead it is evidence that the temperature or composition dependence of those models cannot be extrapolated to the current conditions; see discussion below. Consequently, the K_{oS} of 18.56±2.61 GPa (derived from the expression $K_{oS} = \rho_o C_o^2$ and the unconstrained C_o) is lower than the bulk moduli derived from either the *Ghiorso and Kress* [2004] or the *Ai and Lange* [2008] values, 26.55 and 25.38 GPa, respectively. This K_{oS} is also much lower than the previously reported value given in shock wave studies, 41 GPa at T_o=1673K [*Mosenfelder et al.*, 2009], which was derived from the *Lange and Carmichael* [1990] data set. If corrected to an initial temperature of 2273K using dV/dT and d^2V/dPdT [*Lange and Carmichael*, 1990], K_{oS} is 27.87 GPa and still much stiffer than our newest value of 18.56 GPa. The slope of our unconstrained Hugoniot fit corresponds to a K' of 5.58±0.24, compared to that of the previous estimate of 4.73 [*Thomas et al.*, 2012].

Grüneisen parameter

The thermodynamic Grüneisen parameter (γ) is a macroscopic parameter that relates thermal pressure to the thermal energy per unit volume. The Mie-Grüneisen approximation this can be expressed as

$$\gamma = \frac{1}{\rho}\frac{\partial P_{th}}{\partial E} \quad (1)$$

where thermal pressure (P_{th}) is defined as the increase in pressure due to heating at a constant volume [*Poirier*, 2000]. The Grüneisen parameter can be directly determined by the comparison of two Hugoniots with different initial densities [e.g. *Asimow and Ahrens*, 2010; *Luo et al.*, 2002]. When compared at an equal density, a liquid obtained by shock compression of an initially solid material will have a distinct pressure and internal energy state than that obtained by direct shock compression of the liquid of the same composition. This method also applies for

other changes in the initial state of shocked samples, including differences in initial solid phase and variations in initial porosity [*Mosenfelder et al.*, 2009].

We determined the Mg_2SiO_4 liquid γ by comparison of our 2273K liquid Hugoniot with the initially solid 300K forsterite Hugoniot from *Mosenfelder et al.* [2007]. *Mosenfelder et al.* used two Mg_2SiO_4 starting compositions, polycrystalline forsterite and wadsleyite, and they asserted that the two highest pressure shots from each dataset were shock melted (shots #350 and #349 forsterite and #350 and #349 wadsleyite). However, the calculations of *de Koker et al.* [2008] indicate that shock compression of crystalline forsterite along the 300K principal Hugoniot produces incongruent melting to periclase (MgO) and a more silica rich liquid in the pressure range of 150-170 GPa; only above 170 GPa is pure Mg_2SiO_4 liquid present on the calculated Hugoniot. Correspondingly, their calculated wadsleyite Hugoniot was found to be 1000-1400 K cooler than the forsterite Hugoniot. Therefore even the highest-pressure wadsleyite datum (shot #350) is unlikely to be fully molten and does not provide a secure point for evaluation of liquid properties.

We therefore have used only the highest forsterite point (#350, 188.5 GPa) from the *Mosenfelder et al.* [2007] dataset for determination of the liquid Grüneisen parameter. For the equations and details of this calculation, the reader is directed to *Asimow and Ahrens* [2010] and *Thomas et al.* [2012]. Using the power law form for γ

$$\gamma(\rho) = \left(\frac{\rho_o}{\rho}\right)^q \tag{2}$$

and

$$\gamma_o = \frac{\alpha K_{oS}}{\rho_o C_P}, \tag{3}$$

yields a q value of –1.51 and $\gamma_o = 0.448$. This corroborates the general trend that has been observed by both calculation [*Adjaoud et al.,* 2008; *Boehler and Kennedy,* 1977; *de Koker et al.,* 2008; *Stixrude and Karki,* 2005] and experiment [*Asimow and Ahrens,* 2010; *Mosenfelder et al.,* 2009; *Thomas et al.*, 2012] that liquid γ increases upon compression, opposite to the behavior of solids. This q value is also fairly similar to the Mg_2SiO_4 fit from *Thomas et al.* [2012] (which corrected a sign error in the re-fit from *Mosenfelder et al.* [2009]), but differs greatly in the value for γ_o. The difference in these fits can been seen most clearly in Figure 3, which displays the previous γ curve (dotted) and the newest fit tied at a much lower γ_o. This offset is due to the very discrepant values for K_{oS} used in (3), 41 GPa and 18.56 GPa for the previous and current study, respectively. Our newest fit for γ is also in much closer agreement to the linear fit given in *de Koker et al.* [2008] (Figure 3) and other silicate liquid γ functions derived from shock experiments.

Thermal Equation of State Fitting

The Hugoniot reaches temperatures and energies much higher than those of geophysical interest at lower mantle pressures (even for early Earth processes). It is therefore pertinent to select and apply a thermal equation of state formalism to investigate material properties that lie off the Hugoniot. We attempt to define the entire *P-V-E* surface of Mg_2SiO_4 liquid using the shock wave equation of state (SWEOS) and the 3rd- and 4th-order Birch-Murnaghan/Mie-Grüneisen equations of state (3BM/MG and 4BM/MG). The results and uncertainties for each fit are given in Table 3, and the Hugoniots are plotted in Figure 4.

The SWEOS is defined by a linear Hugoniot in $U_S - u_p$ space, converted to P - ρ space using the first and second Rankine-Hugoniot equations [e.g., *Ahrens,* 1987]. The slope of our linear Hugoniot, $U_S = 2.674 \pm 0.188 + 1.64 \pm 0.06\ u_p$ km/s, corresponds to a K'_S value of

5.58±0.24. States that lie off the Hugoniot are found using the Mie-Grüneisen thermal pressure approximation with a temperature-independent power law expression for the thermodynamic Grüneisen parameter (2). A q value of –1.51 was independently determined in the above Section 3.2 using selected experimental results from *Mosenfelder et al.* [2007].

The 3rd- or 4th-order BM/MG EOS is defined by a 3rd- or 4th-order Birch-Murnaghan isentrope centered at 1 bar and 2273K and a Mie-Grüneisen thermal pressure approximation. The 3BM/MG and 4BM/MG EOS are global fits, which include the six newest initially molten data points (Table 1) and the initially solid shot #350 forsterite from *Mosenfelder et al.* [2007]. Including the initially solid point (#350) reduces the error bars slightly for both fits; however, excluding the point returns nearly identical EOS parameters. We estimated uncertainties in these fits using bootstrap resampling of the data set; however, with only seven data points each at a distinct pressure, rather than many random samples from a population of Hugoniot constraints, this exercise yields rather artificial results.

We applied two sets of 3rd- and 4th-order BM/MG fits at T_o= 2273 K, one where K_{oS} was fixed to 18.56 GPa (derived from the unconstrained C_o) and a second where K_{oS} was permitted to vary within the stated error of the unconstrained C_o. For the first set of fits, the 3BM/MG EOS result is K_{oS}= 18.56 GPa, K'_S = 6.37±0.04, q = –2.16±0.14, and reduced χ^2 = 2.13. The 4BM/MG fit result is K_{oS}= 18.56 GPa, K'_S = 3.12±2.39, K_S" = 1.26±1.47 GPa^{-1}, q = 1.31±6.74 and reduced χ^2 = 1.18. The 4BM/MG evidently has very large error bars and strong correlations among the output parameters indicating a very unstable fitting routine. The 3BM/MG fit by contrast has less severe correlation between the parameters and appears justified by the fitting statistics.

For the second set of fits in which we allowed K_{oS} to vary, the best K_{oS} value was 16.41 GPa. This K_{oS} is the limit at which the derived C_o still yields a linear Hugoniot in U_S-u_p space.

The 3BM/MG fit with this K_{oS} value is K'_S = 7.37±0.81, q = –2.02±1.03, and reduced χ^2 = 1.65. The 4BM/MG fit is K_{oS} = 16.41 GPa, K'_S = 4.27±2.02, K_S'' = 1.31±1.83 GPa^{-1}, q = 0.47±9.86, and reduced χ^2 = 1.11. This 4BM/MG fit is also unstable with large error bars and strong correlations among the parameters, but the 3BM/MG fit is much more reasonable. This 3BM/MG fit has a smaller reduced χ^2 than the 3BM/MG fit above; hence for this dataset, we prefer the 3rd-order fit with K_{oS} = 16.41 GPa.

Revised Equations of State for $MgSiO_3$ and $CaAl_2Si_2O_8$ liquids

Enstatite, $MgSiO_3$

The isentrope of $MgSiO_3$ derived from the recommended global EOS fit to shock wave data from all initial polymorphs and porosities of $MgSiO_3$ [*Mosenfelder et al.,* 2009] displays an inflection point (concave down to concave up) in *T-P* space. Although this topology is not necessarily unphysical, it conflicts with the simple concave down behavior of isentropes derived from shocked liquids only (Fa, Di, $Di_{64}An_{36}$ and Fo). It is possible that the volume decreases along the Hugoniot documented for the $MgSiO_3$ shock wave data [*Mosenfelder et al.,* 2009] may indicate that the sample is only partially molten as opposed to fully molten upon shock. Such an explanation would be consistent with the interpretation of discrepancies between shock data and MD simulations noted above for some Mg_2SiO_4 experiments [*de Koker et al.,* 2008]. However, this idea is contrary to the previous assumption that silicate minerals require such large over-stepping of the liquidus that partial melting does not occur [*Akins et al.*, 2004].

To test whether the enstatite global fit may include non-liquid data, we exclude all but six of the highest pressure points from the glass [*Mosenfelder et al.*, 2009], enstatite crystal [*Akins et al.*, 2004], oxide mix [*Marsh*, 1980], and porous [*Simakov and Trunin*, 1973] data sets. These

points are the most likely to be unambiguously molten during passage of the shock wave. The hollow points in Figure 5 shows the data used in this fit.

The resulting 4BM/MG fit yields K_{oS}= 24.66 GPa, K'_S = 10.06±0.95, K_S" = 2.34±0.82 GPa^{-1}, q= –0.88±0.68, and reduced χ^2= 1.72 at T_o = 1673.15 K. Due to the low number of points being fit, the bootstrap trial values for the output parameters for K' and q were highly correlated and were in two very distinct parameter populations — one with reasonable $q \leq 1$, and another with very high K' (~14) and unreasonably high q values (40-90). This higher set is disregarded when determining the error bars on q. This fit has a similar reduced χ^2 value to the fit given in *Mosenfelder et al.* [2009] (χ^2 = 1.89) but overall displays a simple concave down isentrope in T-P space. Although not conclusive, this result may indicate that the inflection point on the model isentrope in dT/dP space was an artifact of fitting both molten and non-molten data as opposed to showing a unique physical behavior of enstatite liquid. Therefore this result also demonstrates that the technique of detecting shock melting via significant (~3%) volume [*Akins et al.*, 2004] and temperature drops [*Luo et al.*, 2004] may not be as straightforward as previously assumed and may only indicate partial melting of silicate samples.

Anorthite, $CaAl_2Si_2O_8$

In *Thomas et al.* [2012], the anorthite and diopside liquid data of *Asimow and Ahrens* [2010] were re-analyzed only sampling the center 3 mm of the arrival top hat (see Table 1). This re-sampling was motivated by a hydro-code model of shock propagation through the capsule geometry that indicated that the outer part of the top hat arrival was influenced by edge effects. The Di EOS and the An EOS parameters were both adjusted, but only the An fit displayed an inflection point for the isentrope in T-P space. As discussed in the $MgSiO_3$ section above, it is

believed this topology is more likely an artifact of fitting non-similar experimental states as opposed to representing the actual isentropic behavior of the liquid.

The anorthite liquid Hugoniot is composed of two separate experimental data sets—one at low pressure (< 36 GPa) [*Rigden et al.*, 1989] and one at high pressure (< 126 GPa) [*Asimow and Ahrens*, 2010]. The *Rigden et al.* [1989] experiments were re-analyzed in *Asimow and Ahrens* [2010], but the C_o derived from this Hugoniot in U_S-u_p space still did not fall within error of the C_o determined in 1-bar ultrasonic measurements [*Lange and Carmichael*, 1990]. In fact, anorthite liquid is the only composition studied thus far by preheated shock wave experiments (for which an ultrasonic velocity is available at similar temperature) that displays un-relaxed behavior. In the original *Rigden et al.* study, the data was fit with two separate Hugoniots due to a sharp offset observed in U_S-u_p space for the two highest pressure points. These same data points within the 25-36 GPa range have since been interpreted to be un-relaxed during compression [*Asimow and Ahrens*, 2010; *de Koker*, 2010; *Ghiorso et al.*, 2009] despite being in the middle of the full pressure range now studied. Yet excluding these points alone does not resolve the discrepant behavior obtained by simultaneously fitting the lowest pressure points of *Ridgen et al.*, the high pressure data of *Asimow and Ahrens*, and the 1 bar bulk sound speed [*Lange and Carmichael*, 1990].

One potential reason for this discrepancy is that the two shock data sets should not actually lie on the same Hugoniot, meaning the difference in the initial temperatures for two sets of experiments may be greater than stated. The *Asimow and Ahrens* experiments were heated to initially 1932 K and measured using a pyrometer; the *Ridgen et al*. experiments ranged from 1902 K to 1919 K and were measured using a thermocouple (actual experimental temperatures of *Ridgen et al.* are published in *Asimow and Ahrens* [2010]). Typically a 30 K temperature

difference should not be significant for fitting the Hugoniot, but perhaps temperature errors using the thermocouple are larger than expected with consequently some of the experiments being conducted at significantly cooler conditions.

Other possibilities include the experiments not being held at a high enough temperature above the melting point (1826 K) or held long enough above the liquidus before firing. Finally, it is also possible that there are no experimental discrepancies but that the volumetric and elastic behavior of anorthite at low pressure may be difficult to probe due to its highly polymerized structure. The rise time for the shock may be comparable to the relaxation time at least until much stronger shocks and higher temperature conditions along the Hugoniot are achieved.

Although several plausible explanations can be put forward for the seemingly unusual character of the *Ridgen et al.* anorthite data, preliminary shock results on mixed liquids with high mole fractions of anorthite component ($An_{50}Hd_{50}$ and $An_{33}Hd_{33}Di_{33}$) (see Chapter IV), in contrast, display predictable, relaxed behavior upon compression. Although it does not provide conclusive evidence, this newest data does support the likelihood of experimental differences between the two studies as opposed to unique low-pressure behavior for anorthite liquid.

In summary, although we lack a definite understanding of the source of the low-pressure anorthite anomaly, we proceed here to derive a new fit for anorthite that can be used in conjunction with other compositions to synthesize the overall behavior of silicate liquids over a broad composition range. This is obtained from *Ridgen et al.* shot 665, the re-analyzed *Asimow and Ahrens* [2010] points [*Thomas et al.*, 2012] and the experimental 1-bar sound speed at 1932 K [*Ai and Lange*, 2008]. The parameters are for the 4BM/MG fit are K_{oS} = 19.77 GPa, K'_S = 3.72±2.14, K_S" = 0 .37±2.21 GPa^{-1}, q = –1.86±1.14, and reduced χ^2= 3.09 at T_o = 1932 K. This fit displays the same two highly correlated output parameter populations due to the low number

of points included in the fitting as seen in the $MgSiO_3$ fitting in the section above. The errors are determined using only the population of bootstrap trials with $q \leq 1$. The errors for this fit are still unavoidably large, but the fit recovers the data well and also displays a concave down isentrope in *T*-*P* space.

DISCUSSION

Sound Speed of Mg_2SiO_4 liquid

Although our derived C_o is not within the error of the 1-bar models, it is unlikely that our liquid is un-relaxed or crystallized upon compression especially at the lowest experimental pressure (9.1 GPa, see Table 1). First, it would be typical for glass-like behavior to display bulk moduli higher than the ultrasonic values [*Rivers and Carmichael*, 1987]. Although the model values are extrapolated beyond their parameter space, it is at least encouraging to observe that the liquid does not have stiffer behavior than expected from these models. Second, it has been demonstrated that crystallization during the time of the experiment is improbable since the rise time of the shock wave in the sample is much less than the time necessary for crystallization to occur [*Rigden et al.*, 1988]. Rise time (τ_r) can be estimated from

$$\tau_r = \frac{u_P \eta}{U_S \Delta P_{max}} \quad (4)$$

[*Jeanloz and Ahrens*, 1979], where η is the effective viscosity and ΔP_{max} is the maximum pressure offset between the equilibrium Hugoniot and the Rayleigh line at $P_H(U_s, u_p)$. Although η is not well constrained, the experimental 1-bar viscosity at ~2000°C for near Mg_2SiO_4 liquid composition (65.1 mol% MgO) is less than 0.1 Pa s [*Urbain et al.*, 1982]. Using conservative estimates of 0.1-3 Pa s for the change in viscosity with elevated temperature and pressure [*Adjaoud et al.*, 2008], τ_r calculated at our lowest pressure point (9.21 GPa) is on order of 10^{-10}

seconds. This rise time is more than five orders of magnitude less than the time needed for crystallization for basaltic liquids derived from the time-temperature-transformation curves given in *Uhlmann et al.* [1982] (~10^{-5} s). *Fang et al.* [1983] further show that crystallization times increase with decreased polymerization; therefore crystallization is most likely kinetically impeded on the timescales of the experimental shock in Mg_2SiO_4 liquid. Finally, the most compelling evidence that crystallization did not occur during shock compression is that the temperature-pressure path of the Hugoniot is unlikely to have crossed into the solid forsterite stability field. The Mie-Grüneisen model to estimate shock temperature (T_H) is given by

$$T_H = \frac{P_H - P_S}{\gamma C_V \rho} + T_S \quad (5)$$

where T_S and P_S are temperature and pressure along the BM isentrope, C_V is the specific heat at constant volume, and γ is the Grüneisen parameter defined as a function of volume only (1). Using the 3BM/MG EOS fit (calculated in Section 3.3), Figure 6 shows that for even the highest temperature estimates of the Mg_2SiO_4 liquidus curve [*de Koker et al.*, 2008; *Ohtani and Kumazawa*, 1981] the 2273 K Hugoniot lies within the liquid field. Consequently, we are confident that our experiments are probing relaxed liquids and that the unconstrained intercept of the linear Hugoniot of 2.674±0.188 km/s is the most accurate description of the bulk sound speed at 1 bar and 2273 K.

This result implies that the dC_o/dT for Mg_2SiO_4 is negative, i.e., sound speed decreases as temperature increases. This result is actually more in line with intuition than the previous estimates of zero [*Ai and Lange*, 2008] and positive dC_o/dT values [*Ghiorso and Kress*, 2004]. Unless there are special structural rearrangements in liquid that overcome the general tendency of materials to become more anharmonic with increasing temperature and vibrational energy, one would expect liquids to act like solids and display decreasing sounds speed as temperature

increases. Results from *de Koker et al.* [2008] also indicate a decrease in sound speed with increasing temperatures from 3000 K to 6000 K; yet extrapolation of these results to 2273 K gives a value of 3124 m/s, which does not however agree with our measured value. Preliminary modeling of this apparent complex behavior for sound speed suggests it may be due to cation coordination change and the greater degrees of structural freedom of liquids compared to solids [*Wolf et al.*, 2012].

Isentropes for full mantle magma oceans

The examination of liquidus topologies has been previously employed to describe dynamics of a solidifying magma ocean [*Andrault et al.*, 2011; *Miller et al.*, 1991b; *Mosenfelder et al.*, 2009; *Thomas et al.*, 2012]. Crystal/liquid density crossover points and isentrope-liquidus intersections are both key phenomena, and the relationship between these points is important to understand. Originally treated by *Miller et al.* [1991b], the crystallization of a chondritic (iron-depleted CI composition—see *Agee and Walker* [1988]) magma ocean was depicted as a sequence of isentropes with decreasing specific entropy (or potential temperature, T_P). The tangency of the liquid isentrope with the liquidus (maximum in S-P space) gives the pressure of first crystallization. The liquidus solid is the composition of the first forming crystal, and its density contrast with respect to the ambient liquid (whether is sinks, floats, or is neutrally buoyant) has important ramifications for understanding the first steps in the dynamic modeling of the Earth's differentiation.

The one-component liquid systems enstatite and forsterite [*Mosenfelder et al.*, 2009] have been used as compositional analogues for the mantle and exhibited deep (>80 GPa) maxima in *S-P* space. The liquidus-isentrope intersections for two multicomponent systems, KLB-1 peridotite

[*Fiquet et al.*, 2010] and synthetic chondrite [*Andrault et al.*, 2011], have also been previously examined [*Thomas et al.*, 2012]. The liquidi were taken from the above referenced studies; the details for calculating the isentropes of liquid mixtures in CaO-MgO-Al_2O_3-SiO_2-FeO composition space are given in *Thomas et al.* [2012]. Isentropes derived using the newest Mg_2SiO_4 EOS (Table 3) and other re-analyzed end-member EOS of $MgSiO_3$ and $CaAl_2Si_2O_8$ (Table 4) yield slightly different results yet similar consequences to those previously presented. The critical isentrope for simplified chondrite composition shown in Figure 7 (Ch=.62En+.24Fo+.08Fa+.04An+.02Di) has a potential temperature (T_p) of 2960 K (compared to the previous estimate of T_p =2600 K), and the intersection occurs similarly at the base of the mantle (135 GPa). The peridotite (P=.33En+.56Fo+.07Fa+.03An+.007Di) critical isentrope is T_p = 3050 K and intersects the liquidus at 105 GPa, a slightly higher temperature (T_p =2900 K) and higher pressure than previously reported (~85 GPa).

The first crystallizing phase observed on the liquidus in both experimental studies [*Andrault et al.*, 2011; *Fiquet et al.*, 2010] is Mg-perovskite ($MgSiO_3$, Pv). Using the BM3S model given in *Mosenfelder et al.* [2009] (which includes the static data of *Saxena et al.* [1999]), the density of Pv at each intersection point can be calculated to determine whether the first forming crystals would sink or float. For chondrite, the density of Pv at 135 GPa and 4690 K is 5815 kg m^{-3}, whereas chondrite liquid is 5150 kg m^{-3}. Peridotite liquid is 4874 kg m^{-3} at 105 GPa and 5035 K, but Pv is 5401 kg m^{-3}. In both cases, the liquidus solid is ~15% more dense than the liquid from which it formed and would therefore sink upon formation. This calculation can be redone to include partitioning of Fe, but current published values (D_{Fe} = 0.6 to 0.07) [*Andrault et al.*, 2012; *Nomura et al.*, 2011], which favor Fe partitioning into the liquid over high-pressure

phases, would only further increase the density difference by incorporating at least some Fe into the solid Pv to form $(Mg,Fe)SiO_3$ perovskite (MgPv).

Crystallization from the middle or base of a magma ocean has implications for potentially creating a chemically stratified early mantle [*Labrosse et al.*, 2007; *Mosenfelder et al.*, 2009] provided that the lowermost mantle were to remain molten and mechanically separated from the upper mantle [*Abe*, 1997; *Tonks and Melosh*, 1993]. It has been postulated that a dense liquid at the core-mantle boundary (CMB), isolated from convection, could serve as a location for an un-degassed, primordial reservoir, which could hold a missing budget of incompatible elements [*Labrosse et al.*, 2007; *Lee et al.*, 2010]. Yet, similar to the previous conclusion given in *Thomas et al*. [2012], because the first crystals sink upon forming, this does not support the dynamic creation of a chemically stratified mantle. This conclusion is highly dependent on the choice of composition for the early bulk mantle and the liquidus topology of that composition. As shown here, despite the simplified chondrite and peridotite liquids having very similar bulk composition, the liquidus of each composition has a different maximum in *T-P* space. This discrepancy in liquidus shape in turn gives rise to very different predictions of where crystallization would begin. It is unclear whether these very different liquidus topologies are reflective of nature or are potentially derived from the different procedures used in identifying melt in the DAC [*Andrault et al.*, 2011; *Fiquet et al.*, 2010]. Additionally, choosing a bulk earth mineralogy that was more Fe-rich than either of these compositions would result in a smaller density difference with respect to the liquid and liquidus solid, but such a composition would need to be justified theoretically with respect to the timing and sequestration of the core.

Evaluating the Partial Melt Hypothesis for Ultralow Velocity Zones

Ultra low velocity zones (ULVZs) occur in thin (5-40 km) patches above the core-mantle boundary (CMB) [*Garnero and Helmberger,* 1995]. They are distinguished by several key features, the first being that they are best fit with a 3:1 ratio of S-wave to P-wave velocity anomaly, which has been inferred to indicate of the presence of liquid [*Williams and Garnero,* 1996]. They are also discontinuous along the CMB and can be often associated with the edges of large low shear velocity provinces and the source areas of plumes and large igneous provinces [*McNamara et al.*, 2010; *Rost et al.*, 2005; *Williams et al.*, 1998]. They exhibit a non-zero shear wave velocity, so the assumed liquid cannot be present as a pure melt but must be within a liquid-solid "mush." Modeling of different melt structures for this mush permits melt fractions of 0.01 % to 30% [*Williams and Garnero,* 1996], although more than 20% could lead to the loss of structural integrity for some melt configurations [*Hernlund and Jellinek,* 2010]. At select locations where reflection coefficients have been constrained, the ULVZ is inferred to be 6-14% denser than the overlying mantle, and there is an increase in S-wave velocity with depth within the ULVZ itself [*Rost et al.*, 2006].

In order for a molten silicate liquid to comprise some portion of a ULVZ, it must be denser than or at least neutrally buoyant compared to the ambient lower-most mantle; otherwise the liquid would percolate upwards away from the CMB over geologic time. The question is whether such a melt can exist. The presence of liquid in ULVZ's as a partial melt was first inferred by *Williams and Garnero* [1996] with the assumption that the density contrast between the liquid and solid would be relatively small (~1%) so that the variations in inferred seismic velocities would be small. This idea of low density contrast is based on shock-loading experiments [*Brown et al.*, 1987; *Rigden et al.*, 1984], which showed liquid densities overtaking

their equivalent solids at moderate pressures (6-10 GPa for basaltic liquid). Figure 8 shows the densities of silicate liquids Fa, En, and Fo with major mantle solids, including periclase (Pe) and Pv, along a modern mantle adiabat (10 K/ GPa) with a T_P of 1673K. This figure indicates that the assumption of density crossovers is highly dependent on chemistry as $MgSiO_3$ liquid remains less dense than MgPv at all pressures. The density curve for each liquid in Figure 8 is shown at the base of the mantle with a range of uncertainty accounting for thermal expansion across a boundary layer for CMB temperatures of 3073-4400 K. Notably, the liquid compositions have a greater sensitivity to temperature than the solids, which is in accord with their large γ and C_V values ($\alpha = \gamma\rho C_V/K_T$). It is easy to imagine that a simple mixture of any of the liquids could produce a density comparable to that of a ULVZ. In fact Mg_2SiO_4 liquid without the additional Fe at 3073K is 10% denser than PREM [*Dziewonski and Anderson*, 1981], but the important questions are whether a chosen liquid mixture is probable both 1) chemically based on our current knowledge of lower mantle chemistry and temperatures and 2) physically based on a plausible process by which it could be produced.

There are two proposed processes for creating the putative ULVZ melt. The first is a melt left over from the differentiation of the Earth, perhaps distilled from the chemistry of the lower mantle, having been segregated from the surface by mid-mantle crystallization [*Labrosse et al.*, 2007]. A second method of producing the ULVZ melt is by partial melting of the ambient mantle. We discuss these each in turn.

As shown above, our current calculations appear to oppose segregation of a magma ocean into distinct reservoirs, but in fact our ability to constrain this problem so far applies only to the very initial stage of crystallization at the liquidus and is strongly dependent on the chosen composition. Development of a solid septum at later stages of magma ocean crystallization

cannot be entirely ruled out. In detail it remains difficult test the distillation hypothesis for chemical and physical plausibility. The liquid chemistry, initially or during progressive differentiation, could occupy a wide range of compositions within CMASF space. Furthermore, the model of *Hernlund and Jellinek* [2010] suggests that stirring of the ULVZ piles by viscous coupling to the overlying mantle could create a stable mush layer for all geologic time without ongoing melt production. This model is also rather insensitive to density contrast, requiring only that the liquid be at least slightly denser than coexisting solids and disregards any chemical interaction with the mantle. Hence it is difficult to bring much insight to bear on this model using new constraints on the composition-dependent equation of state of silicate melts.

Turning to the partial melting hypothesis, its plausibility has been supported by experiments showing that magnesiowüstite and perovskite assemblages melt at temperatures comparable to estimates for the CMB — e.g., $(Mg_{0.9},Fe_{0.1})_2SiO_4$ has a solidus temperature of 4300±270 K at 130±3 GPa [*Holland and Ahrens*, 1997]. Yet presently the melting temperatures for both Mg-Pv [*Sweeney and Heinz*, 1998; *Zerr and Boehler*, 1993] and MgO [*Asimow and Fat'yanov*, 2011] remain controversial, and the effect of Fe on the melting curve remains poorly constrained. Here, we limit our discussion to the plausibility of generating a stable ULVZ via partial melting of the ambient mantle. We will construct a model of phase and bulk densities under conditions of chemical equilibrium, which searches for an initial bulk mantle composition that would yield an equilibrium assemblage of 30% volume fraction of melt and 70% volume fraction residue that could form a gravitationally stable liquid mush (i.e., melt ≤ 1% denser than residue) with bulk density 10±4% denser than PREM (~ 6123±223 kg/m^3).

To calculate the densities of the mantle solids, (Mg, Fe)SiO_3 perovskite (MgPv) and (Mg,Fe)O ferropericlase (Fp), we used the EOS provided in *Mosenfelder et al.*[2009] for pure

Mg-Pv and pure Mg-Pe and calculated the addition of small amount of Fe^{2+} by ignoring changes in molar volume upon substitution. This is certainly an oversimplification but has already been shown to be a good approximation for estimating densities of (Mg, Fe)O solid solutions (for Fe contents up to ~60 mol%) at pressures greater than 70 GPa where Fe^{2+} is in the low-spin state and has an effective ionic radius similar to Mg^{2+} (~0.72 Å) [*Fei et al.*, 2007]. Given the low Fe contents expected in Pv solid solutions in equilibrium with melt and the substantial uncertainty that remains in the liquid EOS, this is an adequate approximation for assessment of relative melt/solid buoyancy. For calculation of liquid densities, we assume linear mixing of the oxide volumes derived from the BM/MG EOS given in Tables 3 and 4.

To define the distribution of Fe and Mg at chemical equilibrium among melt, Fp, and MgPv we need to define two partition coefficients, for example a solid-solid partition coefficient $D_{Fe}^{MgPv/Fp} = X_{Fe}^{MgPv}/X_{Fe}^{Fp}$ (where X_{Fe} is molar iron content of the phase) and one solid-melt partition coefficient $D_{Fe}^{MgPv/melt} = X_{Fe}^{MgPv}/X_{Fe}^{melt}$. The solid-solid $D_{Fe}^{MgPv/Fp}$ can be as low 0.09 [*Auzende et al.*, 2008] in Al-free systems but approaches unity for Al-bearing systems at high pressure [*Wood and Rubie*, 1996]. A similar range of experimental values exists for the solid-melt $D_{Fe}^{MgPv/melt}$ for non-Al bearing [*Nomura et al.*, 2011] (~0.07) and Al-bearing systems [*Andrault et al.*, 2012] (~0.47-0.6). We have chosen to use the values derived from high pressure Al-bearing experiments as they are likely a closer approximation to natural systems. Hence for our calculations, we assumed $D_{Fe}^{MgPv/Fp}$= 1and $D_{Fe}^{MgPv/melt}$ = 0.47 (we also explore the sensitivity of our result to this choice of solid-melt partition coefficient for Fe).

In our calculations, we also fix the SiO_2 concentration of the MgPv-Fp eutectic liquid. We chose two compositions: 1) a eutectic liquid with an SiO_2 concentration of 41 mol % such that 70% of the melt is MgPv composition (f_{pvE} = 0.7) and 30% is Fp composition and 2) a liquid

with 47 mol% SiO_2 concentration (f_{pvE} = 0.9). These two estimates bracket the eutectic composition determined by *Liebske and Frost* [2012] for the pure MgO-$MgSiO_3$ system such that SiO_2 is 44 mol % (f_{pvE} = 0.8).

Ambient mantle is often approximated as 80% (Mg, Fe)SiO_3 and 20% (Mg, Fe)O with some proportion of Fe [*Boehler*, 2000]. For our model, we evaluate whether this composition as well as other more exotic compositions would be able to produce a partial melt and an equilibrium residue with a low density contrast (a melt 1% denser than the residue, equivalent to the assumption in *Williams and Garnero* [1996]) and also produce an aggregate density comparable to a ULVZ allowing 30% volume fraction of melt.

Results for this calculation at 3700 K and 135 GPa for f_{pvE} =0.7 are given in Figure 9a. The solid lines represent curves of constant density contrast for the melt and residue, where positive percentages are a partial melt denser than the residue and negative percentages are a residue denser than the melt .The ULVZ density region is delineated by dotted lines representing a density 6-14% denser than PREM (~6123±223 kg/m^3). An estimate for ambient mantle composition of 80% MgPv +20% Fp (f_{pv} =0.8) with a Mg# of 0.85 (Mg# = $X_{Mg}/(X_{Fe}+X_{Mg})$) would produce a partial melt 5% denser than its equilibrium residue, but the aggregate density would be 5503 kg/m^3, which is actually 1% less dense than PREM. To produce an aggregate density comparable to PREM, the ULVZ bulk composition would need a very high Fe concentration (Mg# $\leq$ 0.6), but this would yield a very large (at least 14%) melt-residue density contrast. In fact for a eutectic composition of f_{pvE} =0.7 and the selected partition coefficients, there is no starting composition that can fulfill both the aggregate density and density-contrast constraints. The unphysical region on the graph represents aggregate densities that are unachievable with the given amount of Fe in the system (Mg# for the partial melt is negative

within this space). If we allow $D_{Fe}^{MgPv/melt}$ to approach unity (higher than the current experimentally determined values), thereby decreasing the extent to which Fe favors the melt and also thereby decreasing the density contrast between melt and residue, the unphysical region expands and does not permit aggregate densities within the ULVZ region. This result is also insensitive to percent of partial melting, as decreased volume fraction of melt also allows for a diminished melt-residue density contrast, but likewise further limits the highest aggregate densities that are achievable. It is an important conclusion therefore that if the eutectic composition is f_{pvE}=0.7, then there is no composition in the ternary MgO-FeO-SiO_2 system (that is, any combination of Mg# or fraction of MgPv or Fp), regardless of $D_{Fe}^{MgPv/melt}$ or melt fraction, that will produce an equilibrium assemblage equivalent to what is believed to be present in a ULVZ. In fact, this is also true for eutectic compositions f_{pvE} = 0.8 [*Liebske and Frost*, 2012] and f_{pvE} =0.9 with any experimentally determined $D_{Fe}^{MgPv/melt}$ value [*Andrault et al.*, 2011]. Only at $D_{Fe}^{MgPv/melt}$ = 0.8 and a eutectic liquid of f_{pvE} = 0.9 is the minimum estimate of the aggregate density achievable with a melt 1% denser than its residue (Figure 9b). The initial composition would also need to be exotic compared to typical ambient mantle compositions: richer in Fp (f_{pv} = 0.2 -0.5) and Fe (Mg# = 0.6-0.7).

Even disregarding the lack of experimental evidence for such high D_{Fe} or MgPv rich eutectic liquids, such high Fe contents are potentially unrealistic for a wide-spread lower mantle composition. $FeSiO_3$ is unstable in the perovskite structure and decomposes to magnesiowüstite and stishovite [*Jeanloz and Thompson*, 1983] in which case the calculations of bulk densities performed here using the MgPv EOS are no longer appropriate; although the presence of aluminum has been shown to expand both ferrous [*Kesson et al.*, 1995] and ferric stability in the perovskite and post-perovskite (pPv) phases at high pressure [*Frost and McCammon*, 2008;

Frost et al., 2008; *Zhang and Oganov*, 2006].Additionally, experiments and calculations have indicated that an Fe-rich pPv phase (with Mg# ≤ 0.8) may be stable at 130 GPa [*Mao et al.*, 2006; *Mao et al.*, 2005], yet the temperature within a ULVZ remains sufficiently under-constrained that it is unclear whether Pv or pPv would be the predominate stable phase. Similarly, although despite potentially destabilizing Pv, elevated Fe contents are likely necessary to depress the melting point of Fp to reasonable CMB temperatures, considering the melting temperature of pure MgO at ambient conditions is already very high (3060 K) [*Poirier*, 2000], granting its high pressure melting curve remains uncertain. In contrast, this partial melt calculation could yield more reasonable results with less Fe in the bulk starting composition if carried out at a lower temperature (since liquids increase in density more rapidly than solids with decreasing temperature), but at some point the conditions would drop below the solidus. The correct mantle solidus temperature is not well known and better constraints on the phase diagrams of the pertinent compositions at high pressure and temperature are needed. Therefore consequently, if the model results are correct and high Fe contents are required to produce the necessary conditions for a ULVZ, partial melting may not even be necessary as suggested in *Wicks et al.* [2010], which cites the possibility of solid-state ULVZ composed of a large proportion of Fe-rich (Fe, Mg)O to produce the observed drops in S-wave velocity.

We can conclude from this exercise that the ambient mantle (80% MgPv +20% Fp) cannot produce a partial melt and equilibrium residue that could be a ULVZ mush regardless of $D_{\mathrm{Fe}}^{\mathrm{MgPv/melt}}$ or eutectic composition. There exists a starting composition which can produce a ULVZ mush with the correct aggregate density and melt-residue density contrast, but only if subject to $D_{\mathrm{Fe}}^{\mathrm{MgPv/melt}}$ and eutectic composition constraints that lie outside of what has been determined experimentally. The partial melt hypothesis is therefore only plausible if the melt is

fractionally segregated from its residue and combined with some other denser component. Only this process would permit both an aggregate density equivalent to the bulk ULVZ mush constrained by *Rost et al.* [2006] and at the same time a have a melt-residue density contrast that is consistent with assumed values used in seismic modeling (~1%) [*Williams and Garnero*, 1996], assuming both these physical constraints are robust. And although not explicitly calculated here, another potential way to increase the aggregate density would be to transform the residue to post-perovskite structure, but partitioning of Fe in pPv is not well constrained [*Kobayashi et al.*, 2005; *Sinmyo et al.*, 2011], the location of the Pv-pPv transition in Fe-bearing systems is controversial, and it would require a special scenario to place the solid Pv-pPv transition and the onset of partial melting at the same horizon.

CONCLUSIONS

We have completed new shock wave experiments on molten Mg_2SiO_4 at 2273K, a significant technical advance in initial temperature for preheated experiments of this kind, allowing study of liquid compositions and temperatures previously inaccessible to ultrasonic or other experimental methods. This new data enables a revision of the previous liquid Mg_2SiO_4 EOS [*Mosenfelder et al.*, 2009]. The Grüneisen parameter is now in better agreement with values obtained from molecular dynamics simulation [*de Koker et al.*, 2008] and is more similar to the γ behavior of other silicate liquids such as fayalite and diopside compositions. The shock-derived ambient-pressure bulk sound speed at 2273 K, compared to values estimated from lower-temperature ultrasonic data, indicates that sound speed decreases with increasing temperature for Fo liquid, contrary to the positive [*Ghiorso and Kress*, 2004] and zero [*Ai and Lange*, 2008] temperature dependences previously reported. The EOS of liquid $MgSiO_3$ and $CaAl_2Si_2O_8$ were also revised

to exclude experiments that may have only been partially melted upon shock compression and potentially un-relaxed at low pressure, respectively, resulting in EOS models of the five components Fa, Fo, En, Di, and An that all share well-behaved, concave-down isentropes in *P-T* space. These were used in an ideal mixing model to construct new isentropes for whole mantle magma oceans of selected compositions in CMASF. The results are similar to those presented previously [*Thomas et al.*, 2012], in that MgPv may begin crystallizing in the mid-lower mantle or at the base of the mantle for different compositions or estimates of their liquidus curves but in all cases MgPv is negatively buoyant at the site of initial crystallization. This does not favor the formation of a basal magma ocean at early stages of evolution. The revised EOS of $MgSiO_3$ and Mg_2SiO_4 were also used to calculate the plausibility of producing a ULVZ from a partial melt of the ambient mantle. Results indicate that any MgPv-Fp assemblage, including compositions typically assumed for the ambient mantle (80% MgPv and 20% Fp), cannot produce an equilibrium assemblage with a density comparable to that which has been inferred for a ULVZ mush. A ULVZ must be composed of fractionally segregated liquids from elsewhere in the mantle in association with a solid component denser than the equilibrium residue.

ACKNOWLEDGEMENTS

The authors would like to thank the following: the shock wave lab technical staff—Oleg Fat'yanov, Eprapodito Gelle, and Russel Oliver. This work was supported by the National Science Foundation through award EAR-1119522.

REFERENCES

Abe, Y. (1997), Thermal and chemical evolution of the terrestrial magma ocean, *Physics of The Earth and Planetary Interiors*, *100*(1-4), 27-39.

Adjaoud, O., G. Steinle-Neumann, and S. Jahn (2008), Mg_2SiO_4 liquid under high pressure from molecular dynamics, *Chemical Geology*, *256*(3-4), 185-192.

Agee, C. B. (1992), Isothermal compression of molten Fe_2SiO_4, *Geophys. Res. Lett.*, *19*(11), 1169–1172.

Agee, C. B. (1993), Olivine flotation in mantle melt, *Earth and planetary science letters*, *114*(2-3), 315.

Agee, C. B., and D. Walker (1988), Mass balance and phase density constraints on early differentiation of chondritic mantle, *Earth and Planetary Science Letters*, *90*(2), 144-156.

Ahrens, T. J. (1987), 6. Shock Wave Techniques for Geophysics and Planetary Physics, in *Methods in Experimental Physics*, edited by G. S. Charles and L. H. Thomas, pp. 185-235, Academic Press.

Ai, Y. H., and R. A. Lange (2008), New acoustic velocity measurements on CaO-MgO-Al_2O_3-SiO_2 liquids: Reevaluation of the volume and compressibility of $CaMgSi_2O_6$-$CaAl_2Si_2O_8$ liquids to 25 GPa, *J. Geophys. Res.*, *113*(B4), B04203.

Akins, J. A. (2003), Dynamic compression of minerals in the MgO-FeO-SiO_2 system, *Ph.D. thesis, Calif. Inst. of Technol., Pasadena, Calif.*

Akins, J. A., S. N. Luo, P. D. Asimow, and T. J. Ahrens (2004), Shock-induced melting of $MgSiO_3$ perovskite and implications for melts in Earth's lowermost mantle, *Geophys. Res. Lett.*, *31*(14), L14612.

Andrault, D., N. Bolfan-Casanova, G. L. Nigro, M. A. Bouhifd, G. Garbarino, and M. Mezouar (2011), Solidus and liquidus profiles of chondritic mantle: Implication for melting of the Earth across its history, *Earth and planetary science letters*, *304*(1-2), 251-259.

Andrault, D., S. Petitgirard, G. Lo Nigro, J.-L. Devidal, G. Veronesi, G. Garbarino, and M. Mezouar (2012), Solid-liquid iron partitioning in Earth's deep mantle, *Nature*, *487*(7407), 354-357.

Asimow, P. D., and T. J. Ahrens (2010), Shock compression of liquid silicates to 125 GPa: The anorthite-diopside join, *J. Geophys. Res.*, *115*(B10), B10209.

Asimow, P. D., and O. V. Fat'yanov (2011), Pre-heated MgO shock temperature experiments require a hot melting curve, *AGU Fall Meeting Abstracts*, *1*, abstract #MR33A-08 (and the references therein).

Asimow, P. D., D. Sun, and T. J. Ahrens (2008), Shock compression of preheated molybdenum to 300 GPa, *Physics of The Earth and Planetary Interiors*, *174*(1-4), 302.

Auzende, A.-L., J. Badro, F. J. Ryerson, P. K. Weber, S. J. Fallon, A. Addad, J. Siebert, and G. Fiquet (2008), Element partitioning between magnesium silicate perovskite and ferropericlase: New insights into bulk lower-mantle geochemistry, *Earth and planetary science letters*, *269*(1–2), 164-174.

Boehler, R. (2000), High-pressure experiments and the phase diagram of lower mantle and core materials, *Rev. Geophys.*, *38*(2), 221-245.

Boehler, R., and G. C. Kennedy (1977), Pressure dependence of the thermodynamical Grüneisen parameter of fluids, *Journal of Applied Physics*, *48*(10), 4183-4186.

Bowen, N. L., and O. Andersen (1914), The binary system MgO-SiO2 *Am J Sci*, *37*, 487-500.

Brown, J. M., M. D. Furnish, and R. G. McQueen (1987), Thermodynamics for (Mg, Fe) $_2SiO_4$

from the Hugoniot, in *High Pressure Research in Mineral Physics*, edited by M. Manghnani and Y. Syono, AGU, Washington, D.C.

Chase, M. W. (1998), NIST-JANAF Thermochemical Tables, *Journal of Physical and Chemical Reference Data*, *4th edition*(Monograph 9), 1–1951.

Chen, G. Q., and T. J. Ahrens (Eds.) (1998), *Radio frequency heating coils for shock wave experiments*, 63-71 pp., Materials Research Society Symposia Proceedings, Warrendale, PA.

Chen, G. Q., T. J. Ahrens, and E. M. Stolper (2002), Shock-wave equation of state of molten and solid fayalite, *Physics of The Earth and Planetary Interiors*, *134*(1-2), 35-52.

de Koker, N. (2010), Structure, thermodynamics, and diffusion in $CaAl_2Si_2O_8$ liquid from first principles molecular dynamics, *Geochimica et Cosmochimica Acta*, *74*(19), 5657-5671.

de Koker, N., L. Stixrude, and B. B. Karki (2008), Thermodynamics, structure, dynamics, and freezing of Mg_2SiO_4 liquid at high pressure, *Geochimica et Cosmochimica Acta*, *72*(5), 1427-1441.

Dziewonski, A. M., and D. L. Anderson (1981), Preliminary reference Earth model, *Physics of The Earth and Planetary Interiors*, *25*(4), 297-356.

Fang, C. Y., H. Yinnon, and D. R. Uhlmann (1983), Cooling rates for glass containing lunar compositions, *Journal of Geophysical Research: Solid Earth*, *88*(S02), A907-A911.

Fei, Y., L. Zhang, A. Corgne, H. Watson, A. Ricolleau, Y. Meng, and V. Prakapenka (2007), Spin transition and equations of state of (Mg, Fe)O solid solutions, *Geophysical research letters*, *34*(17), L17307.

Fiquet, G., A. L. Auzende, J. Siebert, A. Corgne, H. Bureau, H. Ozawa, and G. Garbarino (2010), Melting of Peridotite to 140 Gigapascals, *Science*, *329*(5998), 1516-1518.

Frost, D. J., and C. A. McCammon (2008), The redox state of Earth's mantle, *Annual Review of Earth and Planetary Sciences*, *36*, 389-420.

Frost, D. J., U. Mann, Y. Asahara, and D. C. Rubie (2008), The redox state of the mantle during and just after core formation, *Philosophical Transactions of the Royal Society A: Mathematical, Physical and Engineering Sciences*, *366*(1883), 4315-4337.

Garnero, E. J., and D. V. Helmberger (1995), A very slow basal layer underlying large-scale low-velocity anomalies in the lower mantle beneath the Pacific: evidence from core phases, *Physics of The Earth and Planetary Interiors*, *91*(1-3), 161-176.

Ghiorso, M. S., and V. C. Kress (2004), An equation of state for silicate melts. II. Calibration of volumetric properties at 10(5) Pa, *American journal of science*, *304*(8-9), 679-751.

Ghiorso, M. S., D. Nevins, I. Cutler, and F. J. Spera (2009), Molecular dynamics studies of $CaAl_2Si_2O_8$ liquid. Part II: Equation of state and a thermodynamic model, *Geochimica et Cosmochimica Acta*, *73*(22), 6937-6951.

Hernlund, J. W., and A. M. Jellinek (2010), Dynamics and structure of a stirred partially molten ultralow-velocity zone, *Earth and planetary science letters*, *296*(1–2), 1-8.

Holland, K. G., and T. J. Ahrens (1997), Melting of $(Mg,Fe)_2SiO_4$ at the Core-Mantle Boundary of the Earth, *Science*, *275*(5306), 1623-1625.

Jeanloz, R. (1989), Shock Wave Equation of State and Finite Strain Theory, *J. Geophys. Res.*, *94*.

Jeanloz, R., and T. J. Ahrens (1979), Release adiabat measurements on minerals: The effect of viscosity, *Journal of Geophysical Research: Solid Earth*, *84*(B13), 7545-7548.

Jeanloz, R., and A. B. Thompson (1983), Phase transitions and mantle discontinuities, *Reviews of Geophysics*, *21*(1), 51-74.

Kesson, S. E., J. D. Fitz Gerald, J. M. G. Shelley, and R. L. Withers (1995), Phase relations, structure and crystal chemistry of some aluminous silicate perovskites, *Earth and planetary science letters*, *134*(1–2), 187-201.

Kobayashi, Y., T. Kondo, E. Ohtani, N. Hirao, N. Miyajima, T. Yagi, T. Nagase, and T. Kikegawa (2005), Fe-Mg partitioning between (Mg, Fe)SiO_3 post-perovskite, perovskite, and magnesiowüstite in the Earth's lower mantle, *Geophysical research letters*, *32*(19), L19301.

Labrosse, S., J. W. Hernlund, and N. Coltice (2007), A crystallizing dense magma ocean at the base of the Earth's mantle, *Nature*, *450*(7171), 866-869.

Lange, R. A. (1997), A revised model for the density and thermal expansivity of K_2O-Na_2O CaO-MgO-Al_2O_3-SiO_2 liquids from 700 to 1900 K: extension to crustal magmatic temperatures, *Contributions to Mineralogy and Petrology*, *130*(1), 1-11.

Lange, R. A., and I. S. E. Carmichael (1990), Thermodynamic properties of silicate liquids with emphasis on density, thermal expansion and compressibility, *Reviews in Mineralogy and Geochemistry*, *24*(1), 25-64.

Lange, R. A., and A. Navrotsky (1992), Heat capacities of Fe_2O_3-bearing silicate liquids, *Contributions to Mineralogy and Petrology*, *110*(2-3), 311.

Lay, T., E. J. Garnero, and Q. Williams (2004), Partial melting in a thermo-chemical boundary layer at the base of the mantle, *Physics of The Earth and Planetary Interiors*, *146*(3-4), 441-467.

Lee, C. T. A., P. Luffi, T. Hoink, J. Li, R. Dasgupta, and J. Hernlund (2010), Upside-down differentiation and generation of a 'primordial' lower mantle, *Nature*, *463*(7283), 930-U102.

Liebske, C., and D. J. Frost (2012), Melting phase relations in the MgO–$MgSiO_3$ system between 16 and 26;GPa: Implications for melting in Earth's deep interior, *Earth and planetary science letters*, *345–348*(0), 159-170.

Luo, S. N., J. L. Mosenfelder, P. D. Asimow, and T. J. Ahrens (2002), Direct shock wave loading of Stishovite to 235 GPa: Implications for perovskite stability relative to an oxide assemblage at lower mantle conditions, *Geophys. Res. Lett.*, *29*(14).

Luo, S. N., J. A. Akins, T. J. Ahrens, and P. D. Asimow (2004), Shock-compressed $MgSiO_3$ glass, enstatite, olivine, and quartz: Optical emission, temperatures, and melting, *Journal of Geophysical Research: Solid Earth*, *109*(B5), B05205.

Mao, W. L., H. Mao, W. Sturhahn, J. Zhao, V. B. Prakapenka, Y. Meng, J. Shu, Y. Fei, and R. J. Hemley (2006), Iron-Rich Post-Perovskite and the Origin of Ultralow-Velocity Zones, *Science*, *312*(5773), 564-565.

Mao, W. L., Y. Meng, G. Shen, V. B. Prakapenka, A. J. Campbell, D. L. Heinz, J. Shu, R. Caracas, R. E. Cohen, Y. Fei, R. J. Hemley, H. Mao(2005), Iron-rich silicates in the Earth's D″ layer, *Proceedings of the National Academy of Sciences of the United States of America*, *102*(28), 9751-9753.

Marsh, S. P. (Ed.) (1980), *LASL Shock Hugoniot Data* 658 pp., University of California, Berkeley.

McNamara, A. K., E. J. Garnero, and S. Rost (2010), Tracking deep mantle reservoirs with ultra low velocity zones, *Earth and planetary science letters*, *299*(1-2), 1-9.

Miller, G. H., T. J. Ahrens, and E. M. Stolper (1988), The equation of state of molybdenum at 1400 C, *Journal of Applied Physics*, *63*(9), 4469-4475.

Miller, G. H., E. M. Stolper, and T. J. Ahrens (1991a), The Equation of State of a Molten

Komatiite 1 Shock Wave Compression to 36 GPa, *J. Geophys. Res.*, *96*.
Miller, G. H., E. M. Stolper, and T. J. Ahrens (1991b), The Equation of State of a Molten Komatiite 2. Application to Komatiite Petrogenesis and the Hadean Mantle, *J. Geophys. Res.*, *96*.
Mosenfelder, J. L., P. D. Asimow, and T. J. Ahrens (2007), Thermodynamic properties of Mg_2SiO_4 liquid at ultra-high pressures from shock measurements to 200 GPa on forsterite and wadsleyite, *J. Geophys. Res.*, *112*.
Mosenfelder, J. L., P. D. Asimow, D. J. Frost, D. C. Rubie, and T. J. Ahrens (2009), The $MgSiO_3$ system at high pressure: Thermodynamic properties of perovskite, postperovskite, and melt from global inversion of shock and static compression data, *J. Geophys. Res.*, *114*.
Nomura, R., H. Ozawa, S. Tateno, K. Hirose, J. Hernlund, S. Muto, H. Ishii, and N. Hiraoka (2011), Spin crossover and iron-rich silicate melt in the Earth's deep mantle, *Nature*, *473*(7346), 199-202.
Ohtani, E., and M. Kumazawa (1981), Melting of forsterite Mg_2SiO_4 up to 15 GPa, *Physics of The Earth and Planetary Interiors*, *27*(1), 32-38.
Ohtani, E., Y. Nagata, A. Suzuki, and T. Kato (1995), Melting relations of peridotite and the density crossover in planetary mantles, *Chemical Geology*, *120*(3-4), 207-221.
Poirier, J.-P. (2000), *Introduction to the Physics of the Earth's Interior*, 2nd ed., 328 pp., Cambridge University Press, New York.
Presnall, D. C., and M. J. Walter (1993), Melting of forsterite, Mg_2SiO_4, from 9.7 to 16.5 GPa, *Journal of Geophysical Research: Solid Earth*, *98*(B11), 19777-19783.
Rigden, S. M., T. J. Ahrens, and E. M. Stolper (1984), Densities of liquid silicates at high pressures, *Science*, *226*(4678), 1071-1074.
Rigden, S. M., T. J. Ahrens, and E. M. Stolper (1988), Shock compression of molten silicate: results for a model basaltic composition, *J. Geophys. Res.*, *93*(B1), 367-382.
Rigden, S. M., T. J. Ahrens, and E. M. Stolper (1989), High-Pressure Equation of State of Molten Anorthite and Diopside, *Journal of Geophysical Research*, *94*(B7), 9508-9522.
Rivers, M. L., and I. S. E. Carmichael (1987), Ultrasonic Studies of Silicate Melts, *J. Geophys. Res.*, *92*(B9), 9247-9270.
Rost, S., E. J. Garnero, and Q. Williams (2006), Fine-scale ultralow-velocity zone structure from high-frequency seismic array data, *J. Geophys. Res.*, *111*(B9), B09310.
Rost, S., E. J. Garnero, Q. Williams, and M. Manga (2005), Seismological constraints on a possible plume root at the core-mantle boundary, *Nature*, *435*(7042), 666-669.
Ruoff, A. (1967), Linear Shock-Velocity-Particle-Velocity Relationship, *Journal of Applied Physics*, *38*(13), 4976.
Saxena, S. K., L. S. Dubrovinsky, F. Tutti, and T. Le Bihan (1999), Equation of state of $MgSiO_3$ with the perovskite structure based on experimental measurement, *American Mineralogist*, *84*(3), 226-232.
Simakov, G. V., and R. F. Trunin (1973), On the existence of overdense perovskite structures in magnesium silicates under conditions of high pressure (English translation), *Izvestiya Earth Phys*, *9*, 603-604.
Sinmyo, R., K. Hirose, S. Muto, Y. Ohishi, and A. Yasuhara (2011), The valence state and partitioning of iron in the Earth's lowermost mantle, *J. Geophys. Res.*, *116*(B7), B07205.
Stebbins, J. F., I. S. E. Carmichael, and L. K. Moret (1984), Heat capacities and entropies of silicate liquids and glasses, *Contributions to Mineralogy and Petrology*, *86*(2), 131-148.
Stixrude, L., and B. Karki (2005), Structure and Freezing of $MgSiO_3$ Liquid in Earth's Lower

Mantle, *Science*, *310*(5746), 297-299.
Stixrude, L., and C. Lithgow-Bertelloni (2005), Thermodynamics of mantle minerals – I. Physical properties, *Geophysical Journal International*, *162*(2), 610-632.
Suzuki, A., E. Ohtani, and T. Kato (1998), Density and thermal expansion of a peridotite melt at high pressure, *Physics of The Earth and Planetary Interiors*, *107*(1–3), 53-61.
Sweeney, J. S., and D. L. Heinz (1998), Laser-heating through a diamond-anvil cell: Melting at high pressures, in *Properties of Earth and Planetary Materials at High Pressure and Temperature*, edited by M. H. Manghanani and T. Yagi, pp. 197-214, Geophysical Monograph-American Geophysical Union, Washington D.C.
Thomas, C. W., Q. Liu, C. B. Agee, P. D. Asimow, and R. A. Lange (2012), Multi-technique equation of state for Fe_2SiO_4 melt and the density of Fe-bearing silicate melts from 0 to 161 GPa, *J. Geophys. Res.*, *117*(B10), B10206.
Tonks, W. B., and H. J. Melosh (1993), Magma Ocean Formation Due to Giant Impacts, *J. Geophys. Res.*, *98*(E3), 5319-5333.
Uhlmann, D. R., H. Yinnon, and C.-Y. Fang (1982), Simplified model evaluation of cooling rates for glass-containing lunar compositions, *Lunar and Planetary Science Conference*, *12B*, 281-288.
Urbain, G., Y. Bottinga, and P. Richet (1982), Viscosity of liquid silica, silicates and alumino silicates, *Geochimica et Cosmochimica Acta*, *46*(6), 1061-1072.
Wicks, J. K., J. M. Jackson, and W. Sturhahn (2010), Very low sound velocities in iron-rich (Mg, Fe) O: Implications for the core-mantle boundary region, *Geophysical research letters*, *37*(15), 15304.
Williams, Q., and E. J. Garnero (1996), Seismic Evidence for Partial Melt at the Base of Earth's Mantle, *Science*, *273*(5281), 1528-1530.
Williams, Q., J. Revenaugh, and E. J. Garnero (1998), A Correlation Between Ultra-Low Basal Velocities in the Mantle and Hot Spots, *Science*, *281*(5376), 546-549.
Wolf, A. S., P. D. Asimow, and D. J. Stevenson (2012), A Simplified Cation Speciation Model for Silicate Liquids at Mantle Pressures and Temperatures, *AGU Fall Meeting Abstracts*, *1*, abstract MR43A-2300.
Wood, B. J., and D. C. Rubie (1996), The Effect of Alumina on Phase Transformations at the 660-Kilometer Discontinuity from Fe-Mg Partitioning Experiments, *Science*, *273*(5281), 1522-1524.
Zerr, A., and R. Boehler (1993), Melting of $(Mg,Fe)SiO_3$ Perovskite to 625 Kilobars: Indication of a High Melting Temperature in the Lower Mantle, *Science*, *262*(5133), 553-555.
Zhang, F. W., and A. R. Oganov (2006), Mechanisms of Al^{3+} incorporation in $MgSiO_3$ post-perovskite at high pressures, *Earth and planetary science letters*, *248*(1-2), 69-76.

Table 1. Shock compression data

Shot #	Flyer material	T (K)	u_{fp} km s^{-1}		u_p km s^{-1}		U_s km s^{-1}		ρ_H Mg m^{-3}		P_H GPa	
Forsterite												
1075 [a]	Mo	2274	2.019	0.003	1.644	0.001	5.38	0.02	3.74	0.01	22.98	0.07
1077 [a]	Mo	2273	1.04	0.02	0.886	0.004	4.00	0.11	3.34	0.03	9.21	0.2
455	Mo	2273	5.426	0.007	4.08	0.02	9.14	0.17	4.68	0.09	96.7	1.4
457	Mo	2273	3.32	0.01	2.59	0.03	7.10	0.44	4.10	0.17	47.6	2.3
458	Mo	2273	4.522	0.008	3.41	0.01	8.47	0.12	5.29	0.05	75.0	0.8
459	Mo	2273	5.964	0.002	4.43	0.02	9.95	0.17	5.42	0.08	114.3	1.5
Anorthite												
665†	Cu	1922.2	1.8	0.03	1.325	0.025	4.68	0.01	3.57	0.03	15.90	0.30
364	Mo	1930	4.997	0.005	3.816	0.003	8.49	0.04	4.64	0.02	82.80	0.28
380	Mo	1932	5.434	0.003	4.501	0.005	9.56	0.05	4.84	0.03	95.30	0.63
379	Mo	1932	6.007	0.025	4.094	0.007	9.09	0.08	4.66	0.04	110.00	0.44
382	Mo	1932	6.533	0.013	4.868	0.024	10.06	0.23	4.97	0.13	126.00	2.30
Diopside												
	Mo	1781	4.984	0.003	3.697	.008	9.33	0.10	4.34	0.03	90.84	0.72

[a] Caltech 40mm propellant gun † Anorthite and diopside shots are from *Asimow and Ahrens* [2010] revised in *Thomas et al.* [2012] but not previously published except for 665 which was revised in *Asimow and Ahrens* [2010] and originally from *Rigden et al.* [1989].

Table 2. Parameters used

		Molybdenum (2273 K)	Molybdenum (300 K)
ρ_o	Mg m^{-3}	9.785	10.21
C_o	km s^{-1}	4.858	5.033
s		1.288	1.289

Asimow et al. [2008]; *Chase* [1998]

Table 3. Equation of State fits for molten Mg_2SiO_4

	Units	SWEOS	BM3	BM4	Source
T_o	K	2273	2273	2273	
ρ_o	kg m^{-3}	2597 9 11	2597 ± 11	2597 ± 11	L97
C_o	m s^{-1}	2674 ± 19	-	-	fitted
s		1.64 ± 0.06	-	-	fitted
γ_o		0.448	0.396	0.396	derived
q		-1.51†	–2.02 ± 1.03	0.47 ± 9.86	fitted
K_{oS}	GPa	18.57	16.41*	16.41*	derived/*fitted
K_S'		5.58 ± 0.24	7.37 ± 0.81*	4.27 ± 2.02*	derived/*fitted
K_S''	GPa^{-1}	-	-	1.31 ± 1.83	fitted
χ^2		-	1.65	1.11	
K_T	GPa	16.54	14.80	14.80	derived
α	K^{-1}	1.21-04	1.21-04	1.21-04	L97
C_p	J kg^{-1}	1926.18	1926.18	1926.18	LN92
C_v	J kg^{-1}	1715.23	1737.36	1737.36	derived

SWEOS= shock wave equation of state. 3BM/MG = 3rd-order Birch-Murnaghan/Mie-Grüneisen EOS 4BM/MG = 4th-order Birch-Murnaghan/Mie-Grüneisen EOS. † derived from shot 350 Fo *Mosenfelder et al.* [2007] Sources: *Fitted* indicates an adjustable parameter, L97 is *Lange* [1997], LN92 is *Lange and Navrotsky* [1992]

Table 4. Equation of State fits for molten silicate liquids

	Units	3BM/MG Di†	3BM/MG Fa†	4BM/MG An	4BM/MG En	Source
T_o	K	1673	1573	1932	1673	
ρ_o	kg m^{-3}	2643	3699	2560	2617	L97
γ_o		0.493	0.412	0.174	0.365	derived
q		-1.28	-0.95	-1.86	-0.88	fitted
K_{oS}	GPa	24.57	21.99	19.77	24.66	derived
K_S'		6.77	7.28	3.73	10.07	fitted
K_S''	GPa^{-1}	-	-	0.38	-2.35	fitted
C_p	J kg^{-1} K^{-1}	1612.56	1182.35	1528.72	1761.15	LN92
C_v	J kg^{-1} K^{-1}	1506.21	1122.73	1511.28	1690.53	derived

3BM/MG = 3rd-order Birch-Murnaghan/Mie-Grüneisen EOS 4BM/MG = 4th-order/Birch-Murnaghan Mie-Grüneisen EOS. Sources: *Fitted* indicates an adjustable parameter, L97 is *Lange* [1997], LN92 is *Lange and Navrotsky* [1992], †Thomas et al [2012]

FIGURE CAPTIONS

Figure 1. The set of experiments used for modeling sound speeds of silicate liquids in *Ghiorso and Kress* [2004] and *Ai and Lange*[2008] compared to the initial temperature and composition of Mg_2SiO_4 liquid.

Figure 2. Preheated (2273K) forsterite Hugoniot in shock velocity (U_s)-particle velocity (u_p) space. The thick black line represents the unconstrained linear Hugoniot; the orange and blue lines are fixed at the sound speeds calculated using the models from *Ghiorso and Kress* [2004] and *Ai and Lange*[2008], respectively.

Figure 3. The behavior of Grüneisen parameter for Mg_2SiO_4 liquid (thick solid green) compared to its previously reported value (dotted) [*Mosenfelder et al.*, 2009]. The thin red and blue lines are the behavior of γ for diopside and fayalite, respectively. The EOS parameters used are given in Table 4. The squares and black line and are the results and linear fit from MD simulations of Mg_2SiO_4 liquid [*de Koker et al.*, 2008]

Figure 4. Mg_2SiO_4 liquid Hugoniot plotted in pressure-density space with thermal EOS fits. Data symbols are the same as Figure 3. Abbreviations: SWEOS- shock wave equation of state; BM/MG – Birch-Murnaghan/Mie-Grüneisen EOS

Figure 5. $MgSiO_3$ Hugoniot data used in the global fit of *Mosenfelder et al*. [2009] for $MgSiO_3$ melt. The volume for each experimental point is normalized to the volume of its starting

material. The data set includes enstatite glass [*Mosenfelder et al.*, 2009] (triangle), enstatite crystal [*Akins et al.*, 2004] (diamond), oxide mix [*Marsh*, 1980] (circle), and porous enstatite [*Simakov and Trunin*, 1973] (square). The gray line is the high pressure state assignment from *Mosenfelder et al*. [2009] to either perovskite, post-perovskite, or melt. Only the hollow points were included in our fit. Solid points within the melt field were excluded. Error bars not shown.

Figure 6. Estimates of the Mg_2SiO_4 liquidus from *de Koker et al.* [2008] (black curve with shaded gray error), *Presnall and Walter* [1993](green curve) and *Ohtani and Kumazawa* [1981] purple curve including the experimentally determinations liquid (circles) and solid (squares) quench. The estimated *T*-*P* path of the Hugoniot (dashed line) and shot #1077 (diamond) (see Table 1) lie within the liquid field.

Figure 7. Models for the early mantle upon cooling showing the comparison of the liquidus curves (black solid line) with the isentropic temperature profile (dotted line) of the same composition. (a) Simplified “chondritic” composition and liquidus from *Andrault et al.* [2011]. (b) Peridotite KLB-1 composition and liquidus from *Fiquet et al.* [2010]. The critical isentrope with its mantle potential temperature is shown in red. The tangent point of the critical isentrope and the liquidus gives the pressure and temperature at the onset of crystallization. The EOS parameters used for calculating the isentropes are given in Table 3 and 4.

Figure 8. Estimated densities for silicate liquids Fa (blue curve), Fo (green curve) and En (orange curve) and mantle solids Fo, wadsleyite (Wd), ringwoodite (Rw), periclase (Pe), Mg-perovskite (Pv), and post-perovskite (pPv) (black curves) as function of pressure along a 10K/GPa mantle

geotherm. The dashed lines are the previous density estimates for Fo liquid (green) and En liquid (orange) from EOS parameters given in *Mosenfelder* et al. [2009].The density at base of mantle (135 GPa) for each composition is thermally corrected from 3073K to 4400K (shaded cones). Also shown is the density profile from PREM [*Dziewonski and Anderson*, 1981], the inferred density for a ULVZ from seismic reflection coefficients [*Rost et al.*, 2006](square), and an estimated ambient mantle composition of 80% $(Mg_{0.85}Fe_{0.15})SiO_3$ perovskite+ 20% $(Mg_{0.85}Fe_{0.15})O$ (diamond) at 3000K and 129 GPa. The EOS parameters for the liquids are taken from Tables 3 and 4. EOS for Mg-Pv and pPv are from *Mosenfelder* et al. [2009]; other solid EOS are from *Stixrude and Lithgow-Bertelloni* [2005].

Figure 9. Results for partial melting calculation at 3700 K and 135 GPa. The solid curves represent lines of constant density contrast for the melt and residue, where positive percentages are a partial melt denser than the residue and negative percentages are a residue denser than the melt for a given starting composition. The y-axis if the fraction of MgPv in the starting material (f_{pv}) where the remainder is Fp; the x-axis is the Mg# of the starting composition, where Mg#.= $X_{Mg}/(X_{Fe}+X_{Mg})$.The density of the ULVZ is the blue region delineated by dotted lines representing a density 6-14% denser than PREM (~6123±223 kg/m^3). An estimate for ambient mantle composition of 80% MgPv +20% Fp (f_{pv} =0.8) with an Mg# of 0.85 is given with its calculated aggregate density (agg ρ) with 30% volume fraction of partial melt. The unphysical region on the graph signifies where Mg# for the partial melt is negative and hence represents aggregate densities that are unachievable with the given amount of Fe in the system) The eutectic liquid is fixed at 70% MgPv (f_{pvE} = 0.7) and the $D_{Fe}^{MgPv/melt}$ = 0.47. b) The eutectic liquid is fixed at 90% MgPv (f_{pvE} = 0.97) and the $D_{Fe}^{MgPv/melt}$ = 0.8.

FIGURES

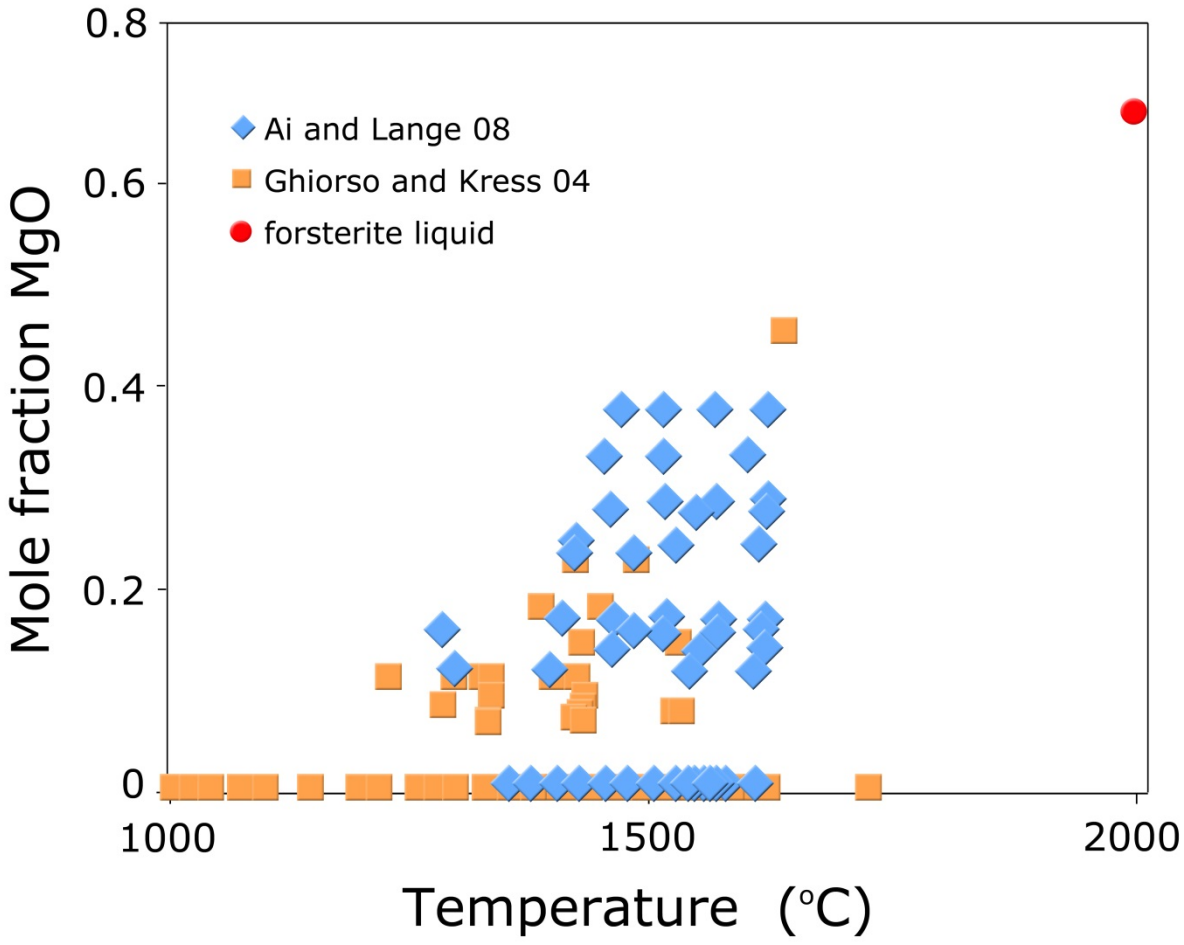

Figure 1

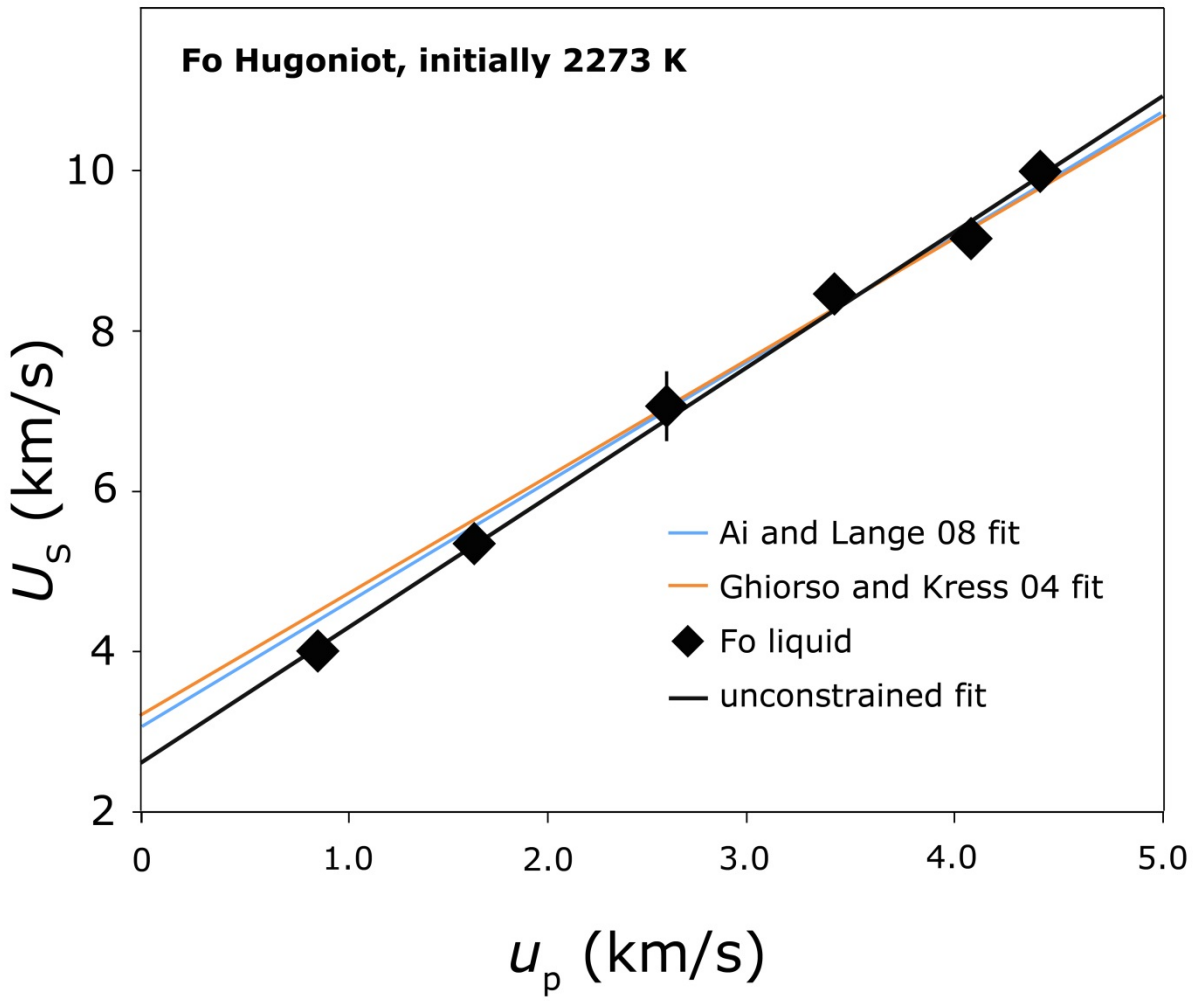
Fo Hugoniot, initially 2273 K
10
8
6
4
2
U_S (km/s)
0
1.0
2.0
3.0
4.0
5.0
u_p (km/s)
Ai and Lange 08 fit
Ghiorso and Kress 04 fit
Fo liquid
unconstrained fit

Figure 2

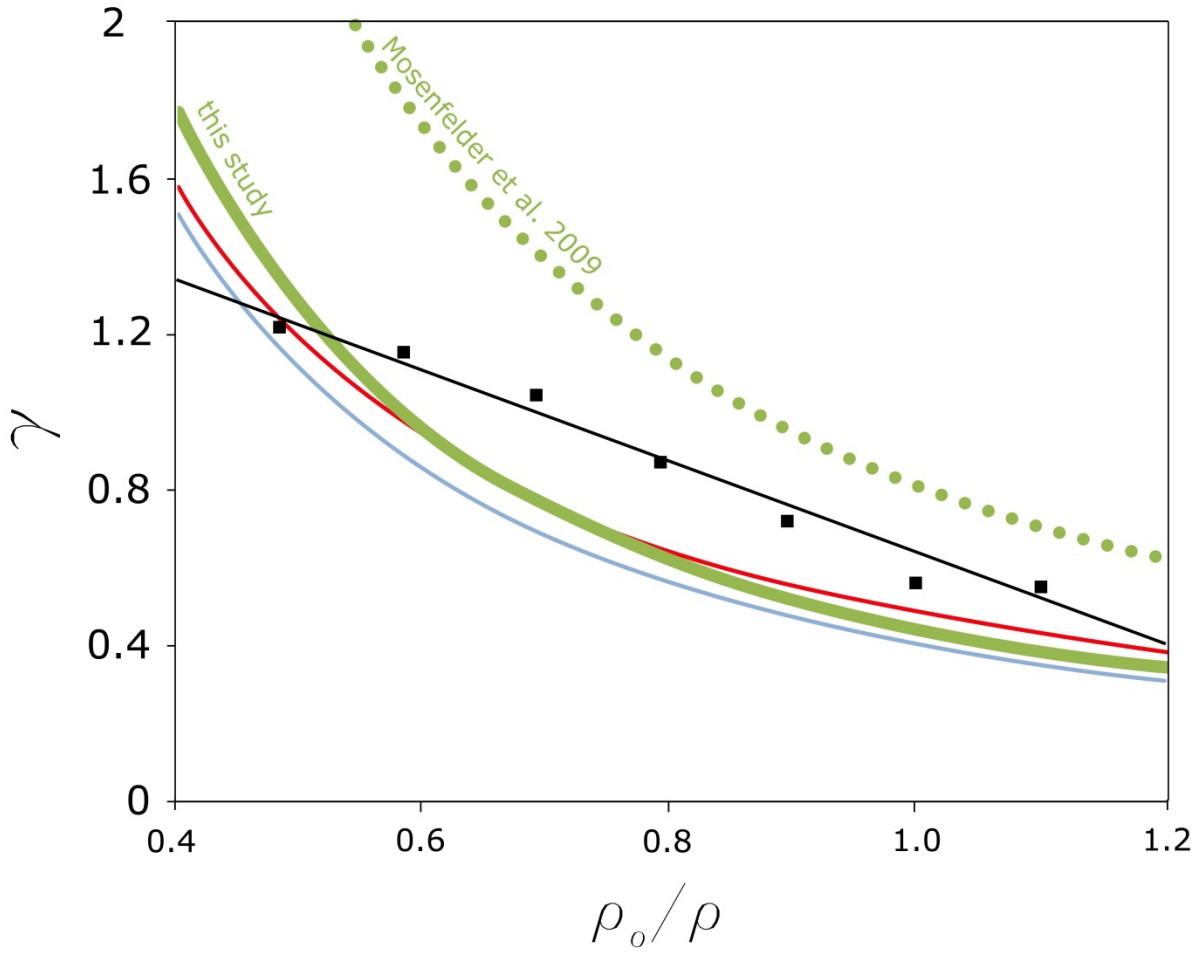
2
1.6
1.2
0.8
0.4
0
0.4
0.6
0.8
1.0
1.2
γ
ρ_o/ρ
this study
Mosenfelder et al. 2009

Figure 3

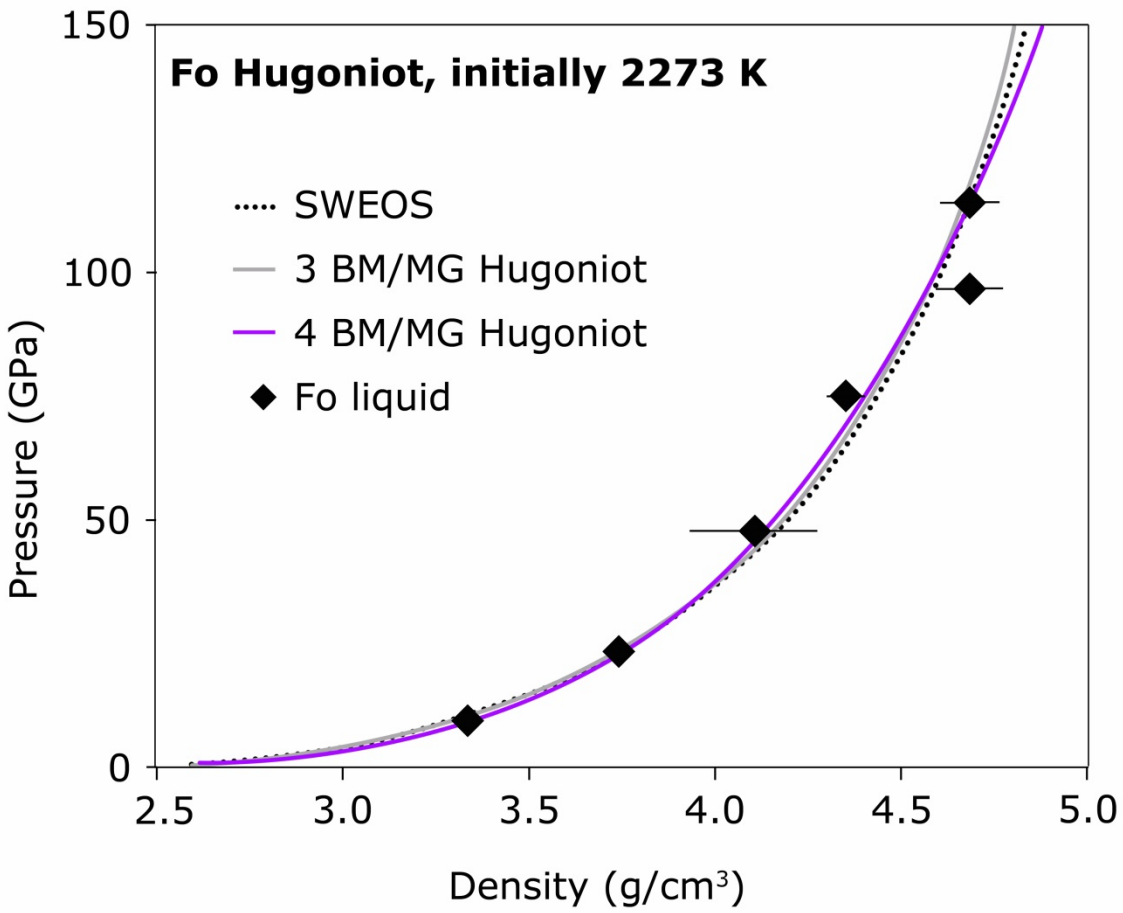
Fo Hugoniot, initially 2273 K
SWEOS
3 BM/MG Hugoniot
4 BM/MG Hugoniot
Fo liquid
Pressure (GPa)
Density (g/cm³)
150
100
50
0
2.5
3.0
3.5
4.0
4.5
5.0

Figure 4

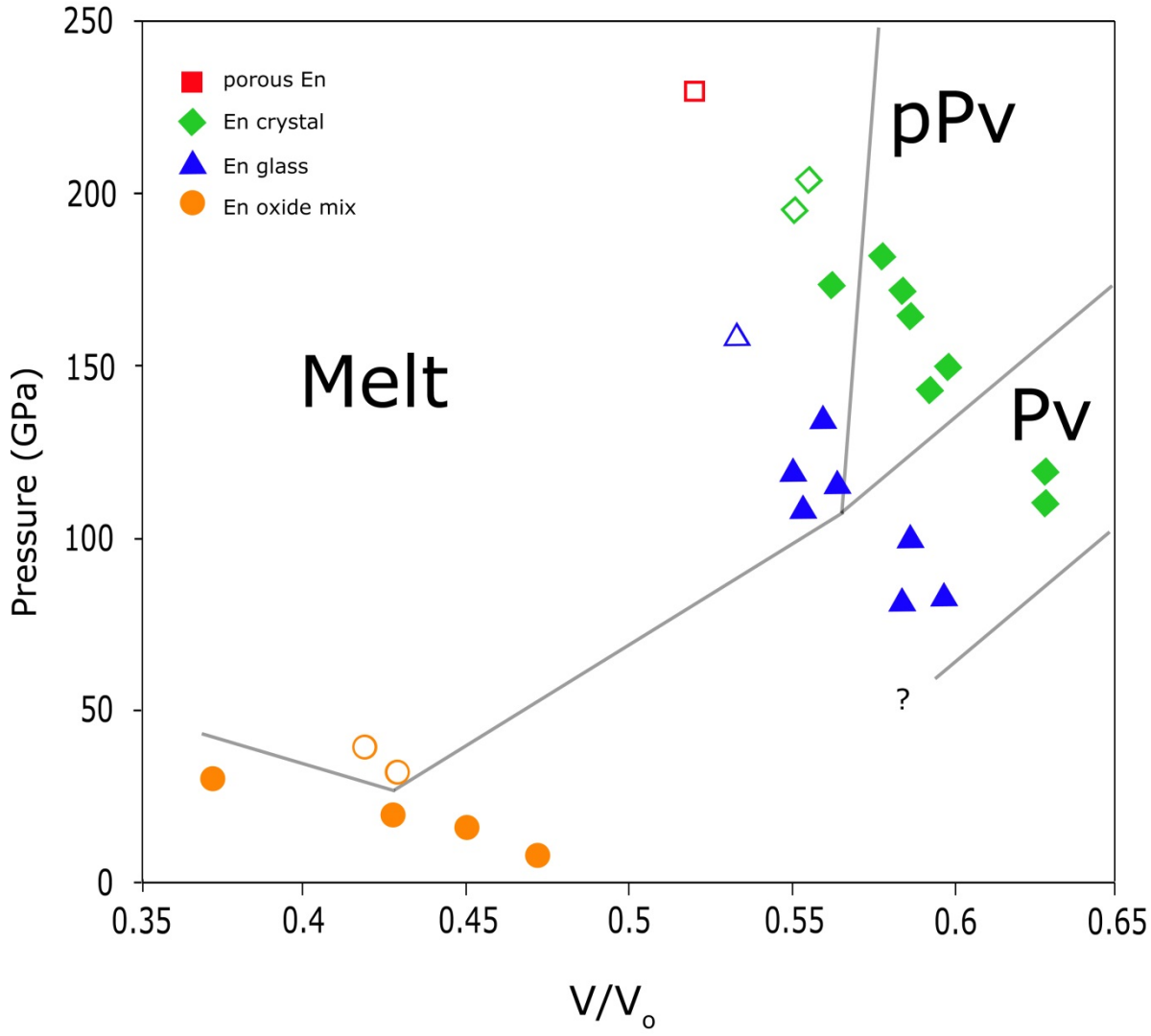
porous En
En crystal
En glass
En oxide mix
Melt
pPv
Pv
?
Pressure (GPa)
V/V$_o$
250
200
150
100
50
0
0.35
0.4
0.45
0.5
0.55
0.6
0.65

Figure 5

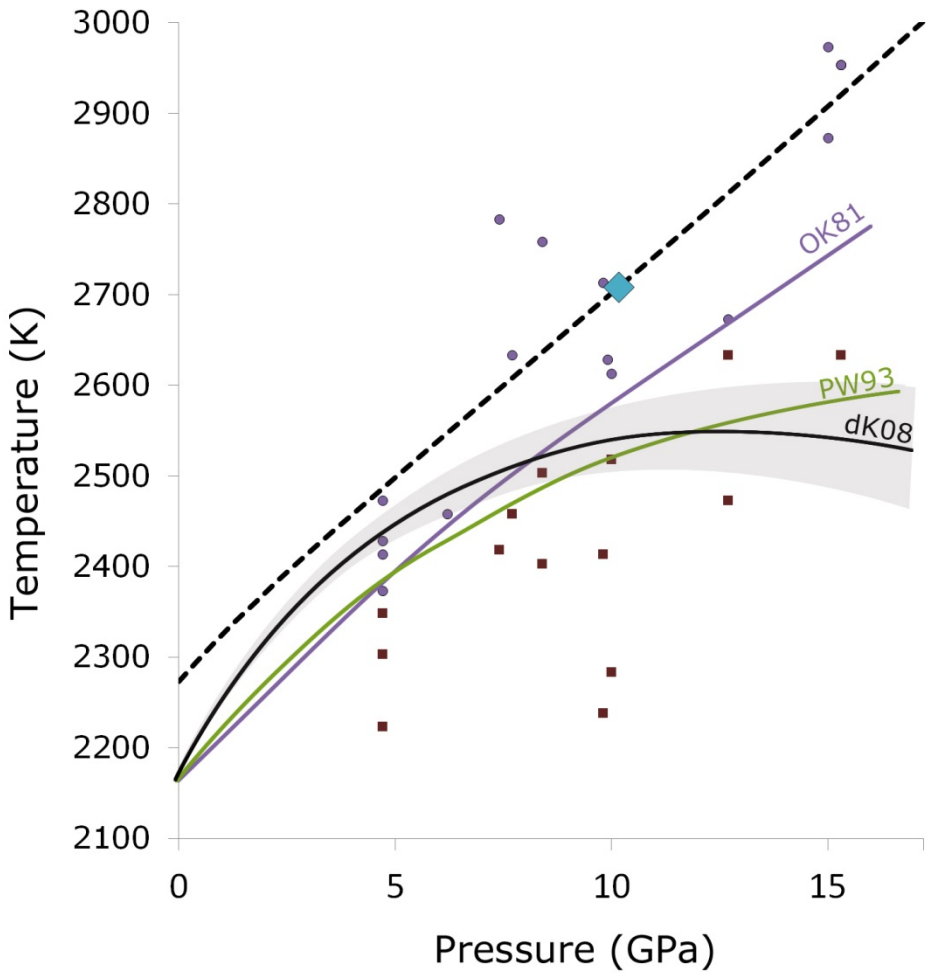
3000
2900
2800
2700
2600
2500
2400
2300
2200
2100
Temperature (K)
0
5
10
15
Pressure (GPa)
OK81
PW93
dK08

Figure 6

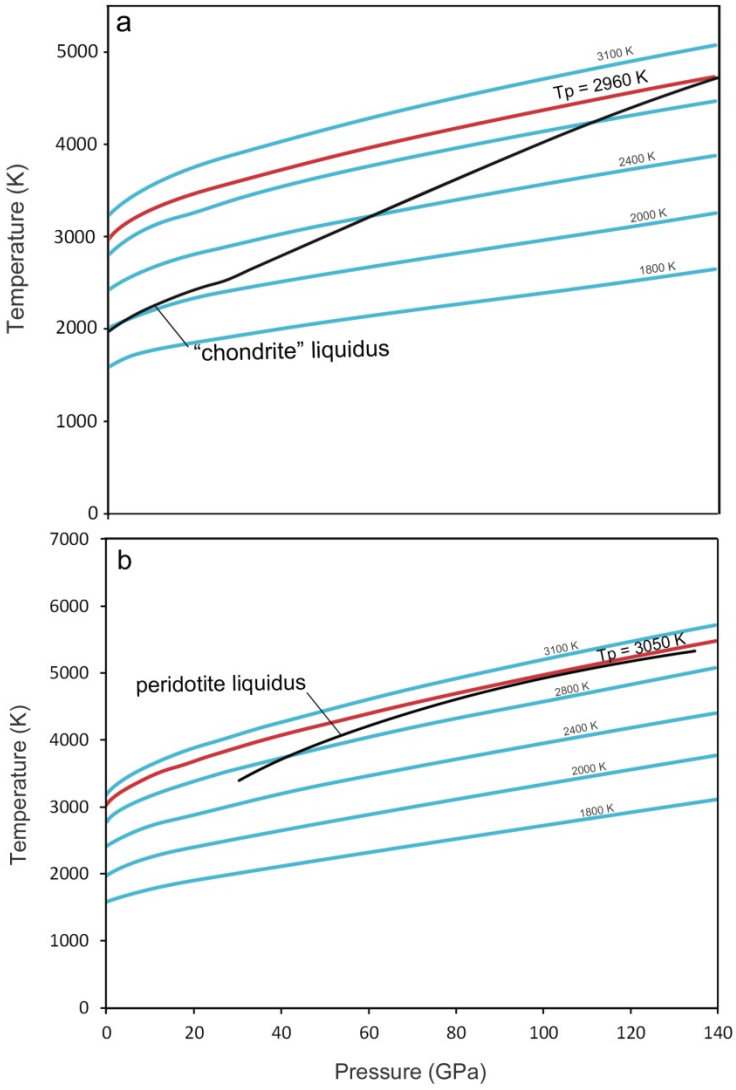
a
3100 K
Tp = 2960 K
2400 K
2000 K
1800 K
"chondrite" liquidus
Temperature (K)
0
1000
2000
3000
4000
5000
b
3100 K
Tp = 3050 K
peridotite liquidus
2800 K
2400 K
2000 K
1800 K
Temperature (K)
0
1000
2000
3000
4000
5000
6000
7000
0
20
40
60
80
100
120
140
Pressure (GPa)

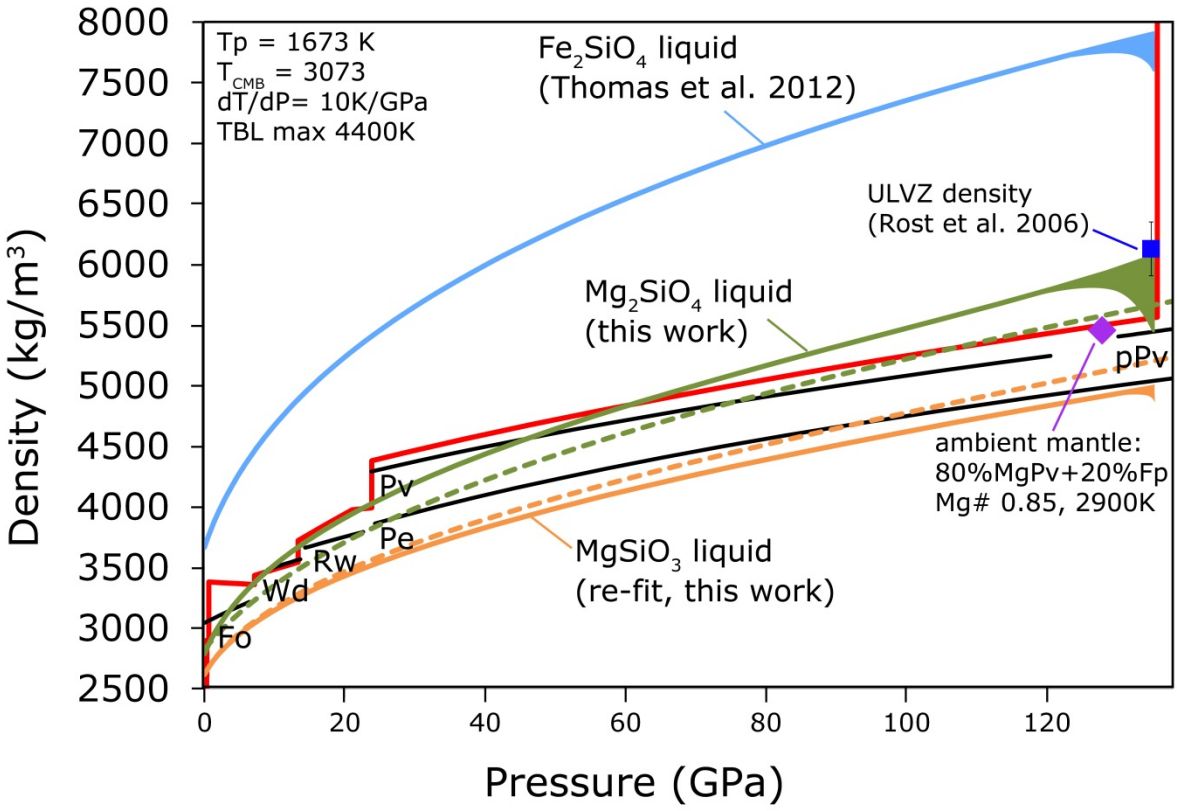

Figure 8

Figure 7

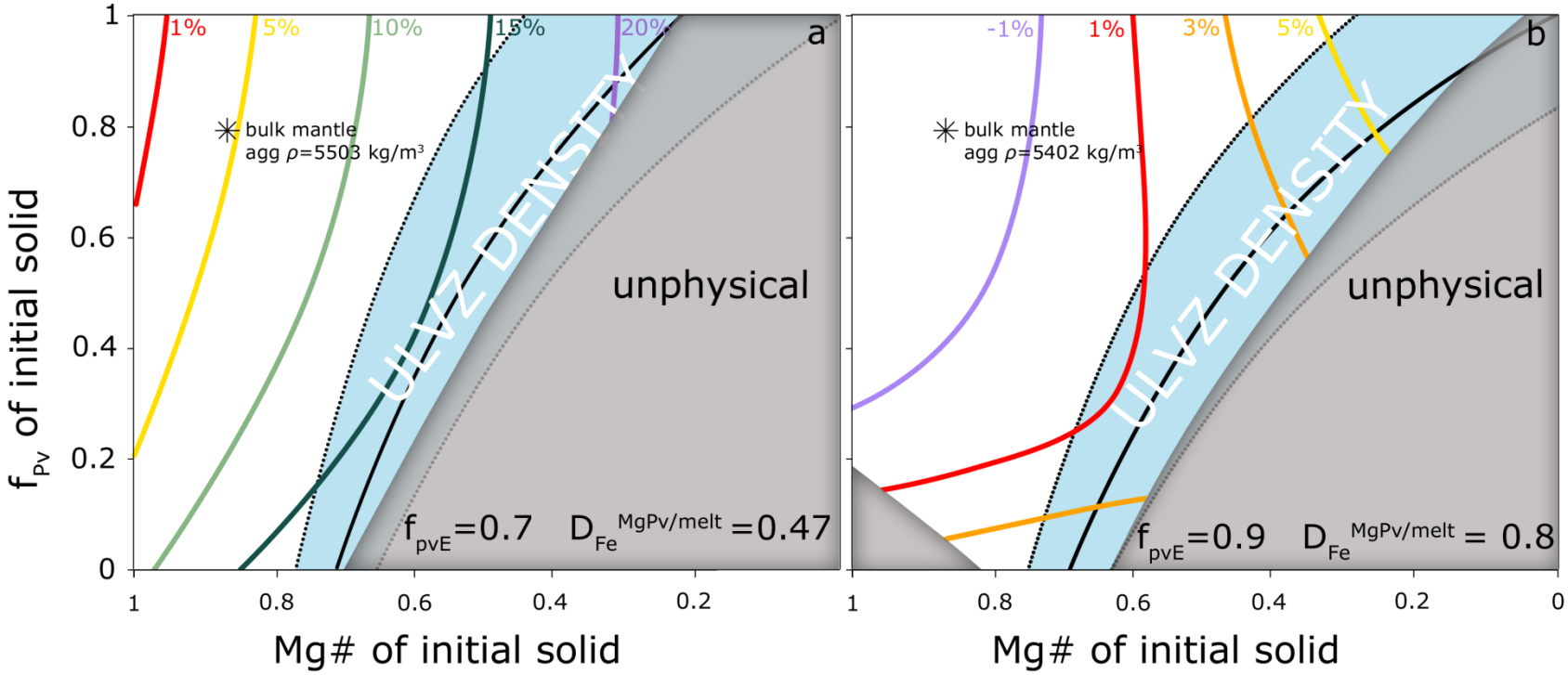
1%
5%
10%
15%
20%
a
bulk mantle
agg ρ=5503 kg/m³
ULVZ DENSITY
unphysical
f_pvE=0.7 D_Fe^MgPv/melt=0.47
-1%
1%
3%
5%
b
bulk mantle
agg ρ=5402 kg/m³
ULVZ DENSITY
unphysical
f_pvE=0.9 D_Fe^MgPv/melt = 0.8
f_Pv of initial solid
Mg# of initial solid
Mg# of initial solid
1
0.8
0.6
0.4
0.2
0

Figure 9

Chapter IV

Pre-heated shock experiments in the molten $CaAl_2Si_2O_8$-$CaFeSi_2O_6$-$CaMgSi_2O_6$ ternary: a test for linear mixing of liquid volumes at high pressure and temperature

Claire W. Thomas

Paul D. Asimow

For submission to

Journal of Geophysical Research

April 4, 2013

ABSTRACT

We performed seventeen new shock wave experiments on pre-heated (1673 K) hedenbergite liquid ($CaFeSi_2O_6$) and two model basalt liquids (an equimolar binary mix of $CaAl_2Si_2O_8$ + $CaFeSi_2O_6$ and an equimolar ternary mix of $CaAl_2Si_2O_8$ + $CaFeSi_2O_6$ +$CaMgSi_2O_6$) in order to determine their equations of state (EOS). Ambient-pressure density measurements on these and other Fe-bearing silicate liquids indicate that FeO has a partial molar volume that is highly dependent on composition, which leads to large errors in estimates of the densities of Fe-bearing liquids at ambient pressure based on an ideal mixing of any fixed set of end-member liquids. We formulated a series of mixing tests using the EOS determined in this study to examine whether ideal mixing of volumes might nevertheless suffice to describe the ternary system $CaAl_2Si_2O_8$-$CaFeSi_2O_6$-$CaMgSi_2O_6$ at high temperature and pressure. The ideal mixing null hypothesis is rejected; compositional variations in partial molar volume of FeO appear to extend to high pressure. Only densities of Fe-bearing liquid mixtures with oxide mole fraction of FeO less than 0.06 can be adequately approximated using an ideal solution.

INTRODUCTION

Silicate liquids play a large role in our understanding of both the early and modern Earth. Most widely-accepted scenarios for the evolution of the early Earth involve at least one stage of extensive or complete melting, for example, in the aftermath of impacts with large proto-planetary sized objects such as the presumed moon-forming event [*Canup*, 2004; 2012; *Canup and Asphaug*, 2001; *Ćuk and Stewart*, 2012]. The chemical and thermal evolution of the early molten mantle and how it affects the chemistry and physical properties of the modern mantle are not well understood. Furthermore, seismic observations of the 410km discontinuity in the upper mantle [*Revenaugh and Sipkin*, 1994; *Song et al.*, 2004] and ultralow velocity zones (ULVZ) in the lowermost mantle [*Garnero and Helmberger*, 1995; *Williams and Garnero*, 1996] have been interpreted to indicate the presence of a neutrally buoyant partial melt, yet there is currently limited knowledge of how the density and compressibility of complex silicate liquids behave at high temperature and pressure. It is therefore essential to have experimental constraints on the equation of state (EOS) of the complex multicomponent silicate liquids that would be actually present in nature. The difficulty lies in that natural silicate liquids comprise a potentially infinite, multi-dimensional continuum of compositions. Understanding their range of volumetric behavior requires either data on an arbitrarily large number of experiments or data on a minimum set of end-member compositions along with a reliable tool of interpolating among them. Choosing the correct method of interpolation is key to producing a predictive model for silicate liquid density and compressibility over a wide range of pressure, temperature, and composition space. Experimental data that provide constraints on end-member volumes as well as a few intermediate compositions offer the opportunity to test whether available methods for such interpolation are reliable.

Ideal mixing of volumes has proven to be a reliable method of interpolation for ambient-pressure experiments within a given compositition and temperature range [*Bottinga and Weill*, 1970; *Bottinga et al.*, 1982; *Bottinga et al.*, 1983; *Guo et al.*, 2013a submitted; *Lange*, 1997; *Lange and Carmichael*, 1990; *Mo et al.*, 1982; *Nelson and Carmichael*, 1979], although exceptions from ideality exist and are discussed below. Likewise, ideal mixing silicate liquid volumes at high pressure has been employed as a simplifying assumption, but it in fact remains poorly tested and constrained [*Asimow and Ahrens*, 2010]. In this study, we report seventeen new shock wave experiments to pressures up to 146 GPa on preheated silicate liquids of three separate compositions: hedenbergite (Hd; $CaFeSi_2O_6$), a 50-50 mixture of anorthite and hedenbergite (An-Hd; $CaAl_2Si_2O_8$-$CaFeSi_2O_6$), and an equal mixture of anorthite, hedenbergite, and diopside (An-Hd-Di; $CaAl_2Si_2O_8$-$CaFeSi_2O_6$-$CaMgSi_2O_6$). Determination of the EOS of Hd and the two mixtures (or "model basalts") permits us to test the validity of linear mixing of volumes and ideal configurational mixing of entropies — two assumptions which were both used in *Thomas et al.* [2012] and Chapter III of this text to predict the volumes of multicomponent liquids at high T and P.

METHODS

Sample preparation

The synthesis and analysis for the Hd and model basalt samples used in this study are described in *Guo et al.* [2013a submitted] and *Guo et al.* [2013b in prep], respectively. These studies also describe the 1-bar double-bob Archimedean density measurements and the ultrasonic sound speed measurements that were completed on these materials. The sample materials used for the shock wave experiments were cored directly from the lower buffer rod crucible used in

the sound speed determinations. The cores were sliced into disks, which were then lapped down to under-fill the volume of the molybdenum shock-experiment sample holder. The Mo sample holders are assembled from two machined pieces: 1) the driver plate, which has a hollow cylindrical projection on one side that becomes the sample well and 2) the cap, which is a 1 mm-thick, 8 mm-diameter disk that is welded on after filling (for complete description of the welding process see *Thomas et al*. [2012]). The interior volume of the sample well is 8 mm in diameter and 2.5 mm deep. The samples under-filled this volume by 7-13% at room temperature to prevent the welded cap from bowing during heating [c.f. *Thomas et al.*, 2012]

The surfaces within the sample well including the inside surface of the cap were polished to a mirror finish with 1-micron alumina grit. Smoothing all the surfaces prevents bubbles from clinging to the walls of the sample holder during heating and potentially interfering with the imaged shock wave. The outer surface of the cap was left with the finish quality as-machined (~9-micron finish), in order to match the quality of polish on the inner portion of the rear-face of the driver plate, which was polished on a rotating stage. The speed of the polishing pad decreases towards the center, hence the quality of mirror finish also decreases. Approximately similar finishes on the cap and driver reflecting surfaces ease acquisition of evenly illuminated images of the cap and driver during the shot and greatly increased the precision of the Hd data given below. On the contrary, the model basalt capsules were polished as in the manner as described in Chapter II due to the larger quantity of light needed for the digital recording system (c.f. Chapter III). Hence this dataset is plagued with larger errors derived from determining the driver and cap arrivals with different exposure levels. An improved technique for polishing for driver to a mirror finish would greatly aid data acquisition in the future. Additional sample preparations are detailed in *Asimow and Ahrens* [2010], *Thomas et al*. [2012], and Chapter III.

Experimental setup

The pioneering work for shock studies on molten materials is *Rigden et al.* [1984]. The description of our methods below builds on this and the work of *Rigden et al.* [1988; 1989], *Miller et al.* [1988; 1991a], *Chen and Ahrens* [1998], and *Chen et al.* [2002]. The most recent changes to experimental techniques and data analysis are in *Asimow* [2008], *Asimow and Ahrens* [2010], *Thomas et al.* [2012], and Chapter III.

For this study, seventeen total experiments were performed—twelve in the Caltech 90/25-mm two-stage light-gas gun and five using the Caltech 40-mm propellant gun—eight performed on Hd, five performed on An-Hd, and four performed on An-Hd-Di (see Table 1). All shots were preheated to 1673 K ± 4 K (1400 °C) and used either molybdenum (Mo), tantalum (Ta), or aluminum alloy (Al2024) flyer plates. Flyer plate velocities (u_{fp}) ranged from 1.46 – 6.19 km/s; the methods used for measuring u_{fp} are given in *Thomas and Asimow* [submitted].

During each experiment, the rear face of the target is illuminated by a Specialised Imaging xenon spark lamp and filmed by a Hadland Imacon 790 streak camera through a narrow (25 μm) slit focused horizontally across the center of the driver and sample cap. Hd shots were recorded on Polaroid film; the model basalts were recorded using a digital system (c.f. Chapter III). As the shock wave reaches the free surface of the driver or the cap the reflected light from the polished surface is extinguished (or shows a sharp change in intensity). The offset time of these two cutoffs allows for the precise measurement of the shock transit time through the sample and molybdenum cap.

To correct for non-uniform streaking rate, the camera was calibrated using a test streak image modulated by a radio-frequency tuner at 148.9875 MHz for a 1500 ns streak length and by a pulse generator at 1.7870 MHz for a 5000 ns streak (shot 1068). Each pixel line on the shot

streak record can then be converted to a time during the experiment, which permits the shock transit time through the sample to be calculated from the pixel distance between the two cutoffs on the film (or digital image). A detailed method for picking cutoffs and reducing the data is described in *Thomas et al.* [2012].

The final calculated shock state — i.e., shock pressure (P_H), shock density (ρ_H), particle velocity (u_p), and shock velocity (U_s) is solved for iteratively [*Rigden et al.*, 1988] using measured shock wave travel time, impedance matching, the Rankine-Hugoniot equations, Hugoniot data (ρ_o, C_o, s) for the metal flyer plates and hot Mo driver (Table 2), and the initial density (ρ_o) for each of the silicate liquids (see Tables 3, 4, and 5). An initial guess for the bulk sound speed (C_o) and Hugoniot slope s is required to seed the iteration, but the converged result is independent of this assumption.

RESULTS

The shock wave data are reported in Table 1, including shot number, flyer material, the temperature prior to firing, u_{fp}, u_p, U_S, ρ_H, and P_H.

A Hugoniot is a series of peak shock states achieved by progressively stronger shocks in a material from the same initial conditions [*Ahrens*, 1987]. The Hugoniot of a well-behaved material empirically forms a line in U_S-u_p space, given to third order in strain by $U_S = C_o + s\,u_p$ [*Jeanloz*, 1989]. The bulk sound speed of the material at room pressure, C_o, is given by the intercept; the slope (s) is related to K'_S, the isentropic pressure derivative of the isentropic bulk modulus (K_{oS}) by [*Ruoff*, 1967],

$$s = \frac{(K'_S + 1)}{4}. \qquad (1)$$

Hedenbergite ($CaFeSi_2O_6$) liquid

Figure 1 shows linear fits to the Hd shock data in U_S-u_p space. An unweighted linear fit to all eight preheated hedenbergite liquid data points yields $U_S = 2.587\pm0.142 + 1.55\pm0.04\ u_p$ km/s ($r^2 = 0.996$). The experimentally determined ultrasonic value of the bulk sound speed, 2.613±0.016 km/s [*Guo et al.*, 2013a submitted], lies within the stated uncertainty of the bulk sound speed derived from the intercept of this fit, 2.587±0.142 km/s. This relationship indicates relaxed (liquid-like) — as opposed to un-relaxed (glass-like) — behavior upon shock compression [*Rigden et al.*, 1988]. Therefore, to reduce the error on the linear fit, we fixed the intercept at the mean ultrasonic value yielding an unweighted constrained linear fit of $U_S = 2.613\pm0.016 + 1.54\pm0.01\ u_p$ km/s ($r^2 = 0.999$).

It is necessary to select and apply a thermal equation of state formalism for investigating material properties that lie off the Hugoniot, since the Hugoniot achieves temperatures and energies much higher than those of geophysical interest at lower mantle pressures (even for processes during early Earth differentiation). We have defined the entire *P-V-E* surface of hedenbergite liquid using various formalisms: the shock wave equation of state (SWEOS) and the 3rd- and 4th-order Birch-Murnaghan Mie-Grüneisen equations of state (3BM/MG and 4BM/MG). For a full description of the thermal EOS equations and fitting procedures, the reader is directed to *Asimow and Ahrens* [2010] and *Thomas et al.* [2012]. The results and uncertainties for each fit on Hd are given in Table 3, and the Hugoniots are plotted in Figure 2.

The SWEOS is define by a linear Hugoniot in $U_S - u_p$ space, converted to P - ρ space using the first and second Rankine-Hugoniot equations [e.g,. *Ahrens*, 1987]. States that lie off the Hugoniot are found using the Mie-Grüneisen thermal pressure approximation with a temperature-independent power law expression for the thermodynamic Grüneisen parameter

$$\gamma(\rho) = \gamma_o \left(\frac{\rho_o}{\rho} \right)^q . \quad (2)$$

Although a value for q to be used with the SWEOS was not independently determined in this study, experimental results thus far indicate that silicate liquids—including iron-bearing liquids [*Thomas et al.*, 2012]—appear to have q values of –0.88 to –2 for compressions of $1 > \rho_o/\rho > 0.49$. The slope and intercept of the constrained Hugoniot fit given above corresponds to a K'_S value of 5.16±0.04 derived from (1) and a K_{oS} value of 19.98±0.24 GPa derived from the expression

$$C_o = \sqrt{\frac{K_{oS}}{\rho_o}} . \quad (3)$$

The 3rd- or 4th-order BM/MG EOS is defined by a 3rd- or 4th-order Birch-Murnaghan isentrope centered at 1 bar and 1673K and a Mie-Grüneisen thermal pressure approximation. The 3BM/MG fit result is K_S' = 6.22±0.55, q = –1.93±0.41, and reduced χ^2= 4.20. The 4BM/MG fit result is K_S' = 3.15±1.67, K_S'' = 0.78±0.60 GPa^{-1}, q = 0.47±9.86 and reduced χ^2 = 3.26. The high precision for most of the points in the Hd dataset propagates into unusually high χ^2 values for both fits. Nevertheless, comparatively the 4BM/MG has very large error bars on and strong correlations among the output parameters indicating a very unstable fitting routine. The 3BM/MG fit, by contrast, has less severe correlation between the parameters and appears justified by the fitting statistics. Hence for this data set we prefer the 3rd-order fit.

An-Hd liquid

The An-Hd Hugoniot in U_S-u_p space is shown in Figure 3. The unweighted linear fit is U_S = 2.742±0.282 + 1.40±0.09 u_p km/s (r^2 = 0.986). As observed above for Hd liquid, the An-Hd liquid appears to be relaxed upon compression as the experimentally determined bulk sound speed, 2.772±0.011 km/s [*Guo et al.*, 2013b in prep], and the intercept are within error. We can then fix the intercept at the mean ultrasonic value yielding an unweighted constrained linear fit of U_S = 2.772±0.011 + 1.39±0.03 u_p km/s (r^2 = 0.998). This slope and intercept constrain the SWEOS K'_S and K_{oS} values to be 4.54±0.12 and 21.30±0.25 GPa, respectively.

The 3BM/MG fit result is K_S' = 5.49±0.65, q = –0.18±2.25, and reduced χ^2 = 6.37. The 4BM/MG fit result is K_S' = 5.10±1.61, K_S" = –0.17±0.60 GPa^{-1}, q = 1.67±2.79 and reduced χ^2 = 12.53. Both fits have relatively large error bars and large reduced χ^2 due to the low number of data points and fairly significant scatter in P-ρ space (Figure 4). Yet both fits give similar K'_S to SWEOS, which is well defined by the linear fit. We therefore prefer the 3rd-order fit despite having large errors, since it fits the data sufficiently well, has a lower reduced χ^2, and exhibits a negative q value, which has been shown to be typical for silicate liquids (see Chapter III). The EOS parameters and their uncertainties for An-Hd liquid are given in Table 4.

An-Hd-Di liquid

The An-Hd Hugoniot in U_S-u_p space is shown in Figure 5. The unweighted linear fit is U_S = 2.823±0.197 + 1.52±0.09 u_p km/s (r^2 = 0.995). Behaving as the two liquids above, An-Hd-Di liquid is relaxed upon compression [*Guo et al.*, 2013b in prep], which justifies an unweighted constrained linear fit of U_S = 2.846±0.014 + 1.54±0.02 u_p km/s (r^2 = 0.999). This slope and

intercept constrain the SWEOS K'_S and K_{oS} values to be 5.15±0.06 and 22.03±0.25 GPa, respectively.

The An-Hd-Di liquid was fit only with the 3BM/MG, as fitting the 4BM/MG to so few data points is under-constrained and does not yield a meaningful reduced χ^2. The 3BM/MG result is K_S' = 6.20±0.17, q = –1.14±0.79, and reduced χ^2 = 0.39. The results and uncertainties for each fit on An-Hd-Di are given in Table 5, and the Hugoniots are plotted in Figure 6.

DISCUSSION

Linear mixing assumptions

To make progress on calculating the volumetric properties of the natural multi-component silicate liquids that may occur in the lower mantle, the plan has been to constrain the EOS for a number of important end-member liquids using shock wave studies and then to attempt to reliably interpolate among them. End-member liquids that have been determined previously using shock wave methods are: Fe_2SiO_4 (Fa, fayalite), Mg_2SiO_4 (Fo, forsterite), $MgSiO_3$ (En, enstatite), $CaAl_2Si2O_8$ (An, anorthite), and $CaMgSi_2O_6$ (Di, diopside). The recommended EOS parameters for each of these end members are given in Chapter III. In *Thomas et al.* [2012], these five end members were used to interpolate within the CaO-MgO-Al_2O_3-SiO_2-FeO major element component space to constrain the volume of a liquid along an isentropic temperature-pressure path for a desired composition, yet there was not a clear test of the validity of the two underlying assumptions: (1) linear mixing of volumes and (2) constant entropy of mixing for a given composition.

The assumption of linear or ideal mixing is simplest assumption that can be made for mixtures,

$$V_{tot} = \sum_i X^i V^i + V_{mix} , \quad (4)$$

where the volume of mixing (V_{mix}) is assumed to be zero, and hence the total volume (V_{tot}) is just a linear combination of the end-member partial molar volumes (V^i) multiplied by their respective mole fractions (X^i). The second assumption is that the configurational entropy of a liquid solution is only a function of composition and therefore does not change with variations in temperature and pressure, such that

$$S_{tot} = \sum_i X^i S^i + S_{mix} , \quad (5)$$

where the entropy of mixing (S_{mix}) is assumed to be a constant and hence an isentrope or constant entropy path in *T-P* space can be found from

$$dS_{tot} = d\sum_i X^i S^i = \sum_i X^i \left(C_P^i d\ln(T) - \frac{\partial V^i}{\partial T}_P \mathrm{d}P \right) = 0, \quad (6)$$

where the T and P derivatives of entropy come from standard thermodynamic identities. Our data do not provide a test of this method of computing isentropes, since we lack experimentally defined isentropes for reference. We therefore focus on evaluating the volume of mixing assumption by comparing isentropes for intermediate compositions constructed with different sets of end members, while acknowledging that this exercise may be compromised to some extent by the configurational entropy issue.

Glass and 1-bar melt data

Both of these assumptions have historically performed fairly well at 1 bar. Linear mixing of temperature-independent partial molar heat capacities has been a successful model for most silicate liquids [*Stebbins et al.*, 1984]. Similarly, linear mixing of volumes has been successful in

determining silicate liquid densities in most major element space (SiO_2-Al_2O_3-MgO-CaO-Na_2O-K_2O) [*Lange*, 1997; *Lange and Carmichael*, 1990]. However, exceptions to both rules do exist. Heat capacities for the Fe_2O_3 oxide component were shown to vary strongly with composition [*Lange and Navrotsky*, 1992] and the partial molar volumes of Fe_2O_3 and TiO_2 components are both variable with composition. These exceptions are attributed to the Fe^{3+} and Ti^{4+} cations having multiple coordination states at ambient pressure that are highly dependent on the composition, i.e., fraction of non-SiO_2 components [*Liu and Lange*, 2001; 2006].

More recent results have found this to be potentially true for Fe^{2+} as well, in that the partial molar volume of FeO (V_{FeO}) in a melt is observed to depend on composition in some cases [*Guo et al.*, 2013a submitted; 2013b in prep]. Such behavior of Fe^{2+} is well documented in the glass literature, which is important insofar as glasses provide a proxy for structural properties of melt at the glass transition temperature. When discussing melt structure, language is typically borrowed from random network theory [*Zachariasen*, 1932], which distinguishes oxides as network formers, network modifiers, or intermediates. Network-forming cations (e.g., Si^{4+}) occur typically in tetrahedral ([4]) oxygen coordination in various connected units in the melt, whereas network modifiers (e.g., CaO, MgO) typically occupy octahedrally ([6]) coordinated sites and disrupt the tetrahedral network. Intermediates (e.g., Al_2O_3, TiO_2) can take on either role, may occupy multiple coordination sites, and may either disrupt or stabilize the polymerization of a melt [*Bottinga and Weill*, 1972; *Mysen*, 1983; 1988]. This is a simplified view of glasses and melts, but it acts to guide our intuition concerning the behavior of cations and the contributions of Fe^{3+} and Ti^{4+} to the density, heat capacity, and other thermodynamic properties of silicate melts [*Burns*, 1993; *Mysen*, 1988].

FeO is an intermediate glass former and has been documented to take on a range of [4] to [6] coordination dependent on composition. Fe^{2+} is predominantly a network modifier in basaltic glasses [*Burns*, 1993; *Jackson et al.*, 2005; *Mysen*, 1983; 1988] and also likely in melts with similar SiO_2 mole fraction. This is supported by the relatively low 1-bar V_{FeO} value (~ 12.1 cm^3/mol) for An-Hd, An-Di-Hd, and Hd-Di model basalts at 1732 K. This V_{FeO} has been inferred to indicate an average Fe^{2+} coordination of ~[5.7] due to its similarity to the molar volume of wüstite, crystalline FeO (in which Fe^{2+} is octahedrally coordinated) [*Guo et al.*, 2013b in prep]. On the contrary, Fe_2SiO_4 glasses contain very low-coordinated Fe^{2+} and are surprisingly polymerized [*Cooney and Sharma*, 1990]. X-ray absorption spectroscopy studies of both glass and melt of fayalite composition infer an average coordination of ~[4] [*Jackson et al.*, 1993]. This is again supported by melt densities, where V_{FeO} increases to ~14-17 cm^3/mol [*Mo et al.*, 1982; *Shiraishi et al.*, 1978; *Thomas et al.*, 2012], similar to the molar volume of crystalline $CaFeO_2$, a structure in which Fe^{2+} is [4] coordinated [*Guo et al.*, 2013a submitted].

Between these two extremes, Hd and the CaO-FeO-SiO_2 (CFS) melts measured in *Guo et al.* [2013a submitted] display FeO in an average coordination state intermediate between [4] and [6]. The V_{FeO} for Hd melt (~ 15.47 cm^3/mol) is inferred to indicate [4.7] coordination, similar to the values in Hd glasses (~4.3) and in molecular dynamics simulation of this melt [*Rossano et al.*, 2000]. The inferred coordination for CFS glasses range from 4.6-5.2. *Guo et al*. [2013b in prep] present an inverse correlation between CaO concentration and average Fe^{2+} coordination number. This is contrary to expectation from the model in *Jackson et al.* [2005] based on valence bond (VB) theory, which suggests a direct correlation between CaO concentration and FeO coordination. In the VB model, the Ca would have a greater “share” of the O valence due to the

higher bond valence of the Ca-O bond and force Fe to find charge balance with other oxygens and hence increase coordination.

The composition dependence of Fe coordination in CFS melts appears to be more strongly related to the degree of polymerization (Si/O ratio) [*Burns*, 1993]. For example in Hd, where SiO_2 is high (Si/O =0.32) and there are equal proportions of CaO and FeO, FeO fills both roles of network former and modifier, with an average value of [4.7]. For the family of CFS melts studies by *Guo et al*. [2013b in prep], the Fe content is fixed (40 mol %) and so increasing CaO is coupled to decreasing SiO_2. The Fe^{2+} may be energetically forced to play the role of network former as CaO competes more effectively for octahedral sites. For fayalite liquid, the Si/O value is quite low (0.25), and FeO is again energetically favored as a network former to accommodate the charge balance of the oxygen, creating a highly polymerized glass as observed by Cooney and Sharma [1990]. Qualitatively, one can understand the importance of FeO as an intermediate behavior cation when Fe_2SiO_4 is compared to Mg_2SiO_4 melt, which has the same Si/O ratio. Since MgO is unable to act as a network former, Mg-rich melts typically have fully depolymerized structure and display very low viscosities.

The dependence of FeO coordination and molar volume on other cation concentration invalidates the assumption of linear mixing of volumes at 1 bar for FeO-bearing liquids. It is unclear, however, what effect pressure and temperature may have. For glasses, higher temperatures are believed to decrease the coordination of transition metals [*Jackson et al.*, 2005], and there is some evidence that cations in melts will favor a coordination state lower than that of the glass [*Jackson et al.*, 1993]. At low pressure, network forming SiO_4 tetrahedra predominate, but as P increases, Si^{4+} coordination increases (~6.5 at 150 GPa) [*Karki et al.*, 2007]. Less is known about the coordination of network modifiers at high pressure. Preliminary modeling of

Fe_2SiO_4 liquid shows decreasing Fe-O bond length and increasing coordination of Fe with pressure, but this does not constrain the effect of other cations [*Muñoz Ramo and Stixrude*, in review]. *Guo et al.* [2013a submitted] and *Guo et al.* [*Guo et al.*, 2013b in prep] provide indirect evidence that coordination of Fe^{2+} in basaltic melts may *decrease* towards [5] at moderate pressures (~5GPa).

The only previous test of linear mixing at high pressure and temperature was for Fe-free anorthite-diopside liquids [*Asimow and Ahrens*, 2010], which found the linear approximation suitable at elevated *T-P* conditions along the measured Hugoniots. Linear mixing appeared to fail at low temperatures, but this may have been an artifact of uncertainties in the large extrapolation downwards from the Hugoniot temperature. Another partial success for linear mixing was found in MD simulations of An-Di and also in MD simulations of the MgO-SiO_2 binary, each of which showed well-behaved mixing at high pressure which began to break down at lower pressure [*de Koker et al.*, 2013; *Martin et al.*, 2012].

Tests of linear mixing

Our first test examines whether the V_{FeO} difference between Fe_2SiO_4 and $CaFeSi_2O_6$ at 1 bar is still significant at high temperature and pressure. That is, can V_{FeO} for either end member substitute for the other, as it would in the case of ideal mixing of volumes? To test this we compare the Hd isentrope from shock wave experiments determined in this study to a modeled linear combination of end-member liquids, where $Hd_{modelFa}$ = Di + 0.5Fa – 0.5Fo. The equations and details of creating isentropes of mixtures are given in *Thomas et al.* [2012]. The results are shown in Figure 7, where it is apparent that the model does not capture the behavior of the Hd isentrope. The errors for temperature and density are highly correlated such that if the model

predicts a lower temperature than the actual isentrope, it will over predict the density and vice versa. Such is the case for Hd, where the errors at high pressure (~120 GPa) and temperature are maximized, and the model underestimates the temperature by 30% and overestimates the density by 20%. In this test, comparing the use of two Fe-rich end members, we find a failure of linear mixing and this is presumably due to complexity in the coordination state of Fe^{2+}.

Our second test examines the question: Which model will perform better in creating an Fe-rich model basalt, An-Hd — using V_{FeO} derived from Fa or V_{FeO} derived from Hd? Our expectation from 1 bar coordination numbers is that since Hd should be a better end member for modeling An-Hd. Two mixing models, $AnHd_{modelFa} = 0.5An + 0.25\ Fa - 0.25\ Fo + 0.5Di$ and $AnHd_{modelHd} = 0.5\ An + 0.5\ Hd$, are compared to the An-Hd isentrope determined in this study. It can be seen in Figure 8 that neither model is able to recover the An-Hd isentrope, but that the Fa model does significantly worse. The Fa model also becomes unphysical at high pressure and lower temperature (Fig. 8a) and this breaks the anticorrelation between errors in T and ρ, which are both underestimated, by 15% and 10% at 120 GPa, respectively (Fig. 8b). The Hd model does significantly better with maximum errors at 120 GPa that overestimate T by 6% and underestimate ρ by 7% (Fig. 8d). These errors worsen systematically for isentropes with progressively higher potential temperature (Fig. 8c). These results are in line with our expectations based on 1-bar results: neither Fa or Hd models can fully recover the behavior of the An-Hd isentrope, but closer similarity of V_{FeO} at 1-bar for Hd and An-Hd are significant enough to improve the fit at high pressure and temperature.

Our third test examines the question: As FeO content decreases, does the difference between the end-member V_{FeO} and that of the model basalt still play as significant of a role in the final volume of the mixture at high pressure and temperature? We attempt to recover the

isentrope of the model basalt, An-Hd-Di (which has less FeO than the previous An-Hd basalt), again using Fa and Hd end-member models: $AnHdDi_{modelFa}$ = 0.33An + 0.667Di + 0.167 Fa – 0.167 Fo and $AnHdDi_{modelHd}$ = 0.33 An + 0.33Hd + 0.33Di. The results in Figure 9 show improvement for both models with the Fa model having high-pressure errors that underestimate *T* by 12% and underestimate ρ by 4% and the Hd model overestimating *T* by only 3% and underestimating ρ by 3%. Again, the Hd model does significantly better than the Fa model, likely due to the greater structural similarity of FeO in Hd and in An-Hd-Di at 1 bar. This test also suggests, at least in the studied region of CaO-FeO-MgO-Al_2O_3-SiO_2, that the linear mixing approximation becomes better as the amount of FeO in the mixture decreases. That is, despite the variable behavior of V_{FeO}, there may be a threshold concentration of FeO below which this is negligible and the ideal solution approximation is adequate.

It still remains to define best choice for V_{FeO} (i.e., Fe^{2+} coordination state) for modeling a particular liquid composition in the mantle and to define the threshold FeO concentration below which this choice is unimportant. Our final test attempts to answer these questions by comparing the original chondrite model given in Chapter III that uses Fa as the V_{FeO} component ($Ch_{modelFa}$= 0.62En + 0.24Fo + 0.08Fa + 0.04An + 0.02Di), and a model which uses An-Hd-Di as the V_{FeO} component ($Ch_{modelAnHdDi}$ = 0.62En + 0.32Fo + 0.45AnHdDi – 0.12An –0.28Di). The results in Fig. 10 show that the An-Hd-Di model predicts a slightly higher temperature but that models are within ±1.5% for both *T* and ρ. Hence, the models are effectively indistinguishable, indicating that liquids with $X_{FeO} \leq 0.06$ (chondrite model [*Andrault et al.*, 2011]) can be suitably approximated with linear mixing. Mole fractions greater than this amount, such as An-Hd-Di (X_{FeO} = 0.08), can be approximated within reasonable error (±3%), but only when using an FeO component that has a similar V_{FeO} at 1 bar.

Direct knowledge of the coordination state of Fe^{2+} in a given liquid thus is an important constraint on the volume behavior of that liquid, especially for high FeO contents. Conversely, precise data on the equation of state of an Fe-bearing liquid can be interpreted primarily as a constraint on the coordination state of Fe^{2+} in that liquid. However, liquids containing Fe_2O_3, Na_2O, K_2O, varying amounts of SiO_2, and other oxide species are far more complex than the five-component system studied so far. Other cations may influence the Fe^{2+} coordination state and may have variable coordination states themselves. *In situ* experiments analyzing cation coordination of complex glasses and melts at high pressure and temperature would greatly aid in elucidating these consequences and complementing macroscopic constraints from shock wave or other equation of state measurements.

CONCLUSIONS

We completed seventeen new pre-heated shock wave experiments on Hd, An-Hd, and An-Hd-Di liquids to determine the EOS of each composition. Having data on more compositions than are necessary to span the multicomponent oxide system, we applied these data to testing the validity of ideal mixing of volumes as a method of interpolation among end-member liquids. Ambient-pressure density measurements on these and other Fe-bearing silicate liquids indicate that FeO has a molar volume (and therefore coordination state) that is highly dependent on composition [*Guo et al.*, 2013a submitted; 2013b in prep], and our results show that this behavior extends to high pressure. An Fe-bearing end member close in composition to the liquid of interest is necessary for adequately predicting temperature and density along its isentrope. We find that deviations from linear mixing of volumes are significant at the level of several percent for liquid mixtures with molar X_{FeO} >0.06. On the other hand, densities and isentropic gradients

for liquids in the system CaO-FeO-MgO-Al_2O_3-SiO_2 with less than this threshold concentration of FeO can be approximated both at ambient and at high pressure using ideal volume of mixing.

ACKNOWLEDGEMENTS

The authors would like to thank the following: the shock wave lab technical staff—Oleg Fat'yanov, Eprapodito Gelle, Russel Oliver, and Emma Dodd. Thanks to X. Guo and R. A. Lange for their ongoing collaboration and willingness to share their manuscripts. This work was supported by the National Science Foundation through award EAR-1119522.

REFERENCES

Ahrens, T. J. (1987), 6. Shock Wave Techniques for Geophysics and Planetary Physics, in *Methods in Experimental Physics*, edited by G. S. Charles and L. H. Thomas, pp. 185-235, Academic Press.

Andrault, D., N. Bolfan-Casanova, G. L. Nigro, M. A. Bouhifd, G. Garbarino, and M. Mezouar (2011), Solidus and liquidus profiles of chondritic mantle: Implication for melting of the Earth across its history, *Earth and planetary science letters*, *304*(1-2), 251-259.

Asimow, P. D., and T. J. Ahrens (2010), Shock compression of liquid silicates to 125 GPa: The anorthite-diopside join, *J. Geophys. Res.*, *115*(B10), B10209.

Asimow, P. D., D. Sun, and T. J. Ahrens (2008), Shock compression of preheated molybdenum to 300 GPa, *Physics of The Earth and Planetary Interiors*, *174*(1-4), 302.

Bottinga, Y., and D. F. Weill (1970), Densities of liquid silicate systems calculated from partial molar volumes of oxide components, *American journal of science*, *269*(2), 169-182.

Bottinga, Y., and D. F. Weill (1972), The viscosity of magmatic silicate liquids; a model calculation, *American journal of science*, *272*(5), 438-475.

Bottinga, Y., D. Weill, and P. Richet (1982), Density calculations for silicate liquids. I. Revised method for aluminosilicate compositions, *Geochimica et Cosmochimica Acta*, *46*(6), 909-919.

Bottinga, Y., P. Richet, and D. F. Weill (1983), Calculation of the Density and Thermal Expansion Coefficient of Silicate Liquids, *B Mineral*, *106*(1-2), 129-138.

Burns, R. G. (1993), *Mineralogical Applications of Crystal Field Theory* 2nd ed., Cambridge University Press, Cambridge, UK.

Canup, R. M. (2004), Simulations of a late lunar-forming impact, *Icarus*, *168*(2), 433-456.

Canup, R. M. (2012), Forming a Moon with an Earth-Like Composition via a Giant Impact, *Science*.

Canup, R. M., and E. Asphaug (2001), Origin of the Moon in a giant impact near the end of the Earth's formation, *Nature*, *412*(6848), 708-712.

Chase, M. W. (1998), NIST-JANAF Thermochemical Tables, *Journal of Physical and Chemical Reference Data*, *4th edition*(Monograph 9), 1–1951.

Chen, G. Q., and T. J. Ahrens (Eds.) (1998), *Radio frequency heating coils for shock wave experiments*, 63-71 pp., Materials Research Society Symposia Proceedings, Warrendale, PA.

Chen, G. Q., T. J. Ahrens, and E. M. Stolper (2002), Shock-wave equation of state of molten and solid fayalite, *Physics of The Earth and Planetary Interiors*, *134*(1-2), 35-52.

Cooney, T. F., and S. K. Sharma (1990), Structure of glasses in the systems Mg_2SiO_4-Fe_2SiO_4, Mn_2SiO_4-Fe_2SiO_4, Mg_2SiO_4-$CaMgSiO_4$, and Mn_2SiO_4-$CaMnSiO_4$, *Journal of Non-Crystalline Solids*, *122*(1), 10-32.

Ćuk, M., and S. T. Stewart (2012), Making the Moon from a Fast-Spinning Earth: A Giant Impact Followed by Resonant Despinning, *Science*.

de Koker, N., B. B. Karki, and L. Stixrude (2013), Thermodynamics of the MgO–SiO2 liquid system in Earth's lowermost mantle from first principles, *Earth and planetary science letters*, *361*(0), 58-63.

Garnero, E. J., and D. V. Helmberger (1995), A very slow basal layer underlying large-scale low-velocity anomalies in the lower mantle beneath the Pacific: evidence from core phases, *Physics of The Earth and Planetary Interiors*, *91*(1-3), 161-176.

Guo, X., R. A. Lange, and Y. H. Ai (2013a submitted), The density and compressibility of CaO FeO-SiO_2 liquids: evidence for four-coordinated Fe^{2+} in the $CaFeO_2$ component, *Geochimica et Cosmochimica Acta*.

Guo, X., R. A. Lange, and Y. H. Ai (2013b in prep), Density and sound speed measurements on model basalt (An-Di-Hd) liquids at one bar: new constraints on the partial molar volume and compressibility of the FeO component, *Earth and Planetary Science Letters*.

Jackson, W. E., J. M. de Leon, G. E. Brown, G. A. Waychunas, S. D. Conradson, and J.-M. Combes (1993), High-Temperature XAS Study of Fe_2SiO_4 Liquid: Reduced Coordination of Ferrous Iron, *Science*, *262*(5131), 229-233.

Jackson, W. E., F. Farges, M. Yeager, P. A. Mabrouk, S. Rossano, G. A. Waychunas, E. I. Solomon, and G. E. Brown Jr. (2005), Multi-spectroscopic study of Fe(II) in silicate glasses: Implications for the coordination environment of Fe(II) in silicate melts, *Geochimica et Cosmochimica Acta*, *69*(17), 4315-4332.

Jeanloz, R. (1989), Shock Wave Equation of State and Finite Strain Theory, *J. Geophys. Res.*, *94*.

Karki, B. B., D. Bhattarai, and L. Stixrude (2007), First-principles simulations of liquid silica: Structural and dynamical behavior at high pressure, *Physical Review B*, *76*(10), 104205.

Lange, R. A. (1997), A revised model for the density and thermal expansivity of K_2O-Na_2O CaO-MgO-Al_2O_3-SiO_2 liquids from 700 to 1900 K: extension to crustal magmatic temperatures, *Contributions to Mineralogy and Petrology*, *130*(1), 1-11.

Lange, R. A., and I. S. E. Carmichael (1990), Thermodynamic properties of silicate liquids with emphasis on density, thermal expansion and compressibility, *Reviews in Mineralogy and Geochemistry*, *24*(1), 25-64.

Lange, R. A., and A. Navrotsky (1992), Heat capacities of Fe_2O_3-bearing silicate liquids, *Contributions to Mineralogy and Petrology*, *110*(2-3), 311.

Liu, Q., and R. A. Lange (2001), The partial molar volume and thermal expansivity of TiO_2 in alkali silicate melts: Systematic variation with Ti coordination, *Geochimica et Cosmochimica Acta*, *65*, 2379-2393.

Liu, Q., and R. A. Lange (2006), The partial molar volume of Fe_2O_3 in alkali silicate melts: Evidence for an average Fe^{3+} coordination number near five, *American Mineralogist*, *91*, 385-393.

Marsh, S. P. (Ed.) (1980), *LASL Shock Hugoniot Data* 658 pp., University of California, Berkeley.

Martin, G. B., M. S. Ghiorso, and F. J. Spera (2012), Transport properties and equation of state of 1-bar eutectic melt in the system $CaAl_2Si_2O_8$-$CaMgSi_2O_6$ by molecular dynamics simulation, *American Mineralogist*, *97*(7), 1155-1164.

Miller, G. H., T. J. Ahrens, and E. M. Stolper (1988), The equation of state of molybdenum at 1400 C, *Journal of Applied Physics*, *63*(9), 4469-4475.

Miller, G. H., E. M. Stolper, and T. J. Ahrens (1991a), The Equation of State of a Molten Komatiite 1 Shock Wave Compression to 36 GPa, *J. Geophys. Res.*, *96*.

Mitchell, A. C., and W. J. Nellis (1981b), Shock compression of aluminum, copper, and tantalum, *Journal of Applied Physics*, *52*(5), 3363-3374.

Mo, X., I. S. E. Carmichael, M. L. Rivers, and J. F. Stebbins (1982), The partial molar volume of Fe_2O_3 in multicomponent silicate liquids and the pressure-dependence of oxygen fugacity in magma, *Mineralogical Magazine*, *45*(337), 237-245.

Muñoz Ramo, D., and L. Stixrude (in review), Spin crossover in Fe_2SiO_4 liquid at high pressure,

Physical Review Letters.
Mysen, B. O. (1983), The structure of silicate melts, *Annual Review of Earth and Planetary Sciences*, *11*(1), 75.
Mysen, B. O. (1988), *Structure and Properties of Silicate Melts*, 354 pp., Elsevier, Amsterdam.
Nelson, S. A., and I. S. E. Carmichael (1979), Partial Molar Volumes of Oxide Components in Silicate Liquids, *Contributions to Mineralogy and Petrology*, *71*(2), 117-124.
Revenaugh, J., and S. A. Sipkin (1994), Seismic evidence for silicate melt atop the 410-km mantle discontinuity, *Nature*, *369*(6480), 474-476.
Rigden, S. M., T. J. Ahrens, and E. M. Stolper (1984), Densities of liquid silicates at high pressures, *Science*, *226*(4678), 1071-1074.
Rigden, S. M., T. J. Ahrens, and E. M. Stolper (1988), Shock compression of molten silicate: results for a model basaltic composition, *J. Geophys. Res.*, *93*(B1), 367-382.
Rigden, S. M., T. J. Ahrens, and E. M. Stolper (1989), High-Pressure Equation of State of Molten Anorthite and Diopside, *Journal of Geophysical Research*, *94*(B7), 9508-9522.
Rossano, S., A. Y. Ramos, and J. M. Delaye (2000), Environment of ferrous iron in $CaFeSi_2O_6$ glass; contributions of EXAFS and molecular dynamics, *Journal of Non-Crystalline Solids*, *273*(1–3), 48-52.
Ruoff, A. (1967), Linear Shock-Velocity-Particle-Velocity Relationship, *Journal of Applied Physics*, *38*(13), 4976.
Shiraishi, Y., K. Ikeda, A. Tamura, and T. Saito (1978), On the viscosity and density of the molten FeO-SiO2 system, T*ransactions of the Japan Institute of Metals*, ***19***, 264-274.
Song, T.-R. A., D. V. Helmberger, and S. P. Grand (2004), Low-velocity zone atop the 410-km seismic discontinuity in the northwestern United States, *Nature*, *427*(6974), 530-533.
Stebbins, J. F., I. S. E. Carmichael, and L. K. Moret (1984), Heat capacities and entropies of silicate liquids and glasses, *Contributions to Mineralogy and Petrology*, *86*(2), 131-148.
Thomas, C. W., and P. D. Asimow (submitted), Direct shock compression experiments on pre molten Mg_2SiO_4 and progress towards a consistent high-pressure equation of state for CaO-MgO-Al_2O_3-SiO_2-FeO liquids.
Thomas, C. W., Q. Liu, C. B. Agee, P. D. Asimow, and R. A. Lange (2012), Multi-technique equation of state for Fe_2SiO_4 melt and the density of Fe-bearing silicate melts from 0 to 161 GPa, *J. Geophys. Res.*, *117*(B10), B10206.
Williams, Q., and E. J. Garnero (1996), Seismic Evidence for Partial Melt at the Base of Earth's Mantle, *Science*, *273*(5281), 1528-1530.
Zachariasen, W. H. (1932), The atomic arrangement of glass, *Journal of the American Chemical Society*, *54*(10), 3841-3851.

TABLES

Table 1. Shock compression data

Shot #	Flyer material	T (K)	u_{fp} km s^{-1}		u_p km s^{-1}		U_s km s^{-1}		ρ_H Mg m^{-3}		P_H GPa	
Hedenbergite												
1068 [a]	Mo	1673	1.976	0.002	1.58	0.01	5.12	0.11	4.27	0.05	23.8	0.4
413	Al	1673	4.471	0.002	2.006	0.005	5.56	0.07	4.62	0.04	32.9	0.3
419	Mo	1674	3.497	0.001	2.68	0.02	6.59	0.24	4.99	0.17	52.2	1.5
418	Mo	1673	4.066	0.148	3.05	0.01	7.50	0.06	4.98	0.03	67.6	0.4
417	Ta	1677	4.535	0.005	3.65	0.01	8.29	0.10	5.29	0.05	89.1	0.6
416	Ta	1672	5.144	0.012	4.10	0.01	9.01	0.09	5.42	0.06	109.1	0.9
415	Ta	1673	5.613	0.001	4.46	0.01	9.46	0.05	5.59	0.03	124.5	0.5
414	Ta	1675	6.187	0.020	4.88	0.01	10.10	0.05	5.72	0.03	145.6	0.9
An-Hd												
1070 [a]	Mo	1673	2.006	0.003	1.62	0.01	5.17	0.12	4.04	0.05	23.2	0.4
1074 [a]	Mo	1673	1.456	0.002	1.211	0.014	4.27	0.28	3.87	0.13	14.3	0.8
466	Mo	1675	3.618	0.003	2.82	0.01	6.56	0.15	4.87	0.10	51.3	0.9
469	Mo	1673	4.700	0.003	3.55	0.01	7.99	0.10	4.99	0.06	78.7	0.8
471	Mo	1674	5.815	0.016	4.37	0.01	8.66	0.11	5.59	0.08	104.8	1.0
An-Hd-Di												
1069 [a]	Mo	1673	2.016	0.003	1.63	0.03	5.48	0.47	3.88	0.10	24.4	2.1
1071 [a]	Mo	1673	1.470	0.005	1.20	0.01	4.77	0.30	3.64	0.09	15.6	0.8
468	Mo	1673	3.503	0.008	2.70	0.01	7.00	0.07	4.43	0.03	51.5	0.4
470	Mo	1674	4.796	0.006	3.61	0.02	8.31	0.16	4.81	0.09	81.7	1.3

[a] Caltech 40mm propellant

Table 2. Parameters used

		Molybdenum[a] (2273 K)	Molybdenum[a] (300 K)	Tantalum[b] (300 K)	Aluminum 2024[c] (300 K)
ρ_o	Mg m^{-3}	9.785	10.21	16.65	2.78
C_o	km s^{-1}	4.858	5.033	3.293	5.330
s		1.288	1.289	1.307	1.34

[a]*Asimow et al.* [2008], *Chase*[1998]; [b] *Mitchell and Nellis* [1981b]; [c] *Marsh* [1980]

Table 3. Equation of State fits for molten $CaFeSi_2O_6$

	Units	SWEOS	BM3	BM4	Source
T_o	K	1673	1673	1673	
ρ_o	kg m^{-3}	2913 ± 11	2913 ± 11	2913 ± 11	G13a
C_o	m s^{-1}	2613 ± 16	-	-	G13a
s		1.54 ± 0.01	-	-	fitted
γ_o		0.300	0.300	0.300	derived
q		-	–1.93 ± 0.41	0.47 ± 9.86	fitted
K_{So}	GPa	19.89± 0.24	19.89± 0.24	19.89± 0.24	derived
K_S'		5.16 ± 0.04	6.22 ± 0.55*	3.15 ±1.61*	derived/*fitted
K_S''	GPa^{-1}	-	-	0.78± 0.60	fitted
χ^2		-	4.20	3.26	
K_T	GPa	19.32	19.32	19.32	derived
α	K^{-1}	5.91-05	5.91-05	5.91-05	G13a
C_p	J kg^{-1}	1345.48	1345.48	1345.48	LN92
C_v	J kg^{-1}	1306.70	1306.70	1306.70	derived

SWEOS= shock wave equation of state. 3BM/MG = 3rd-order Birch-Murnaghan/Mie-Grüneisen EOS 4BM/MG = 4th-order Birch-Murnaghan/Mie-Grüneisen EOS Sources: *Fitted* indicates an adjustable parameter, L97 is *Lange* [1997], LN92 is *Lange and Navrotsky* [1992], G13a is *Guo et al.* [2013a]

Table 4. Equation of State fits for molten An-Hd

	Units	SWEOS	BM3	BM4	Source
T_o	K	1673	1673	1673	
ρ_o	kg m^{-3}	2772 ± 3	2772 ± 3	2772 ± 3	G13b
C_o	m s^{-1}	2772 ± 11	-	-	G13b
s		1.39 ± 0.03	-	-	fitted
γ_o		0.310	0.310	0.310	derived
q		-	–0.18 ± 2.25	1.67 ± 2.79	fitted
K_{So}	GPa	21.30 ± 0.25	21.30 ± 0.25	21.30 ± 0.25	derived
K_S'		4.54 ± 0.12	5.49 ± 0.65*	5.10 ±1.61*	derived/*fitted
K_S''	GPa^{-1}	-	-	-0.17± 0.82	fitted
χ^2		-	6.37	12.53	
K_T	GPa	20.68	20.68	20.68	derived
α	K^{-1}	5.81-05	5.81-05	5.81-05	G13b
C_p	J kg^{-1}	1442.34	1442.34	1442.34	LN92
C_v	J kg^{-1}	1400.19	1400.19	1400.19	derived

Sources: *Fitted* indicates an adjustable parameter, L97 is *Lange* [1997], LN92 is *Lange and Navrotsky* [1992], G13b is *Guo et al.* [2013b]

Table 5. Equation of State fits for molten An-Hd-Di

	Units	SWEOS	BM3	Source
T_o	K	1673	1673	
ρ_o	kg m^{-3}	2722 ± 2	2722 ± 2	G13b
C_o	m s^{-1}	2846 ± 14	-	G13b
s		1.54 ± 0.02	-	fitted
γ_o		0.361	0.361	derived
q		-	–1.14 ± 0.79	fitted
K_{So}	GPa	22.03 ± 0.25	22.03 ± 0.25	derived
K_S'		5.15 ± 0.06	6.20 ± 0.17*	derived/*fitted
K_S''	Gpa^{-1}	-	-	fitted
χ^2		-	0.39	
K_T	Gpa	21.19	21.19	derived
α	K^{-1}	6.64-05	6.64-05	G13b
C_p	J kg^{-1}	1491.96	1491.96	LN92
C_v	J kg^{-1}	1434.47	1434.47	derived

For abbreviations see Tables 3 and 4

FIGURE CAPTIONS

Figure 1. Preheated (1673K) $CaFeSi_2O_6$ liquid Hugoniot in shock velocity (*U*s)-particle velocity (u_p) space. The dotted line represents the unconstrained linear Hugoniot, G13a is *Guo et al.*[2013a submitted].

Figure 2. $CaFeSi_2O_6$ liquid Hugoniot plotted in pressure-density space with thermal EOS fits. Data symbols are the same as Figure 1. Abbreviations: SWEOS- shock wave equation of state; BM/MG – Birch-Murnaghan/Mie-Grüneisen EOS, G13a is *Guo et al.* [2013a submitted].

Figure 3. Preheated (1673K) An-Hd liquid Hugoniot in shock velocity (*U*s)-particle velocity (u_p) space. The dotted line represents the unconstrained linear Hugoniot. G13b is *Guo et al.*[2013b in prep]

Figure 4. An-Hd liquid Hugoniot plotted in pressure-density space with thermal EOS fits. Data symbols are the same as Figure 3. The abbreviations are the same as Figure 2 and 3.

Figure 5. Preheated (1673K) An-Hd-Di liquid Hugoniot in shock velocity (*U*s)-particle velocity (u_p) space. The dotted line represents the unconstrained linear Hugoniot G13b is *Guo et al.* [2013b in prep]

Figure 6. An-Hd-Di liquid Hugoniot plotted in pressure-density space with thermal EOS fits. Data symbols are the same as Figure 6. The abbreviations are the same as Figure 2 and 5.

Figure 7. A comparison of the mixing model ($Hd_{modelFa}$ = Di +0.5Fa -0.5Fo) and the Hd isentrope at various potential temperatures (T_P).

Figure 8. a) A comparison of the mixing model using a Fa end member ($AnHd_{modelFa}$ = 0.5An +0.25 Fa -0.25 Fo +0.5Di) and the An-Hd isentrope at various potential temperatures (T_P) and b) its % errors in temperature and density in estimating the An-Hd isentrope. c) A comparison of the mixing model using a Hd end member ($AnHd_{modelHd}$ = 0.5 An +0.5Hd) and the An-Hd isentrope at various potential temperatures (T_P) d) its % errors in temperature and density in estimating the An-Hd isentrope. Errors shown in text are the maximum at 120 GPa.

Figure 9. a) A comparison of the mixing model using a Fa end member ($AnHdDi_{modelFa}$ = 0.33An +0.667Di +0.167 Fa -0.167 Fo) and the An-Hd-Di isentrope at various potential temperatures (T_P) and b) its % errors in temperature and density in estimating the An-Hd-Di isentrope. c) A comparison of the mixing model using a Hd end member ($AnHdDi_{modelHd}$ = 0.33 An +0.33Hd +0.33Di) and the An-Hd-Di isentrope at various potential temperatures (T_P) d) its % errors in temperature and density in estimating the An-Hd-Di isentrope. Errors shown in text are the maximum at 120 GPa.

Figure 10. a) A comparison of the two mixing models for chondrite liquid ($Ch_{modelFa}$= 0.62En+0.24Fo +0.08Fa +0.04An +0.02Di and $Ch_{modelAnHdDi}$ = 0.62En +0.32Fo +0.45AnHdDi -

0.12An -0.28Di) and b) their % error difference in temperature and density. Errors shown in text are the maximum at 120 GPa.

FIGURES

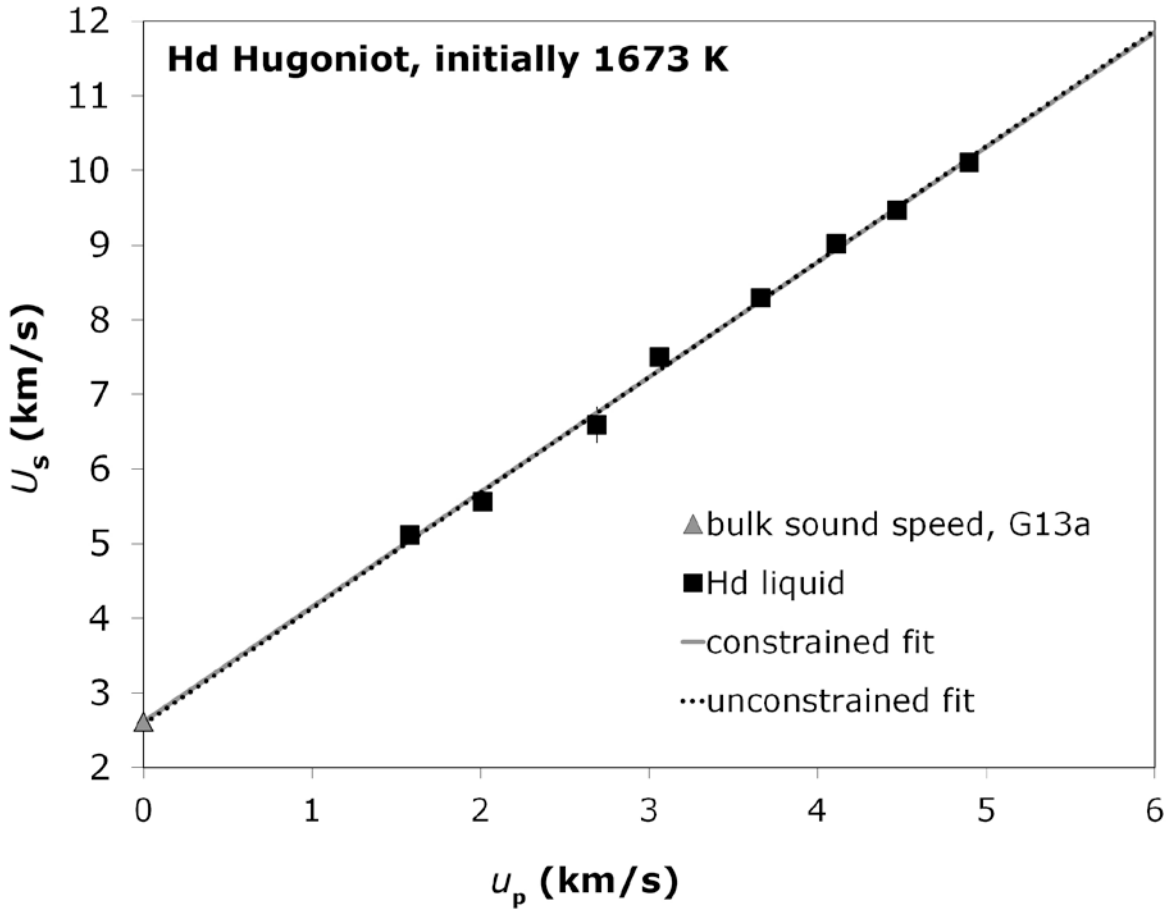

Figure 1

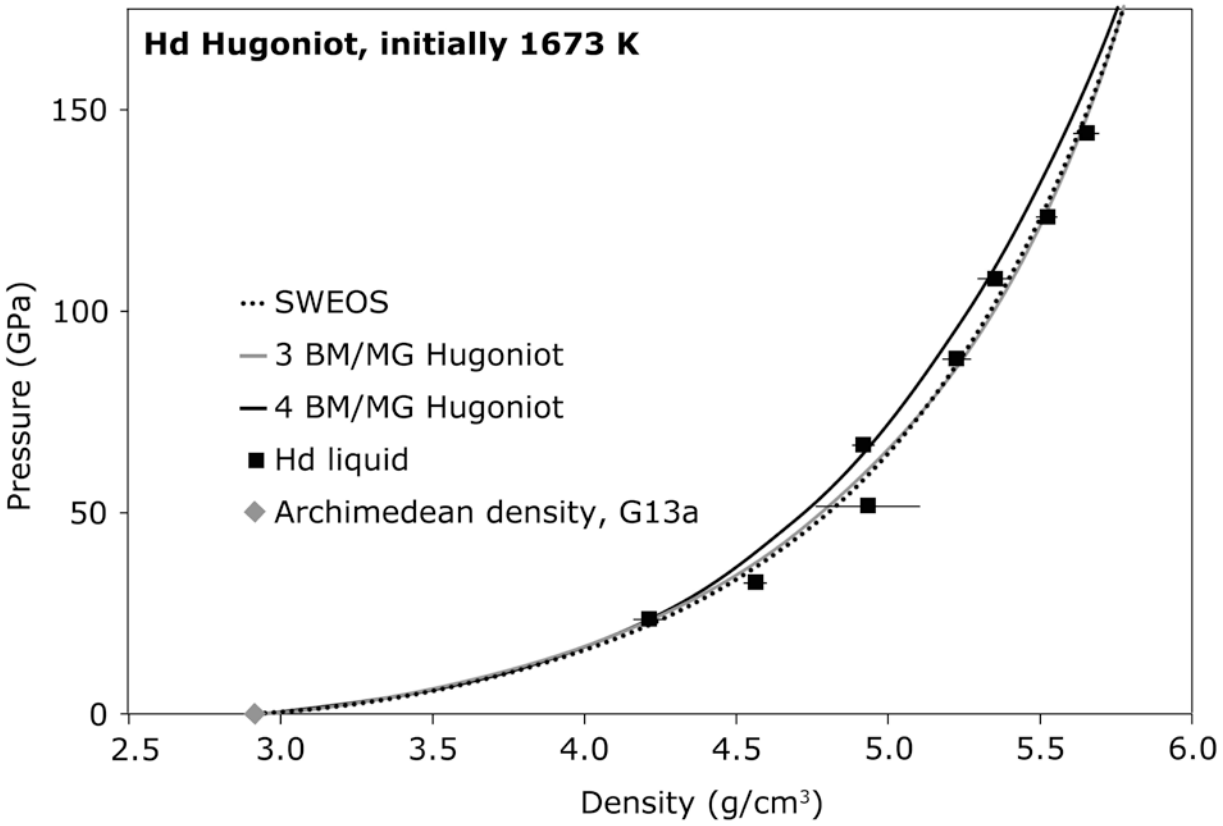
Hd Hugoniot, initially 1673 K
150
100
50
0
Pressure (GPa)
SWEOS
3 BM/MG Hugoniot
4 BM/MG Hugoniot
Hd liquid
Archimedean density, G13a
2.5
3.0
3.5
4.0
4.5
5.0
5.5
6.0
Density (g/cm³)

Figure 2

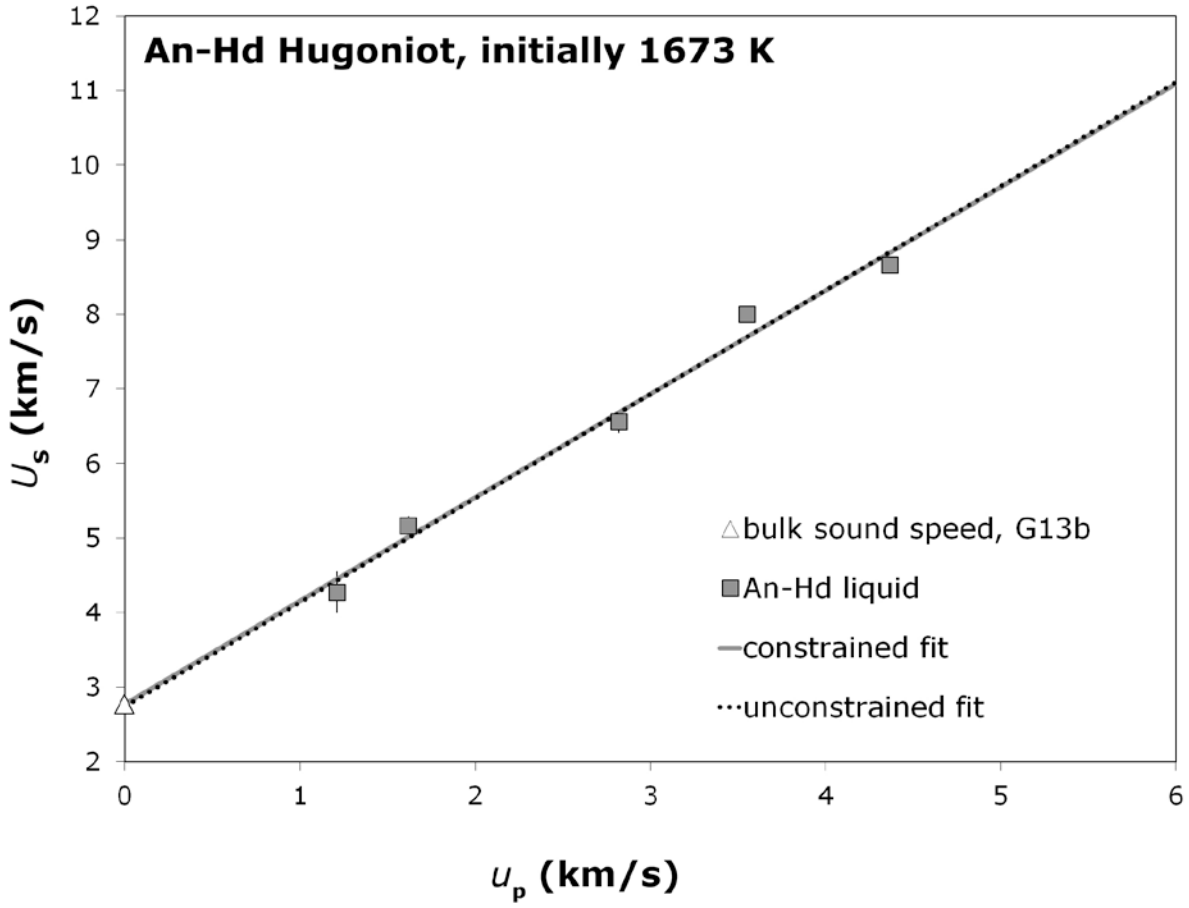
An-Hd Hugoniot, initially 1673 K
U_s (km/s)
u_p (km/s)
bulk sound speed, G13b
An-Hd liquid
constrained fit
unconstrained fit

Figure 3

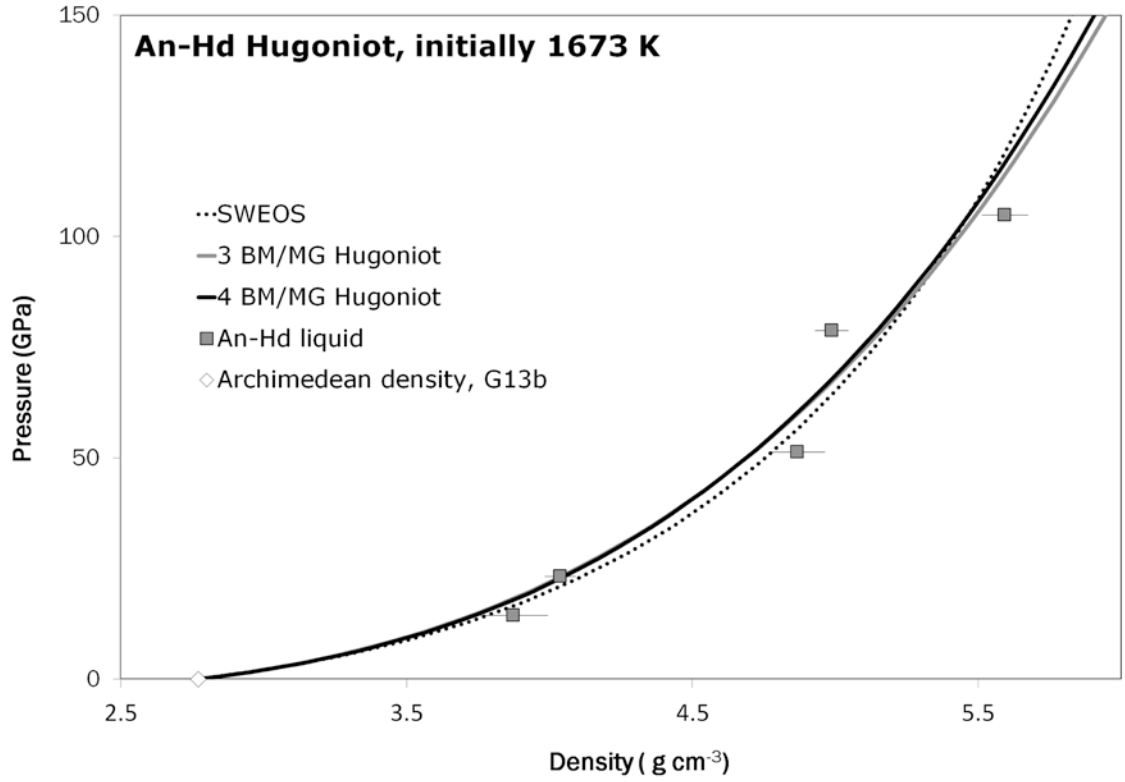
An-Hd Hugoniot, initially 1673 K
SWEOS
3 BM/MG Hugoniot
4 BM/MG Hugoniot
An-Hd liquid
Archimedean density, G13b
Pressure (GPa)
Density (g cm-3)
150
100
50
0
2.5
3.5
4.5
5.5

Figure 4

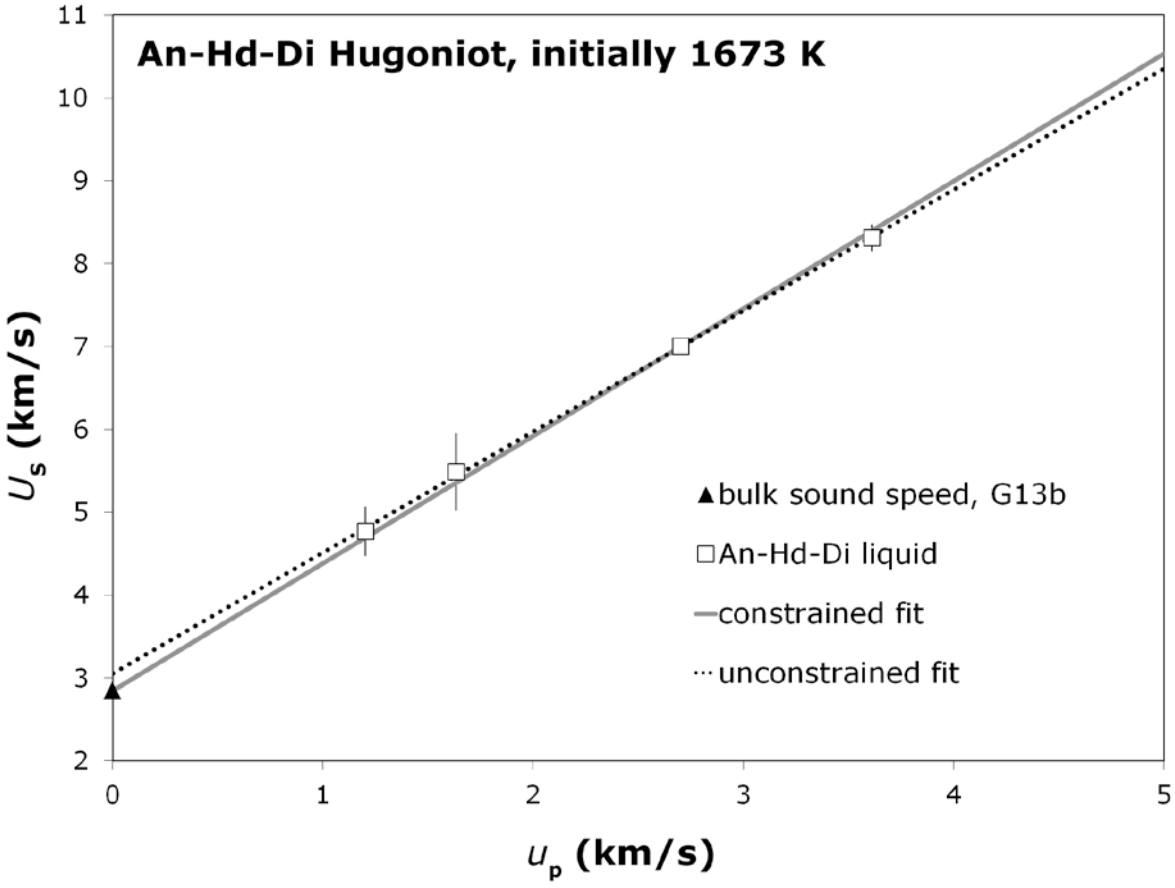
An-Hd-Di Hugoniot, initially 1673 K
U_s (km/s)
u_p (km/s)
bulk sound speed, G13b
An-Hd-Di liquid
constrained fit
unconstrained fit
11
10
9
8
7
6
5
4
3
2
0
1
2
3
4
5

Figure 5

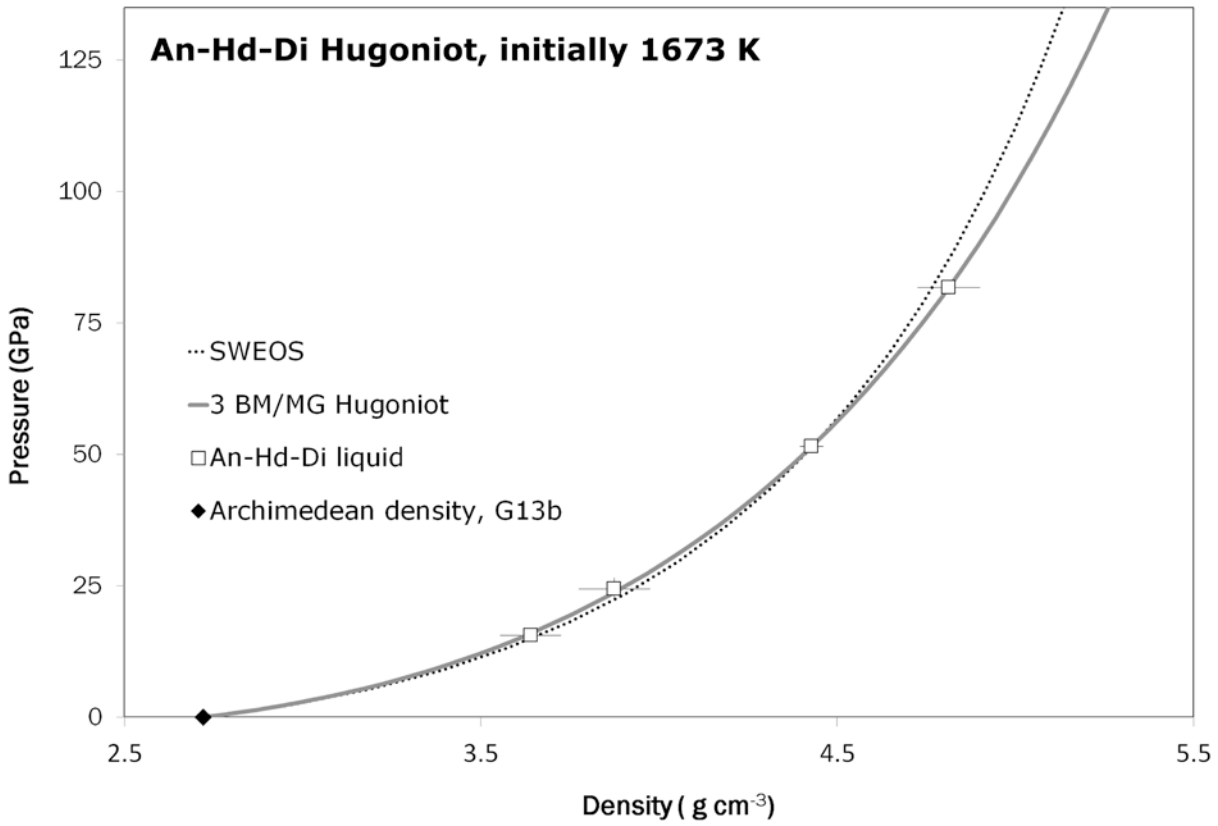
An-Hd-Di Hugoniot, initially 1673 K
Pressure (GPa)
125
100
75
50
25
0
2.5
3.5
4.5
5.5
Density (g cm-3)
SWEOS
3 BM/MG Hugoniot
An-Hd-Di liquid
Archimedean density, G13b

Figure 6

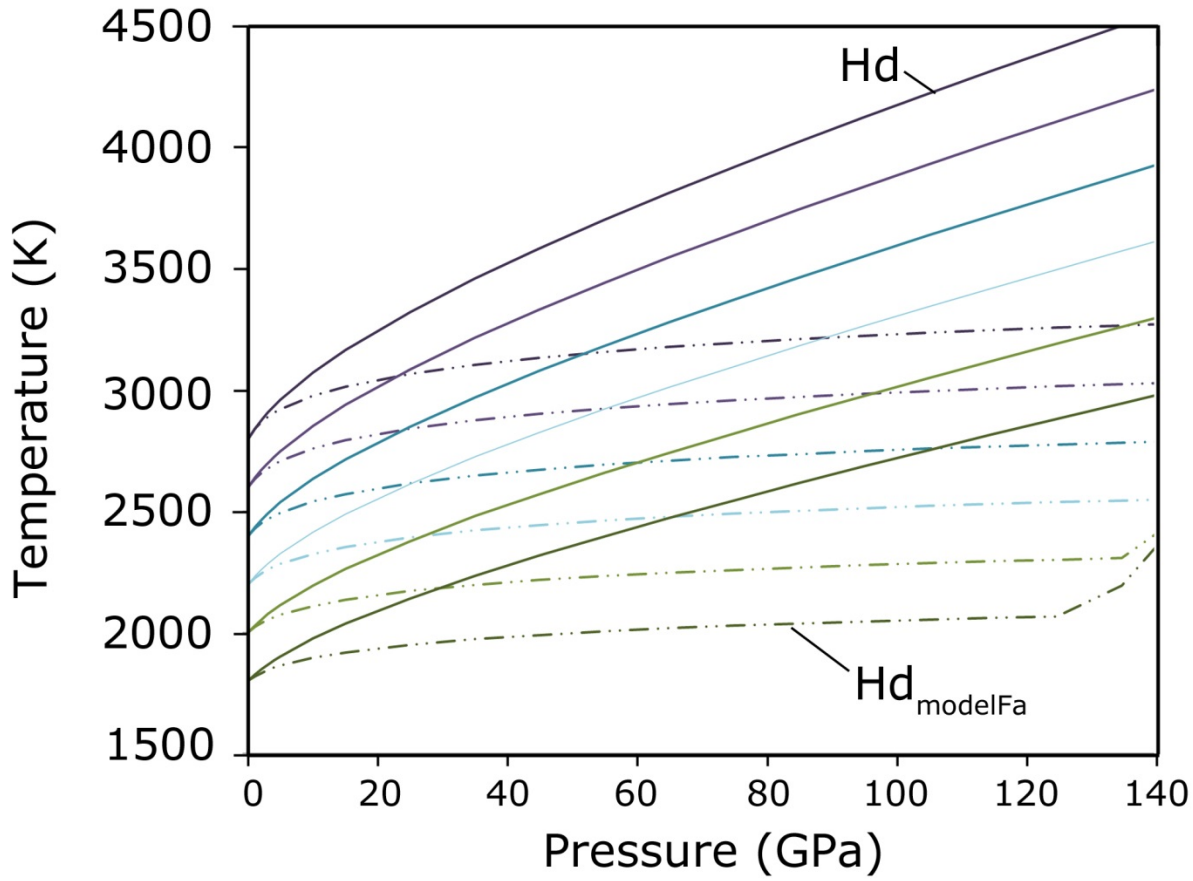
4500
4000
3500
3000
2500
2000
1500
Temperature (K)
0
20
40
60
80
100
120
140
Pressure (GPa)
Hd
Hd modelFa

Figure 7

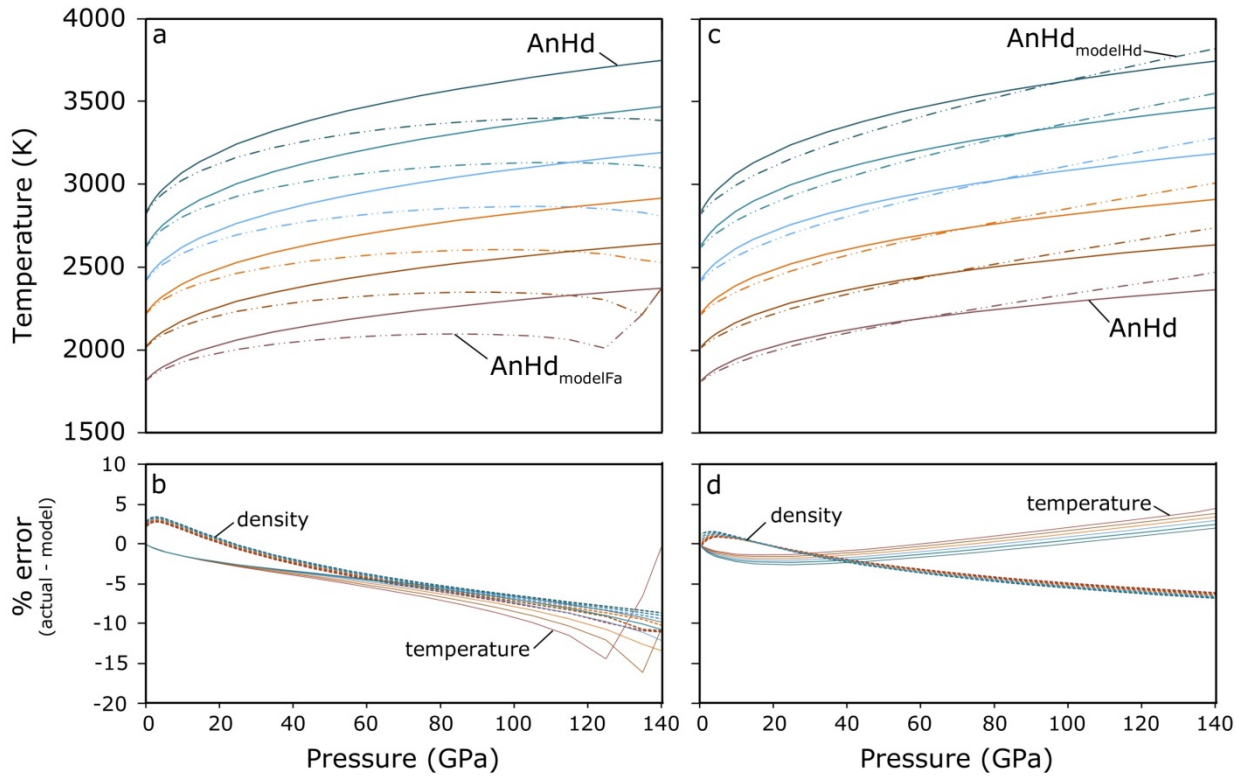
a
AnHd
AnHd modelFa
c
AnHd modelHd
AnHd
Temperature (K)
4000
3500
3000
2500
2000
1500
b
density
temperature
d
density
temperature
% error
(actual - model)
10
5
0
-5
-10
-15
-20
0
20
40
60
80
100
120
140
Pressure (GPa)
Pressure (GPa)

Figure 8

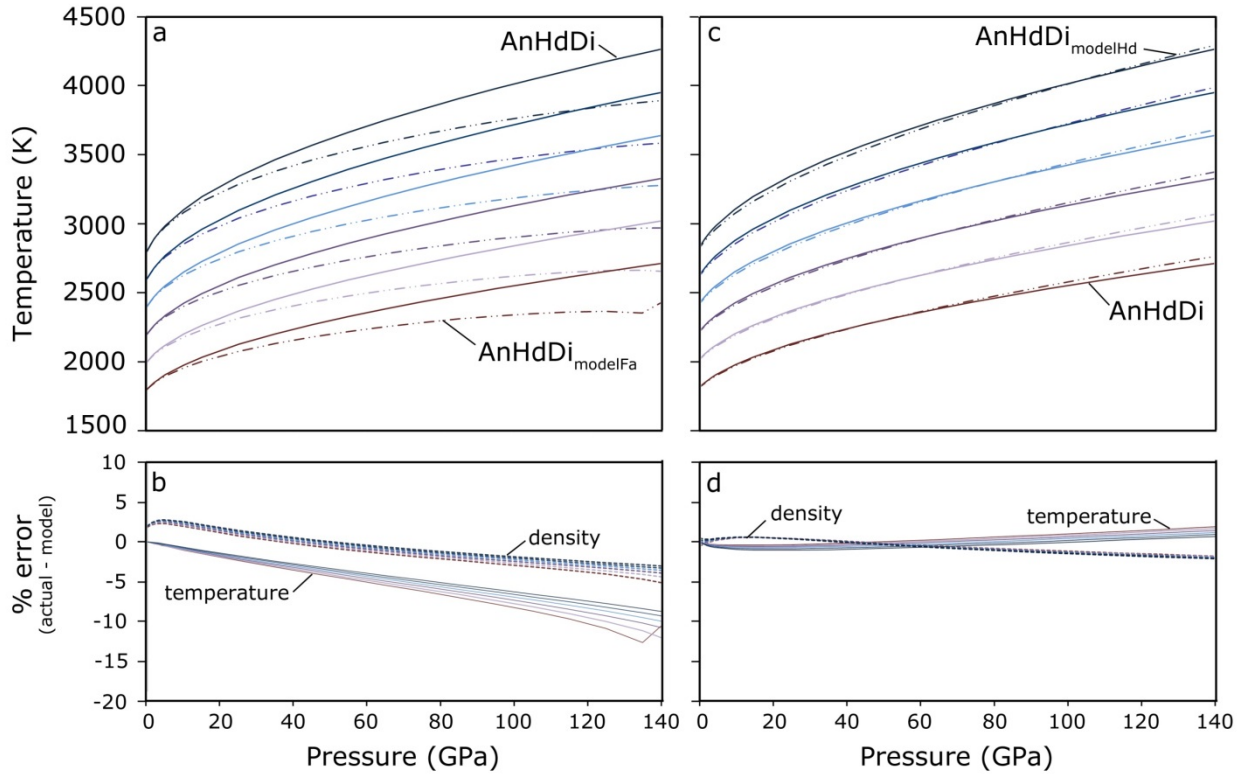
a
AnHdDi
AnHdDi modelFa
c
AnHdDi modelHd
AnHdDi
Temperature (K)
4500
4000
3500
3000
2500
2000
1500
b
density
temperature
% error
(actual - model)
10
5
0
-5
-10
-15
-20
d
density
temperature
0
20
40
60
80
100
120
140
Pressure (GPa)
Pressure (GPa)

Figure 9

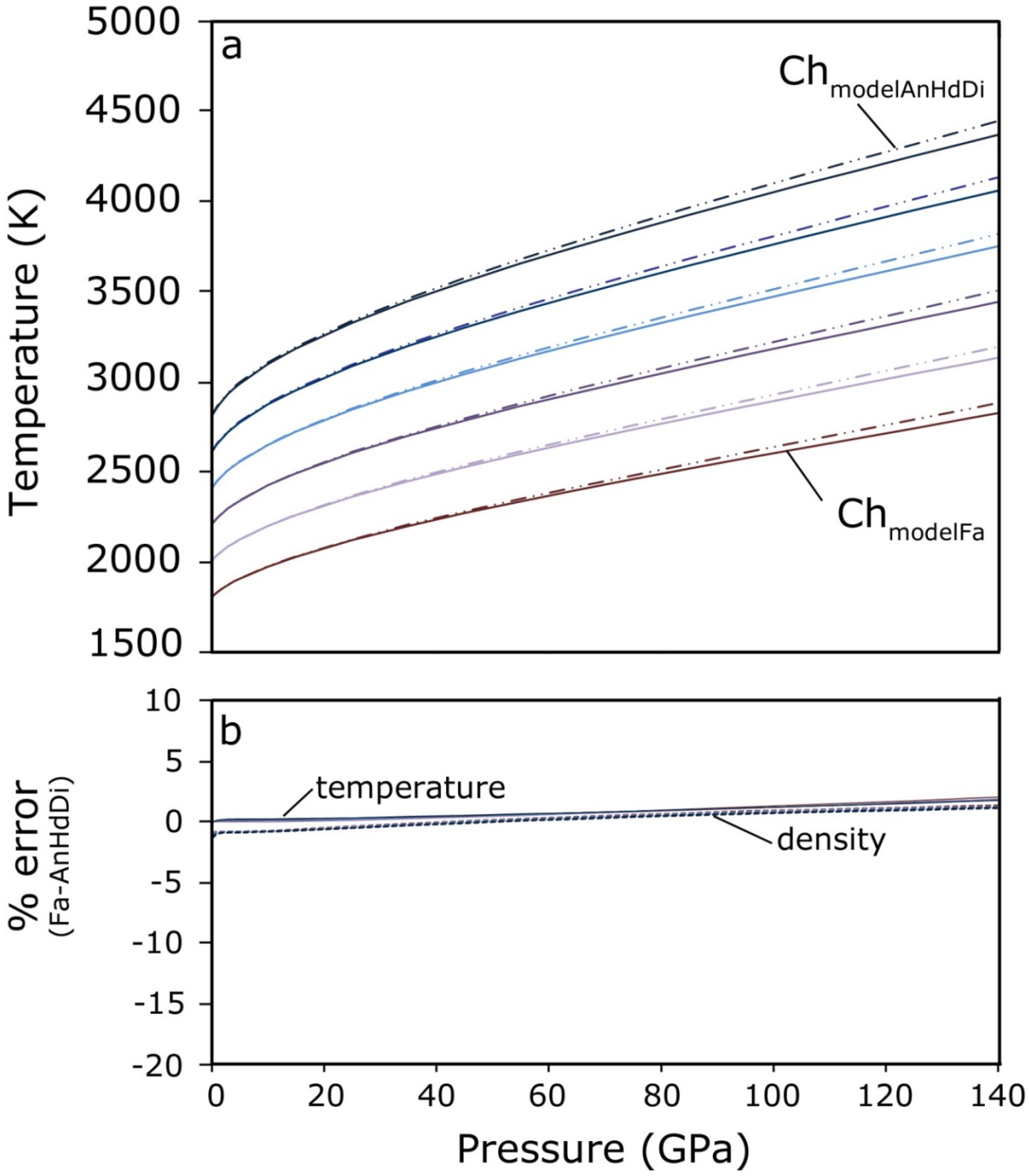
a
b
Temperature (K)
5000
4500
4000
3500
3000
2500
2000
1500
Ch modelAnHdDi
Ch modelFa
% error
(Fa-AnHdDi)
10
5
0
-5
-10
-15
-20
temperature
density
0
20
40
60
80
100
120
140
Pressure (GPa)

Figure 10